

Synthesis and Characterization of CeO₂ Based Nanostructures



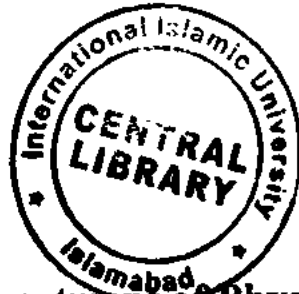
PhD Thesis

By

**Fazal Abbas
(13-FBAS/PHDPHY/F11)**

Supervised by:

Dr. Javed Iqbal Saggi



**Department of Physics
Faculty of Basic and Applied Sciences
International Islamic University, Islamabad
(2017)**

CV

Accession No TH-16734

PhD
620.5
FAS

1. Nanotechnology
2. Nanostructures



INTERNATIONAL ISLAMIC UNIVERSITY, ISLAMABAD

Faculty of Basic and Applied Sciences

DEPARTMENT OF PHYSICS

13 January, 2017

Certificate

This is to certify that the work contained in this thesis entitled: **“Synthesis and Characterization of CeO₂ Based Nanostructures”** has been carried out by **Mr. Fazal Abbas** in Laboratory of Nanoscience and Technology (LNT) under my supervision. In my opinion, this is fully adequate in scope and quality for the thesis of PhD Physics.

Supervisor

Dr. Javed Iqbal Saggu

Synthesis and Characterization of CeO₂ Based Nanostructures

By

Fazal Abbas

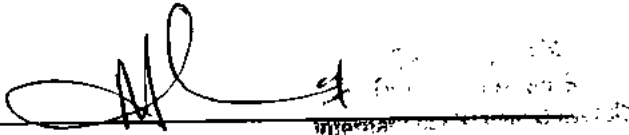
(13-FBAS/PHDPHY/F11)

A thesis submitted to

Department of Physics

For the award of the degree of

PhD Physics

Signature: 
(Chairman, Department of Physics, IIUI)

Signature: 
(Dean, FBAS, IIU, Islamabad)

International Islamic University, Islamabad

Faculty of Basic and Applied Sciences

Department of Physics

Dated: 13 January, 2017

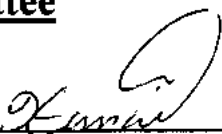
Final Approval

This is to certify that work in this dissertation entitled “**Synthesis and Characterization of CeO₂ Based Nanostructures**” has been carried out by **Mr. Fazal Abbas**, Registration No. **13-FBAS/PHDPHY/F11** and completed in Laboratory of Nanoscience and Nanotechnology, Department of Physics, Faculty of Basic and Applied Sciences, International Islamic University, Islamabad is of sufficient standard in scope and quality for the award of degree of **PhD Physics**.

Committee

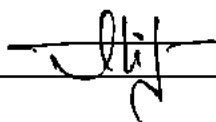
External Examiner 1

Dr. Iftikhar Gul
SCME, National University of
Science and Technology (NUST), Islamabad.



External Examiner 2

Dr. Muhammad Atif
Department of Physics,
AIR University, Islamabad.



Internal Examiner

Dr. Naeem Ahmed
Department of Physics,
FBAS, IIUI.



Supervisor

Dr. Javed Iqbal Saggu
Department of Physics,
QAU, Islamabad.



*This work is submitted as a dissertation in partial fulfillment of the requirement
for the degree of*

PhD in PHYSICS

at

Department of Physics

International Islamic University, Islamabad.

Declaration

I hereby declare that this thesis work, neither as a whole nor a part of it has been copied out from any source except referred to wherever due. Furthermore, work presented in this dissertation has not been submitted in support of any application for any other degree or qualification to any other university or institute. This thesis is based on my listed publications. If any part of this project is proved to be copied from any source or found to be reproduction of some other project, I (Fazal Abbas) shall be legally responsible for punishment under the plagiarism rules of Higher Education Commission (HEC), Pakistan.



Fazal Abbas

(13-FBAS/PHDPHY/F11)

DEDICATED TO

My Parents, Sweet Bushra

&

Ahadi

AKNOWLEDGEMENT

First of all, I want to thank Allah who blessed me a mind to contemplate, a talent for analysis, a knack for science, strength and determination to write this dissertation which is a major mile stone in my academic career.

I am immensely thankful to my parents who instilled in me an aptitude for learning and dedication for work. Special thanks to my mother for her generous encouragement, underlying support and heartfelt prayers which have been working as elixir in my life.

I would like to extend my acknowledgements to my research supervisor Dr. Javed Iqbal Saggu for his continuous support, outstanding scientific guidance, tremendous cooperation and motivation. He is the real source behind the compilation of this research work. It was impossible for me to complete this work without the munificent guidelines and constant support of Dr. Javed. I am fortunate enough that I got an opportunity to work with him and I would like to convey my heartfelt gratitude to him for his keen interest and involvement in the work. I would also like to thank Chairman Department of Physics and Dean Faculty of Basic and Applied Sciences, IIUI for their cooperation during my research work. Their sincere pieces of advice and proactive guidance facilitated me to do my work with comfort and due concentration.

I am thankful to Dr. Sajjad Haider Naqvi (Department of Biochemistry, University of Karachi), Dr. Arshad Janjua (NILOPE Islamabad), Mr Qaiser Mansoor and Dr. M. Ismail (Institute of Biomedical and Genetic Engineering Islamabad) for providing me the much-needed opportunity to do part of experimental work in their laboratories.

I'd hardly be able to express deep sense of gratitude that I feel for Mr. Tariq Jan for supporting me whenever I required his assistance. He helped me out where I was stuck and remained, throughout this extended period of research, a never-ending source of motivation and inspiration.

I'm also indebted to Mr. Shahid Amir and Mr. Shams Ali (SCME, NUST) for providing me a valuable opportunity of SEM. I also want to pay special thanks to Dr. Shahid Atiq (CSSP, PU Lahore) for their valuable cooperation. I am also very thankful to my research fellows M. Waqee-ue-Rehman, Irfan Qasim, Kashif Shehzad, Aqsa Arshad and Faisal Shahzad for their support and kindness.

I also owe my deepest gratitude to my family including my parents, sisters and brothers, especially my wife, Bushra whose untiring support surpasses any gratitude that I may express.

Last but not the least; I am also very thankful to Prof. Dr. Yuo Ronghui, Beihang University Beijing, China for his outstanding scientific guidance, tremendous cooperation and motivation when I was in need during my research work.

Fazal Abbas

List of Publications

This thesis is based on the following publications:

1. **F. Abbas, J. Iqbal, T. Jan, M. S. H. Naqvi, A. Gul, R. Abbasi, A. Mahmood, I. Ahmad, M. Ismail, Differential cytotoxicity of ferromagnetic Co doped CeO₂ nanoparticles against human neuroblastoma cancer cells, Journal of Alloys and Compounds, 648 (2015) 1060-66. (I.F= 3.00)**
2. **F. Abbas, T. Jan, J. Iqbal, M.S.H. Naqvi, Fe doping induced enhancement in room temperature ferromagnetism and selective cytotoxicity of CeO₂ nanoparticles, Current Applied Physics, Current Applied Physics, 15 (2015) 1428-1434.(I.F= 2.21)**
3. **F. Abbas, T. Jan, J. Iqbal, I. Ahmed, M.S.H. Naqvi, M. Malik, Facile synthesis of ferromagnetic Ni doped CeO₂ nanoparticles with enhanced anticancer activity, Applied Surface Science, 357 (2015) 931-936. (I.F= 2.71)**
4. **F. Abbas, T. Jan, J. Iqbal, I. Ahmed, M.S.H. Naqvi, Inhibition of Neuroblastoma cancer cells viability by ferromagnetic Mn doped CeO₂ monodisperse nanoparticles mediated through reactive oxygen species, Materials Chemistry and Physics, 173 (2016) 146-151. (I.F= 2.259)**
5. **F. Abbas, J. Iqbal, T. Jan, N. Badshah, Q. Mansoor, M. Ismail, Structural, morphological, Raman, optical, magnetic, and antibacterial characteristics of CeO₂ nanostructures, Int. J. Miner. Metall. Mater., 23 (2016) 102-108. (I.F= 0.80)**

Additional publications:

6. **J. Iqbal, T. Jan , M.S. Awan, M.S.H. Naqvi, S. F.H. Naqvi, A. Ullah, F. Abbas, Mg Doping Induced Effects on Structural, Optical and Electrical Properties as well as Cytotoxicity of CeO₂ Nanostructures, accepted manuscript in Metallurgical and Materials Transactions B, 47 (2016) 1363-1368. (I.F= 1.45).**

7. T. Jan, S. Hassan, I. Ahmed, Q. Mansoor, M. U. Ali, **F. Abbas**, M. Ismail, Facile synthesis of Zn doped CuO hierarchical nanostructures: Structural, optical and antibacterial properties, *AIP ADVANCES*, **5** (2015) 127112. **(I.F= 1.52)**
8. T. Jan, J. Iqbal, Q. Mansoor, M Ismail, M.S.H. Naqvi, A. Gul, S.F.H. Naqvi and **F. Abbas**, Synthesis, physical properties and antibacterial activity of Ce doped CuO: a novel nanomaterial, *J. Phys. D: Appl. Phys.*, **47** (2014) 355301. **(I.F= 2.72)**
9. S. Atiq, S.A. Siddiqi, **F. Abbas**, M. Saleem, S.M. Ramay, Carriers-assisted Enhanced Ferromagnetism in Al-doped ZnMnO Nano-crystallites, *Chin. J. Chem. Phys.*, **26** (2013) 457-461. **(I.F= 0.50)**

Abstract

Rare-earth metal oxide (REMO) nanomaterials play a major role in emerging technologies related to magnetic and biomedical applications. The partially unfilled 4f shells of REMOs make them potential for future spintronics nano devices and targeted cancer therapy. This property of REMO may lead to room temperature ferromagnetism (RTFM) with high T_c and also to control the ROS production as well as redox reaction. The introduction of different impurities especially TM into REMO host matrix due to exchange interaction of 4f with 3d can significantly further improve the efficiency of REMO based devices. The physical characteristics and bioactivity of REMO nanoparticles are significantly dependent on the particle size, type and level of dopants and defects. This thesis is schematically based on the fabrication and characterizations of CeO_2 nanoparticles, as well as selective doping in the host matrix in order to tune its structural, optical, magnetic and electrical properties as well as anticancer characteristics. The scope of this study lies in the interesting fields of biophysics and spintronics.

In the start, co-precipitation method has been optimized to fabricate the desired CeO_2 nanoparticles having homogeneous size, shape and distributions via controlling through various synthesis parameters.

In Chapter No. 1, transition metal (TM) Co ions doped CeO_2 nanoparticles have been prepared by optimized facile chemical co-precipitation technique. The structural investigations reveal the formation of single phase cubic fluorite structure of CeO_2 for undoped and doped samples. Morphological examinations demonstrate the formation of highly homogeneous nanoparticles with average particle size in the range of 8-20 nm. The specific surface area (SSA) is observed to be $234 \text{ m}^2/\text{g}$ for undoped CeO_2 and is found to be enhanced remarkably as function of Co doping level. Raman spectroscopy results depict the presence of V_o defects in undoped CeO_2 nanoparticles which are found to be further enhanced in host matrix as function

of cationic doping. The optical and dielectric properties of CeO₂ nanoparticles are significantly tailored via dopant impurity induced defects (such as abundance of V_o) as observed in Raman spectroscopy. The narrowing of band gap up to 0.34 eV and enhancement in dielectric constant up to 10 via Co doping have been observed which may be linked to introduction of impurity levels mediated by structural defects like V_o and structural parameters variations etc. It is found that these defects (V_o) play a vital role in the activation of RTFM in both undoped and Co doped CeO₂ nanoparticles which may arise from exchange interactions. It is interestingly observed that these synthesized nanoparticles have very significant differential cytotoxicity inhibiting the growth of human Neuroblastoma cancerous cells up to 69% without harming healthy cells.

In the Chapter No. 2, TM (Fe) ions have been doped in the CeO₂ nanoparticles host matrix by the same method as used for Co doped samples. SEM and XRD results have shown that the synthesized samples are comprised of ultrafine spherical nanoparticles having single phase cubic fluorite structure of CeO₂. Raman spectroscopy results have depicted a red shift in F_{2g} mode with Fe doping which reveals enhancement in the V_o. The optical band gap calculated from UV-visible absorption spectra has been found to tune up to 0.2 eV with Fe doping which is associated with the creation of impurity level and abundance in V_o with Fe doping. The V_o have introduced the RTFM in undoped and Fe doped CeO₂ nanoparticles. The M_s value of pristine CeO₂ nanoparticles has been found to be 0.0083 emu/g which is increased up to 0.0126 emu/g for 7% Fe doped nanoparticles which may be due to overlapping of bound polarons created by V_o due to TM ions doping. For cytotoxicity tests, the synthesized nanoparticles induced effects on Neuroblastoma cancer cells & HEK-293 healthy cells have been analyzed via CCK-8 analysis. It has been observed that the prepared undoped and Fe doped CeO₂ nanoparticles have nontoxic nature towards healthy cells while they are extremely toxic towards cancerous cells. Furthermore, the anticancer activity is found to enhance with Fe

doping. The selective toxicity and enhancement in anticancer activity with Fe doping has observed to be strongly correlated with ROS generation.

In Chapter No. 3, TM (Ni) ions have been doped in the CeO₂ nanoparticles host matrix by the same method as used in previous experiments. XRD and Raman results have indicated the formation of single phase cubic fluorite structure for the synthesized nanoparticles. Ni dopant has induced excessive structural changes such as decrease in crystallite size as well as lattice constants and enhancement in V_o in CeO₂ crystal structure. These structural variations have significantly influenced the optical and magnetic properties of CeO₂ nanoparticles. The synthesized Ni_xCe_{1-x}O₂ nanoparticles have exhibited RTFM behavior having M_s 0.0357 emu/g. Ni doping induced effects on the cytotoxicity of CeO₂ nanoparticles have been examined against HEK-293 healthy cell line and SH-SY5Y neuroblastoma cancer cell line. The prepared Ni_xCe_{1-x}O₂ nanoparticles demonstrated differential cyto-toxicity up to 50%. Furthermore, anticancer activity of CeO₂ nanoparticles has been observed to be significantly enhanced with Ni doping. The level of ROS is observed to be responsible for this cytotoxic nature of the synthesized nanoparticles.

In the last chapter, the Mn doping induced effects on structural, Raman, optical, magnetic and anticancer properties of CeO₂ nanoparticles have been investigated. Structural and microstructural results infer that the synthesized nanoparticles have single phase cubic fluorite structure of CeO₂ and that Mn doping results in enhancement of the structural defects. SEM results reveal the formation of monodisperse nanoparticles having average particle size ranging from 30 to 41 nm. The optical absorbance spectroscopy analysis depicts the band gap energy tailoring of CeO₂ nanoparticles via Mn doping with a red shift of 0.36 eV. RTFM has been found in both as-prepared and Mn doped CeO₂ nanoparticles. This RTFM of the synthesized nanoparticles have been attributed to the Mn ions and surface defects such as V_o. Finally, the influence of Mn dopant on the cell viability and ROS generation levels of CeO₂

nanoparticles in the presence of healthy and cancerous cells have been studied. It has been observed that the differential cytotoxic nature of the synthesized $Mn_xCe_{1-x}O_2$ nanoparticles is strongly linked with the level of ROS generation.

The detail study of uniformly distributed $TM_xCe_{1-x}O_2$ nanoparticles with tailored structural, microstructural, bandgap, dielectric, RTFM and differential cytotoxic nature will open new insight in optomagnetic nano devices and targeted cancer therapeutic fields.

Table of Contents

Chapter No.1	1
Introduction	1
1.1 Introduction.....	1
1.2 CeO ₂	3
1.2.1 Fundamental properties of CeO ₂	4
1.2.2 Crystal structure of CeO ₂	5
1.2.3 Defects chemistry of CeO ₂	7
1.2.4 Specific surface area (SSA)	9
1.2.5 Optical properties of CeO ₂	10
1.2.6 Redox chemistry of CeO ₂	12
1.2.7 Vibrational properties of CeO ₂	12
1.2.8 Magnetic doping of CeO ₂	13
1.2.9 Biological activity of CeO ₂	18
1.3 Statement of Problem.....	21
1.4 Aims and Objectives of the Thesis	22
Chapter No.2	24
Synthesis and Characterization Techniques	24
2.1 Nanotechnology and Nanomaterials	24
2.1.1 Size effects	24
2.1.2 Classification of nanomaterials	25
2.2 Synthesis Techniques.....	26
2.2.1 Bottom-up approach.....	26
2.2.2 Top-down approach	27
2.2.3 Chemical co-precipitation method	28
2.3 Synthesis Parameters Optimization	30
2.3.1 Reaction temperature	30
2.3.2 Role of pH.....	31
2.3.3 Role of surfactant	32
2.4 Synthesis Procedures	34
2.4.1 Synthesis of CeO ₂ nanostructures	34
2.4.1.1 Synthesis of Co doped CeO ₂ nanostructures.....	34

2.4.1.2 Synthesis of Fe doped CeO ₂ nanostructures	34
2.4.1.3 Synthesis of Ni doped CeO ₂ nanostructures	34
2.4.1.4 Synthesis of Mn doped CeO ₂ nanostructures	34
2.5 Cell Culture, Anticancer Activity and Cytotoxicity of CeO ₂ Nanostructures	35
2.6 Characterization Techniques.....	36
2.6.1 X-ray diffraction (XRD)	36
2.6.2 Scanning electron microscopy (SEM)	38
2.6.3 Raman spectroscopy	39
2.6.4 Ultra violet visible (UV-Vis) spectrometry.....	40
2.6.5 Vibrating sample magnetometer (VSM).....	41
2.6.6 Brunauer-Emmet and Teller (BET) SSA analyzer.....	42
2.6.7 Electrical measurements using LCR meter	44
Chapter No.3.....	46
Synthesis, Characterization and Anticancer Study of Co Doped CeO₂ Nanoparticles.....	46
3.1 Introduction.....	46
3.2 Results and Discussions	47
3.2.1 Structural and morphological investigations.....	47
3.2.2 Analysis of surface area	50
3.2.3 Raman and optical characterizations.....	51
3.2.4 Dielectric properties.....	53
3.2.5 Magnetic study	55
3.2.6 Differential cytotoxicity analysis	57
Chapter No.4.....	60
Synthesis, Characterization and Anticancer Study of Fe Doped CeO₂ Nanoparticles.....	60
4.1 Introduction.....	60
4.2 Results and Discussions	61
4.2.1 Structural and morphological investigations.....	61
4.2.2 Analysis of surface area	63
4.2.3 Raman and optical characterizations.....	64
4.2.4 Dielectric properties.....	66
4.2.5. Magnetic study.....	68
4.2.6 Differential cytotoxicity analysis	69

Chapter No.5.....	73
Synthesis, Characterization and Anticancer Study of Ni Doped CeO₂ Nanoparticles.....	73
5.1 Introduction.....	73
5.2 Results and Discussions	73
5.2.1 Structural and morphological investigations.....	73
5.2.2 Analysis of surface area	76
5.2.3 Raman and optical characterizations.....	76
5.2.4 Dielectric properties.....	79
5.2.5. Magnetic study.....	81
5.2.6 Differential cytotoxicity analysis.....	82
Chapter No.6.....	85
Synthesis, Characterization and Anticancer Study of Mn Doped CeO₂ Nanoparticles.....	85
6.1 Introduction.....	85
6.2 Results and Discussions	86
6.2.1 Structural and morphological investigations.....	86
6.2.2 Analysis of surface area	88
6.2.3 Raman and optical characterizations.....	88
6.2.4 Dielectric properties.....	91
6.2.5 Magnetic study.....	93
6.2.6 Differential cytotoxicity analysis	94
Conclusion.....	99
References	102

LIST OF FIGURES

Figure 1.1: Position of rare earth elements in periodic table	1
Figure 1.2: The face centered cubic cell of fluorite ceria	5
Figure 1.3: The crystal structure of CeO ₂ ; (a) two unit cells (b) alternate view	6
Figure 1.4: Generalized size-dependent reactivity of a material.....	10
Figure 1.5: A schematic of the discrete energy level of a semiconductor	11
Figure 1.6: Illustrating (A) a magnetic semiconductor, (B) a non-magnetic semiconductor material, and (C) a diluted magnetic semiconductor.....	14
Figure 1.7: Polaron percolation model as illustrated by Coey et al.	18
Figure 1.8: Magnetic nanoparticles-based cancer therapy.....	20
Figure 1.9: Possible mechanisms by which nanomaterials interact with biological tissues.. ..	21
Figure 2.1: The plot of percentage of surface atoms as a function of particle size.....	25
Figure 2.2 A Schematic representation of the “top-down” and “bottom-up” approaches	27
Figure 2.3: A Schematic diagram for the preparation of CeO ₂ nanostructures by the chemical co- precipitation method	29
Figure 2.4: (a) XRD patterns CeO ₂ prepared at distinct reaction temperatures (b) SEM micrograph of CeO ₂ prepared via temperature treated synthesis	30
Figure 2.5: XRD patterns CeO ₂ prepared at distinct reaction temperatures	31
Figure 2.6: SEM micrographs of synthesized CeO ₂ prepared using various surfactants.....	33
Figure 2.7: Diffraction of X-rays from a crystal.....	38
Figure 2.8: An illustration of the three types of scattering related to Raman spectroscopy	40
Figure 2.9: Principle of UV-VIS Spectroscopy	41
Figure 2.10: (a) A general setup of VSM (b) a hysteresis loop	42
Figure 2.11: Schematic diagram of LCR meter	45
Figure 3.1: a) XRD patterns of the prepared samples and b) Co loading induced shift in the (111) plane.....	48

Figure 3.2: SEM images of $Ce_{1-x}Co_xO_2$ nanoparticles. (a) undoped CeO_2 , (b) 3% Co doped CeO_2 , (c) 5% Co doped CeO_2 , (d) 7% Co doped CeO_2	49
Figure 3.3: BET-SSA Analysis of $Ce_{1-x}Co_xO_2$ nanoparticles	50
Figure 3.4: Raman spectra of the prepared nanoparticles	51
Figure 3.5: (a): UV-Vis absorption spectra of the CeO_2 nanoparticles (b): Plots of $(\alpha h\nu)^2$ as a function of photon energy E for the synthesized nanoparticles	53
Figure 3.6: (a): Dielectric Constant (ϵ'), (b): Dielectric Loss (ϵ''), (c): AC conductivity (δ_{AC}), variations as a function of AC frequency.....	54
Figure 3.7: M-H loops of undoped and Co-doped CeO_2 nanoparticles (Inset of the figure shows opened loops).....	56
Figure 3.8: Effect of undoped & Co doped CeO_2 nanoparticles on Neuroblastoma & HEK-293 cells viability	57
Figure 3.9: Reactive oxygen species (ROS) production in Neuroblastoma & HEK-293 Cells after incubation with undoped and Co doped CeO_2 nanoparticles.....	58
Figure 4.1: a) XRD patterns of the prepared samples, b) shift in the (111) plane with Fe doping	61
Figure 4.2: SEM images of (a) undoped (b) 1% (c) 3% (d) 5% and (e) 7% Fe doped CeO_2 nanoparticles	62
Figure 4.3: BET-SSA Analysis of $Ce_{1-x}Fe_xO_2$ nanoparticles	63
Figure 4.4: Raman spectra of the prepared nanoparticles.....	64
Figure 4.5: (a): UV-Vis absorption spectra of the $Fe_xCe_{1-x}O_2$ nanoparticles (b): Plots of $(\alpha h\nu)^2$ as a function of photon energy E for the synthesized nanoparticles.....	66
Figure 4.6: (a): Dielectric Constant (ϵ'), (b): Dielectric Loss (ϵ''), (c): AC conductivity (δ_{AC}), variations as a function of AC frequency.....	68
Figure 4.7: M-H loops of undoped and Fe doped CeO_2 nanoparticles (Inset of the figure shows opened loops).....	69
Figure 4.8: Effect of undoped & Fe doped CeO_2 nanoparticles on Neuroblastoma & HEK-293 Cells viability	70

Figure 4.9: Reactive oxygen species (ROS) production in Neuroblastoma & HEK-293 Cells after incubation of undoped and Fe doped CeO ₂ nanoparticles	72
Figure 5.1: a) XRD patterns of the prepared samples and b) Ni loading induced shift in the (111) plane.....	74
Figure 5.2: SEM images of prepared CeO ₂ nanoparticles with (a) 1% (b) 3% (c) 5% and (d) 7% of Ni doping	75
Figure 5.3: BET-SSA as a function of doping percentage of Ni host CeO ₂ nanoparticles.....	76
Figure 5.4: Raman spectra of the synthesized nanoparticles	77
Figure 5.5: UV-visible absorption spectra of the undoped and Ni doped CeO ₂ nanoparticles.....	78
Figure 5.6: (a): Dielectric Constant (ϵ'), (b): Dielectric Loss (ϵ''), (c): AC conductivity (δ_{AC}), variations as a function of AC frequency.....	80
Figure 5.7: Magnetic study of synthesised samples (Inset well opened MH-loops).....	82
Figure 5.8: Effect of undoped & Ni doped CeO ₂ nanoparticles on Neuroblastoma & HEK-293 Cells viability	84
Figure 5.9: Reactive oxygen species (ROS) production in Neuroblastoma & HEK-293 Cells after incubation of undoped and Ni doped CeO ₂ nanoparticles	84
Figure 6.1: a) XRD patterns of the prepared samples and b) Shift in the (111) plane with Mn doping	86
Figure 6.2: SEM images of (a) 1% (b) 3% (c) 5% and (d) 7% Mn doped CeO ₂ nanoparticles.....	87
Figure 6.3: BET-SSA analysis of synthesized nanoparticles.....	88
Figure 6.4: Raman spectra of the prepared nanoparticles	89
Figure 6.5: UV-visible absorption spectra of the undoped and Mn doped CeO ₂ nanoparticles (Inset shows the bandgap estimation via Tauc relation).....	90
Figure 6.6: (a): Dielectric Constant (ϵ'), (b): Dielectric Loss (ϵ''), (c): AC conductivity (δ_{AC}), variations as a function of AC frequency.....	92
Figure 6.7: M-H loops of undoped and Mn doped CeO ₂ nanoparticles (Inset of the figure shows opened hysteresis loops)	94
Figure 6.8: Effect of undoped & Mn doped CeO ₂ nanoparticles on Neuroblastoma & HEK-293 Cells viability	96

Figure 6.9: ROS production in Neuroblastoma & HEK-293 Cells after incubation of undoped and Mn doped CeO₂ nanoparticles 97

.....
.....
.....

List of Tables

Table 1.1: Basic physical properties of CeO ₂ at room temperature	04
Table 1.2: Some reports on high T _c oxide-based DMSs	17
Table 6.1: Summry of physical Properties of thesis work	98

Chapter No.1

Introduction

1.1 Introduction

Rare earth metal oxides (REMO) belong to an important class of materials being widely explored for various applications. These are formed when rare earth metals elements form oxidic compounds by interacting with oxygen element. There are 15 rare earth metals in the periodic table having atomic numbers ranging from 57 to 71. The rare earth elements were first discovered in 1789 in village of Sweden by Lieutenant Carl Axel Arrhenius.

The image shows a periodic table where the rare earth elements are highlighted in black. The title "Rare Earth Elements" is centered at the top, with "by msesupplies.com" below it. The highlighted elements include the lanthanide series (atomic numbers 57-71) and the actinide series (atomic numbers 89-103). The rest of the periodic table is shown in white with black grid lines.

Figure 1.1: Position of rare earth elements in periodic table [1]

The rare earth elements are also known as lanthanides. This series starts from lanthanum ((La) and ends at lutetium (Lu). The scandium (Sc) and yttrium (Y) are also sometimes grouped to rare earth elements due their similar nature. The rare earth elements are further divided into two groups i.e. light rare earth elements and heavy ones. The light rare earth elements range from La to europium (Eu) while heavy rare earth elements starts

from gadolinium (Gd) and ends at Lu. The elements ranging from cerium (Ce) to Lu have also electron filling in 4f sub shell, therefore they are also known as 4f elements.

The oxides of rare earth elements have tremendous physio-chemical properties such high magneto resistance, excellent luminescence, giant dielectric constant, very higher thermal stabilities and remarkable catalytic activities [1-7]. Due these excellent properties, REMO are widely used in superconductors, fuel cells, lithium ion batteries, water splitting, photocatalysis, defense industry and medical technology [8-13]. The oxides of La and Ce (La_2O_3 and CeO_2) are also widely explored for environmental applications [13, 14].

Among all the REMO CeO_2 is the most abundant material and is present about 66 ppm as metallic Ce and its oxides in the earth crust. The Ce (iv) and Ce (iii) are two possible oxidation states of Ce. The most interesting characteristic of CeO_2 is that the two oxidation states can interchange under certain conditions [15]. CeO_2 is an excellent material having tremendous physio-chemical characteristics such as ultraviolet (UV) light absorption, antioxidant characteristics, ability to form oxygen vacancies on the surface, strong luminescence, unique magnetic behavior, higher thermal, mechanical and chemical stabilities, biocompatibility, and interesting redox reaction on its surface. These excellent and interesting properties of CeO_2 has attracted it for various applications such as in catalysts, oxygen sensors, solid oxide fuel cells (SOFC), thin films of electro-chromic stuff, optical polishing agents, luminescence, UV adsorbents, water splitting, photocatalysis, luminescent materials and sensors [16-20]. Moreover, CeO_2 is also believed to be a strong candidate for spintronics nano devices due its similar characteristics with silicon (Si) likewise its crystal structure, lattice parameters and compatibility with micro-electronic devices [21].

1.2 CeO₂

CeO₂ is the most abundant REMO existing in the Earth's crust about 66.5ppm which is higher value of abundance than copper, cobalt and lithium [22]. It is a wide band gap (3.2 eV) ceramic material with cubic fluorite crystal structure and owing room temperature large free exciton binding energy (58 meV). It has attained an immense attention because of its technological applications in the fields of electronics, spintronics, optoelectronics and magnetic data storage devices originated from its partially 4f filled electronic structure [23]. It is vastly used in semiconductor devices technology as phosphor and luminescent material as it owns the features of both activator as well as hosts [24]. It is insoluble in water but soluble in some strong acids. Due to these incredible properties, CeO₂ is vastly explored for applications in various fields such as antibacterial agents, an ionic conductor, as a gas sensor, an electrolyte material of solid oxide fuel cells (SOFCs), luminescence, optical polishing agents, UV adsorbents, humidity sensors, targeted drug delivery, photo catalytic activities, automotive exhaust catalysts, high oxygen storage capability and high storage capacitor devices [25-35].

1.2.1 Fundamental properties of CeO₂

Some of the basic physical properties of bulk CeO₂ at room temperature are listed in table 1.1.

Table 1.1: Basic physical properties of CeO₂ at room temperature [36-38]

Physical Property	Value (unit)
Crystal structure	Cubic fluorite
Space group	$Fm\bar{3}m$
Lattice Parameter	5.41134Å
Asymmetric units	Ce (0,0,0) O ($\frac{1}{4}, \frac{1}{4}, \frac{1}{4}$)
Band gap energy	3.19eV
Density	7.22 g cm ⁻³
Melting point	2750 K
Specific heat	460 J kg ⁻¹ K ⁻¹
Thermal conductivity	12 W m ⁻¹ K ⁻¹
Refractive index	2.1 visible 2.2 infrared
Dielectric constant (0.5–50 MHz)	11
Young's modulus	1.65*10 ¹¹ N m ⁻²
Poisson's ratio	0.3
Hardness	5–6

1.2.2 Crystal structure of CeO₂

Cerium (Ce) has two stable oxidation valence states i.e. Ce³⁺ and Ce⁴⁺. Its oxide is one of the most important oxide material due to the switching of oxidation states between Ce³⁺ and Ce⁴⁺ which is known as redox reactions. CeO₂ has a cubic fluorite structure with space group $Fm\bar{3}m$ and a cell parameter of 5.41134Å at room temperature as shown in Fig. 1.2 [39].

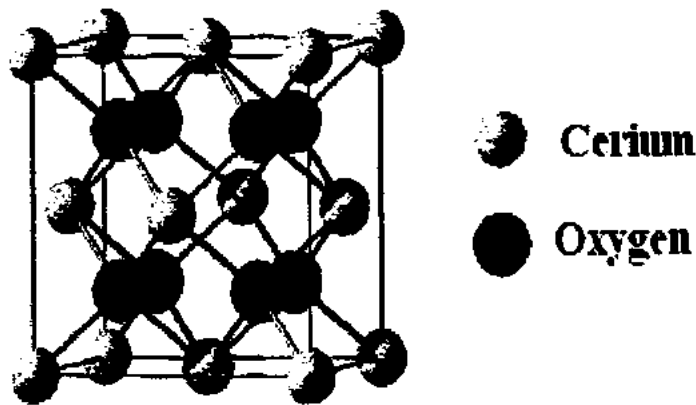


Figure 1.2: The face centered cubic cell of fluorite CeO₂ [39].

Generally, the ionic compounds having RX₂ form such as CaF₂ crystallizes into cubic fluorite structure if the ratio of ionic radii satisfies equation 1.1 given as follows:

$$\frac{r(X^-)}{r(R^{2+})} \leq \frac{\sqrt{3}+1}{2} \text{ or } \frac{r(X^-)}{r(R^{2+})} \leq 1.36 \quad (1.1)$$

If the values for ionic radii of O and Ce ions are inserted in equation 1.1, we get the value less than or equal to 1.36 which demonstrates that these ions will crystallize in cubic fluorite structure. The crystal structure of CeO₂ is comprised of a cubic close-packed array of Ce ions coordinated by 8 oxygen ions. Each Ce atom is surrounded by eight equivalents nearest neighbor O atoms. The O atoms are further surrounded by a tetrahedron of four equivalent Ce atoms [40]. The fluorite structure is relatively open with large ($\frac{1}{2}, \frac{1}{2}, \frac{1}{2}$) octahedral holes and shows large tolerance for atomic disorder due to substitution, reduction or oxidation etc. The

O ions reside in tetrahedral holes generated by Ce^{4+} ions as shown in Fig. 1.3(a). This can also be narrated as one Ce ions is located in center of a cube having O ions on corner of it as shown in Fig. 1.3(b). In this fig, there are diagonal planes of the cubes with cations in it which are known as octahedral holes in the system. These holes are responsible for allowing defects to hop or jump through the host lattice.

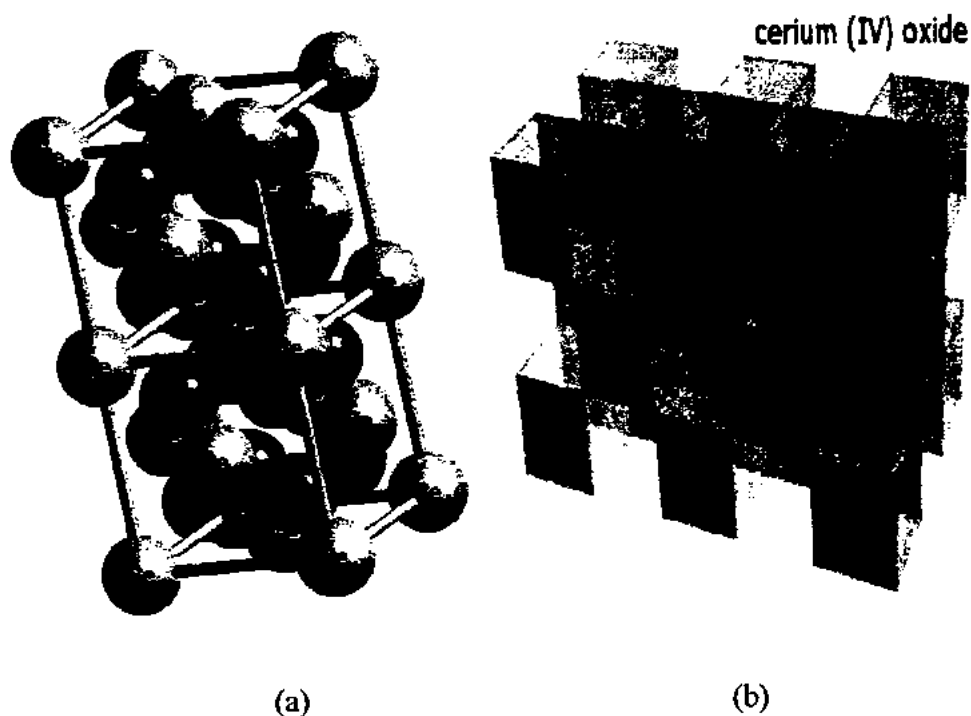


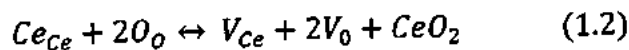
Figure 1.3: The crystal structure of CeO_2 ; (a) two unit cells (b) alternate view [41].

Previous work suggested that the most stable surface termination is normally the low index (111)-termination. This low index surface is followed by comparatively less stable (110) surface and then the high energy surfaces such as (100), (210) and (310) [41, 42]. During the crystal growth, CeO_2 commonly exposes (111) surface because of its higher stability. The other less stable surfaces such as (110) and (100) surfaces exposure is followed after (111) surface. The type of the exposed surface is very important for catalytic applications of CeO_2 likewise the (100) terminated surface is more reactive as compared to (111) terminated surface. Moreover, it is reported earlier by Conesa et al., that the amount of

energy required for the formation of V_o is lesser on (110) and (100) as compared to that on (111) [42]. The exposure of surfaces type strongly depends on shape of crystal. K. Zhao et al., have reported that (001) and (110) surfaces are exposed in case of CeO_2 nanorods [43]. Similarly, CeO_2 nanopolyhedrans expose (111) and (100) surfaces while (100) surface is explored in case of nanocubes [44]. Hence, strict control over the shapes of CeO_2 nanostructures is required for desired catalytic activities and formation of V_o . The later one is important for RTFM ferromagnetism of CeO_2 nanostructures. This can be achieved by controlling the synthesis parameters and use of certain capping agents.

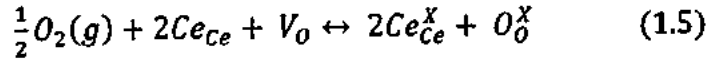
1.2.3 Defects chemistry of CeO_2

The defects chemistry of CeO_2 is relatively well established. The defects can be produced in CeO_2 both intrinsically and extrinsically. Intrinsic defects are produced via thermal disorder or host reaction with environment. There are two main defect types in CeO_2 , V_o and small polarons. The formation of intrinsic V_o is governed by Kroger and Vink notations which are given below;

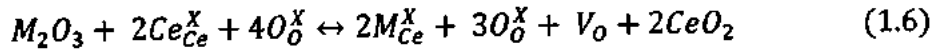


Where Ce_{Ce} is Ce at Ce site, O_o is O at O site, Ce_i is Ce at interstitial sites and O_i is O at interstitial sites. It is believed that V_o are formed in order to compensate the charge produced by reduction of Ce^{4+} to Ce^{3+} . This introduction of the V_o in the system will lead lattice expansion of host matrix as ionic radii of Ce^{3+} is larger as compared to that of Ce^{4+} . The second type of defects i.e. polarons are created when electrons migrate through host, it polarize the lattice which in return for the potential well that traps the electron. This type of

defects is explained by equation (1.5) which is given for quasi particles. Actually, polarons are type of quasi-particles.



Where Ce_{Ce}^X representing the small polaron. The polarons can be produced in the CeO_2 both intrinsically and extrinsically. In undoped or pure CeO_2 , dilute solution approximation breaks down when the value of oxygen non stoichiometry is above 0.001 while is unstable in doped CeO_2 up to the values of 0.03-0.04. This means that defects are more pronounced in doped CeO_2 . Defects can be formed in CeO_2 host matrix via doping. For example if we dope a trivalent ions in the host structure then CeO_2 defects chemistry will governed by the equation (1.6);



Where M_2O_3 is a trivalent dopant and M_{Ce}^X is dopant ion on the sites of host ions.

The concentration of oxygen vacancies C_{V_o} and concentration of electrons C_e must satisfy the equilibrium conditions set by the relation(1.7);

$$K_r = \frac{C_e C_{V_o}^2 P_{O_2}^{\frac{1}{2}}}{[O_o^X]} \quad (1.7)$$

Where O_o^X is the concentration of oxygen sites while K_r is Arrhenius expression. The dopant must obey the neutrality at sample equilibrium which is given by;

$$B + C_e = 2C_{V_o} \quad (1.8)$$

Where B is equilibrium constant which depends on the valancy of the dopant. The concentration of V_o and polarons (trapped electrons) in CeO_2 can be tuned via selective doping, as type of the dopant is very crucial in this regard.

1.2.4 Specific surface area (SSA)

SSA is the characteristic of the solids which is the total surface area offered by a material per unit mass and is measured in m^2/g . It is usually determined by physical adsorption of a gas on the surface of the solid. The amount of adsorbed gas gives the value of SSA. SSA vastly determines many physical and chemical properties of materials. Physical adsorption of molecules, heat loss or gain due to that adsorption, shrinking and swelling and many other physical and chemical manners are closely linked to SSA. Furthermore, surface or exposed area is also a strong controlling factor in many biological processes.

NPs have a much greater SSA than the identical mass of materials at the micro-scale [46] which enhances the proportion of atoms or molecules available on the surface in contrast to the interior of the material [47]. It is well evident from Fig. 1.4 that as particle size of a material decreases, the SSA exposed to the environment increases. Moreover, increasing the SSA of a material leads to enhancement in the abundant reactive sites on the surface of NPs [48] as well as the available surface free energy [49]. It is reported that magnetic properties are also linked with SSA of a material. When materials are scaled down from bulk to nano, large fraction of defects and less coordinated atoms are available on the surface which strongly influence the magnetic properties of the material. The increase in SSA may also increase or decrease the ferromagnetism mediated through defects. According to Kodama et al., smaller the particle size more will be the FM effects in oxides nanoparticles [50] while for some metallic nanoparticles, this case is reversed [51]. It is a well-established fact that increased SSA may [52] or may not [53] enhance the cytotoxic mechanisms as a function of particle size alone. A higher surface energy makes the NPs able to interact and agglomerate which may result into the reduction of the NPs bioavailability [18]. It is also noticed that as we make a transition of a particle from macroscopic level to its atomic domain i.e. nano

scale, its reactivity is changed (increase or decrease) which depends on the nature of material and the type of chemical reaction.

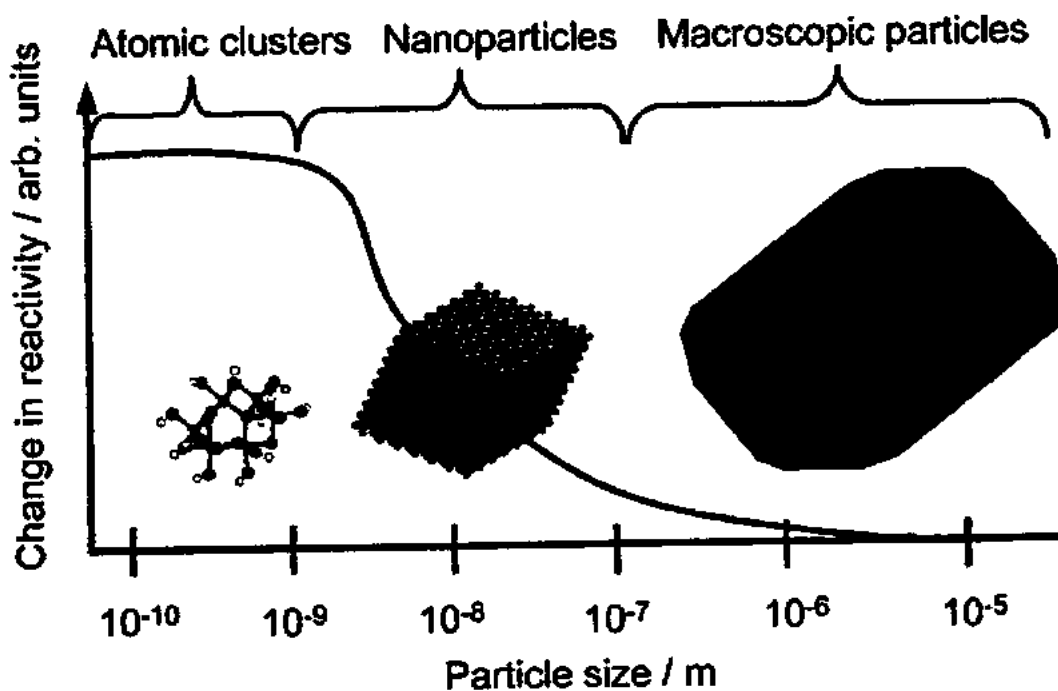


Figure 1.4: Generalized size-dependent reactivity of a material [54].

1.2.5 Optical properties of CeO₂

Optical characteristics of a material are very much important in determining its potential applications in many functional devices. Therefore, controlling the optical properties are of utmost importance. CeO₂ is a wide band gap semiconductor and can be activated by only UV light. The band edge absorption in CeO₂ occurs from the transition of electron between O 2p and Ce 4f bands. The band energy of CeO₂ is also particle size and shape dependent. When material is scaled down from bulk to nano, band gap energy increases which may be linked with quantum size confinement effects. This phenomenon occurs due to the variations in band structure of material at nanoscale. The typical quantum confinement regimes defined to be 1 to 25 nm in various metal oxides nanomaterials [55, 56]. When the spatial extent of electronic wave function approaches the particle size then

electrons can feel the boundaries or edges of the particles. By this, electron tends to adjust its energy as function of particle size. This adjustment as function of particle size is known as quantum size confinement effects. This effect is more pronounced when the particle size is comparable to the Bohr exciton radius of the material. The Bohr exciton radius of a particle is given by a relation [57];

$$\mu_B = \varepsilon' \frac{m}{m^*} \mu_0 \quad (1.9)$$

Where m is the rest mass of an electron, m^* is the effective mass of a particle, ε' is the dielectric constant of the medium and μ_0 is the Bohr radius. When particle sizes approach the Bohr radius, quantum size confinement effect leads to enhancement in excitonic transition energy and blue shift in the absorption edge. The quantum confinement effect also transforms the continuous energy bands into discrete energy bands as shown in Fig. 1.5

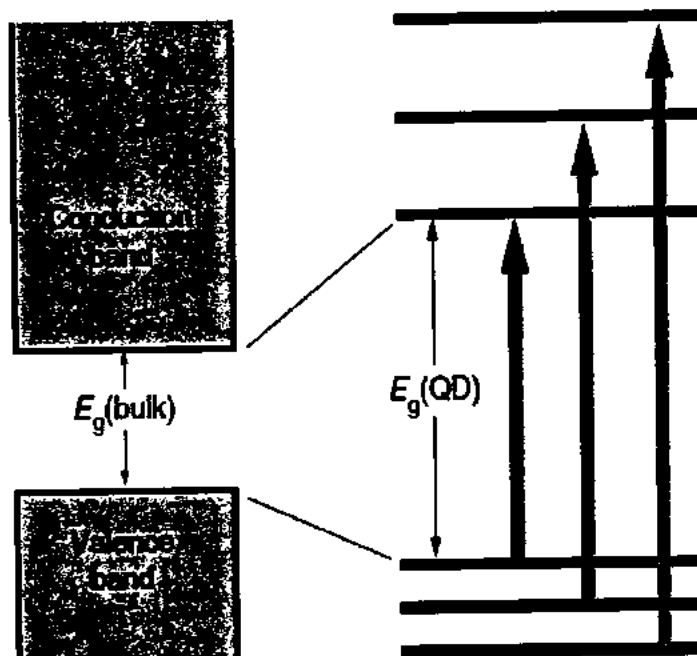
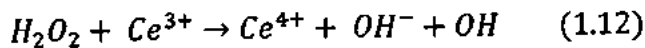
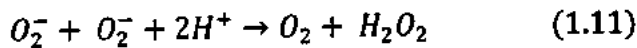
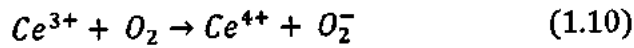


Figure 1.5: A schematic of the discrete energy levels of a semiconductor [58].

A strong quantum confinement effects is observed for CeO_2 nanomaterials by several research groups [45, 59]. The band gap engineering of CeO_2 nanostructures is also achieved by selective doping [60]. The dopant can either increase or decrease the band gap energy of CeO_2 nanostructures depending on type and concentration of dopant [60-63].

1.2.6 Redox chemistry of CeO₂

CeO₂ is very important functional material having interesting redox chemistry with two oxidation states of Ce⁴⁺ and Ce³⁺. It has the ability to cycle between the two under the ambient conditions. The reduction of Ce⁴⁺ to Ce³⁺ and vice versa leads to formation of defects especially V_o [43, 64]. This interesting feature makes it potential for catalytic and biological applications. The Ce³⁺ ions can interact with oxygen and form Ce⁴⁺ and oxygen radicals. These oxygen radicals interact with H⁺ and generate hydrogen peroxide (H₂O₂) which may be lethal for biological cells such as bacterial and cancerous cells. These H₂O₂ may interact with Ce³⁺ ions and leads to generation of Ce⁴⁺ ions and hydroxyl radicals (OH⁻). These hydroxyl radicals are also toxic for cancer lines and environmental pollutants. All these phenomenon are explained in the below reactions [65, 66].



This redox property of CeO₂ is usually exhibited at nanoscale which makes it very important nanomaterial for catalytic and biological applications.

1.2.7 Vibrational properties of CeO₂

In order to understand and explore the physical properties of a material, it is very essential to have an exact idea about its vibrational properties. Raman spectroscopy is a very handy tool to have an exact knowledge about the vibrational modes of CeO₂. Raman modes of a material are only active if one of the polarizability components varies during irradiation by the laser in the Raman spectroscopy. It is well known fact that CeO₂ possesses various Raman vibrational modes. Interestingly, CeO₂ owns *Fm* $\bar{3}$ *m* space group with cubic fluorite

structure which is linked with point group O_h^5 [67]. It is reported that O_h point group in CeO_2 molecule possesses three axes having two-fold rotational, four axes owing three-fold rotational and an inversion symmetry. The allowed symmetries for this point group indicate that CeO_2 has three vibrations A_{1g} , E_g and F_{2g} which are Raman active. Some frequencies of vibrational modes are inactive and they are estimated from the combined analysis of combinational and overtone bands. It is reported that, Raman spectra of CeO_2 usually exhibit a sharp line on 465cm^{-1} which is related to first order F_{2g} mode [68]. Additional observed features in CeO_2 Raman spectra are linked with the second order combinations of the other active vibrational modes such as (A_{1g} , E_g and F_{2g}). These comprise some weak bands at about 207, 250, 428, 578 and 1174 cm^{-1} [69].

The Raman vibrational modes of CeO_2 are strongly linked with dopant type, its concentration and also with the crystal defects. It is reported in literature that Raman peak shift, suppression in peak intensity and broadening of F_{2g} active mode peak are associated with the phonon confinement effect due to small particle size, presence of V_o and interstitial defects etc. in the host matrix [70, 71]. Thus, Raman analysis (Raman mode peak position, broadening and intensity suppression) is a very vital tool to gather important structural information about CeO_2 nanostructures.

1.2.8 Magnetic doping of CeO_2

The first generation of spintronics devices was based on passive magnetoresistive sensors and memory elements using electrodes made from alloys of ferromagnetic 3d metals. The discovery of giant magneto-resistance in Fe/Cr based multilayers, later on, boosted the development of these spintronics devices [72]. Next generation of spintronics devices having more sophisticated and advanced features may be based on the introduction and manipulation of spin polarized electrons in metal oxide hosts. The functionality of these devices requires the spin polarization of electrons and their preservation throughout the host matrix [73]. This

can be achieved by the introduction of minute amount of magnetic elements in the metal-semiconductor junctions. These types of spintronics devices have been widely explored but they lack the long range preservation of electron spin through the interface. This drawback has been attributed to the difference in the electrical conductivities of the metal and semiconductor [74]. Hence, development of materials having both semiconducting and ferromagnetic (FM) properties is a great challenge these days.

Dilute magnetic semiconductors (DMSs) have been emerged as a potential candidate for this purpose. DMSs are actually nonmagnetic semiconductors doped with very few percentages of magnetic metal elements. Transition metal (TM) elements are considered to be the best dopants in this context. The TM dopants must produce spin polarized electrons in the host as well as their long range preservation. The challenge is big because of the introduction of both electronic and magnetic dopants at the same time and engineering of the interaction between dopants spins and free carriers in order to have thermally robust dopant and spin carrier coupling. Fig. 1.6 depicts the schematic representation of a magnetic, nonmagnetic semiconductor and DMS.

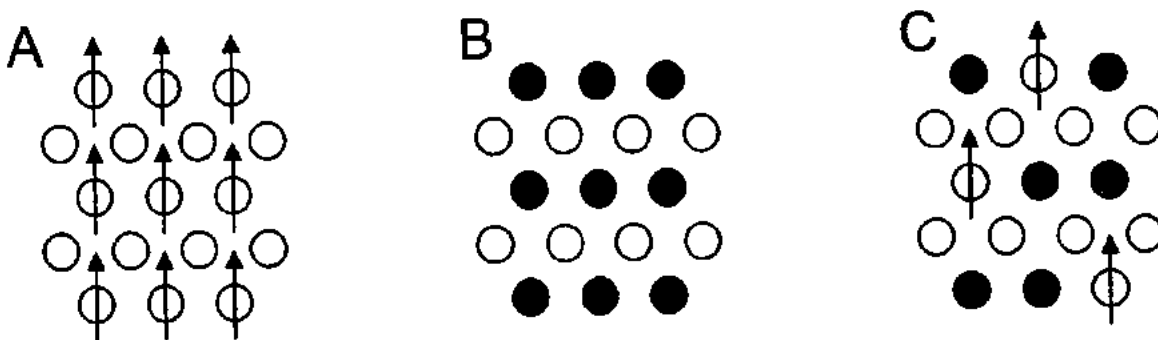


Figure: 1.6: Illustrating (A) a magnetic semiconductor, (B) a non-magnetic semiconductor material, and (C) a diluted magnetic semiconductor [75].

The first DMSs were group II-IV semiconductors doped with magnetic elements. The drawback of these DMS is that they exhibit FM at very low Curie temperature (T_c) i.e. few

Ks [76]. Therefore, they are not considered to be the best candidates for spintronics devices. The TM ions doped group III-V semiconductors have also exhibited FM at T_C of 173 K which is far low from the required room temperature [77, 78]. The FM in all these TM doped semiconductors were carriers mediated which enables the modification of ferromagnetic behavior through charge manipulation. This behavior has encouraged the researchers to search for carrier mediated ferromagnetic semiconductors with high T_C . TM ions doped metal oxides based DMS may be the ideal materials for spintronics devices. In this regard, the ground breaking discovery was RTFM in Co doped TiO_2 system [79, 80]. This discovery triggered the research for RTFM in other TM doped metal oxides such as ZnO [81], SnO_2 [82], Cu_2O [83], In_2O_3 [84] and CeO_2 [85-88] etc. The table 1.2 lists the TM doped metal oxides based DMS with Curie temperature and respective magnetic moments. The CeO_2 based DMS are interesting because of its RTFM with sufficient M_s value, similar properties with that of Si and compatibility with micro-electronic devices [21]. Moreover, it has excellent redox characteristics which make it suitable for therapeutics. The combination of anticancer characteristics along with RTFM makes it potential for targeted cancer therapy [43, 64-66]. The origin of RTFM in these TM doped CeO_2 is still not clear, It is debatable, whether the RTFM is due to the direct interactions between TM ions local moments in the magnetic impurity cluster or it is the intrinsic originated from the exchange interactions between spin of the carriers and local moments of TM ions. It is very important issue as spintronics devices require only intrinsic FM order. There are number of experimental proofs for the carrier mediated RTFM in TM doped oxides especially in CeO_2 [88-91]. From the proposed theoretical models, it can be observed that formation and distribution of V_o is of utmost importance for RTFM of CeO_2 based DMS. It has been suggested that introduction and distribution of V_o in the host unit cell may enhance their ferromagnetic behavior and vice versa [90, 92]. This case is supported by bound magnetic polaron (BMP) model. According

to this model, when V_o is formed, the electrons of the cations donated are shared by the oxygen atoms or anions are no longer attached to any atom. This makes them loosely bonded to V_o site considered as hydrogen like orbitals and constitutes a polaron. The dopant ions which are magnetic ions tend to form a BMP by interacting with the V_o , coupling the moments of the ions within their own orbitals. The basic idea of BMP model is illustrated in Fig. 1.7. The nature of the coupling between V_o and magnetic ions which defines the nature of magnetic order to be constituted is dependent on the valence state of the dopants i.e. whether it is less than or more than half full or half full. Moreover, the coupling between the dopant magnetic ions always gives ferromagnetic order. The ϵ' and effective mass of the host ions determines the radius of the polaron as depicted in equation (1.10). At critical concentration of polarons percolation is achieved where the whole network of the polarons and TM ions are interlinked which leads to RTFM.

Table 1.2: Some reports on high T_c oxide-based DMSs [79-88]

Material	Doping (x)	Moment ($\mu_B/3d$ ion)	T_c (K)
TiO₂	Co, 1-2%	0.3	> 300
	Co, 7%	1.4	650 - 700
	V, 5%	4.2	> 400
	Fe, 2%	2.4	> 300
ZnO	Co, 10%	2.0	280 - 300
	V, 15%	0.5	> 350
	Mn, 2.2%	0.16	> 300
	Fe, 5% - Cu, 1%	0.75	550
	Ni, 0.9%	0.06	> 300
SnO₂	Co, 5%	7.5	650
	Fe, 5%	1.8	610
Cu₂O	Co, 5% - Al, 0.5%	0.2	> 300
In_{1.8}Sn_{0.2}O₃	Mn, 5%	0.8	> 300
	Co	1.1	870
CeO₂	Co (0%, 1%, 3%)	1.2, 1.7, 1.1	> 300
	Fe (0%, 3%, 5%)	1.2, 1.4, 2.1	> 300

More recently, various groups have suggested that the combination of indirect exchange interactions explained by Ruderman-Kittel-Kasuya-Yosida (RKKY) model and percolation of magnetic polarons are responsible for FM in CeO₂ based DMS at high temperature [89, 90, 92]. Thus it is more obvious from this discussion that the exact origin of RTFM in TM doped metal oxides DMS is still very controversial.

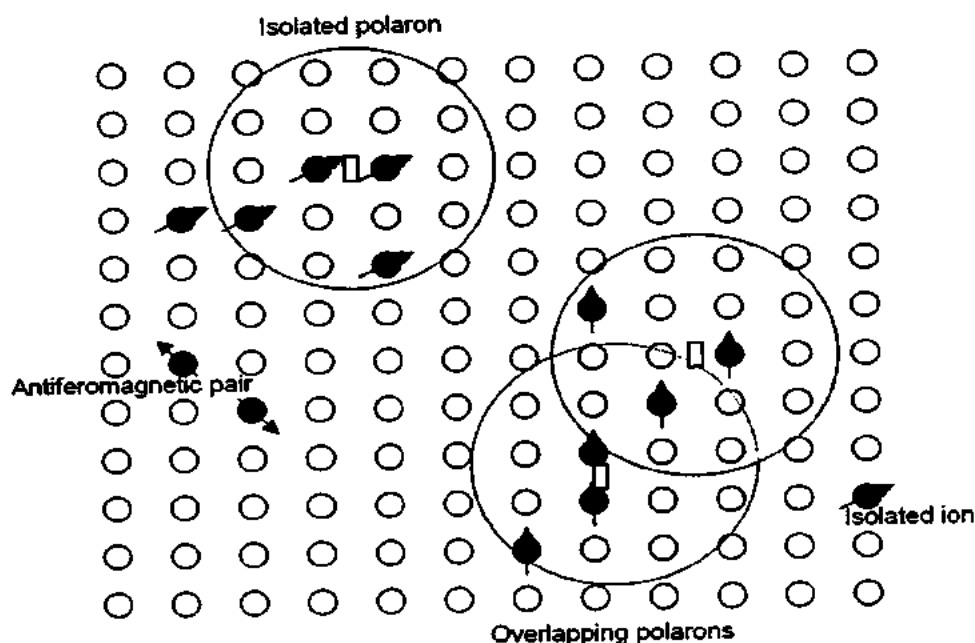


Figure 1.7: Polaron percolation model as illustrated by Coey *et al.* [88]

1.2.9 Biological activity of CeO₂

Inorganic nanoparticles show stable physical and chemical properties which make them a suitable candidate for use in biological assays to remove or minimize the shortcomings of organic fluorophores, natural enzymes or radioactive labeling as they are photobleachable, toxic and are easily degradable, respectively [93]. Furthermore, it is noticed that inorganic NPs comprise well improved reactivity as they have high penetrating power against different tissues and cell membranes. In spite of all above mentioned features of inorganic NPs, it is a great challenge to control the toxicity of these NPs towards healthy cells as they owe very low physical and chemical stability at high pressure and temperature conditions [94, 95].

Cancer is categorized as the uninhibited growth of cells and is one of the main causes of expiries in worldwide over a last few decades [96, 97]. Developments of suitable medicines for cancer therapy have yet been a great challenge for scientists and researchers especially against nervous system cancer cell line Neuroblastoma (NB) which is one of the

most common and hazardous kind of cancer existing in children [98]. Treatment to a high-stage NB is a big challenge because of its high resistance against chemotherapy as well as numerous patient relapses. Currently employed therapeutic schemes against NB involve multi-nodal approaches which includes radiotherapy, surgery as well as immuno and chemotherapy [99]. Such a high dose intensive chemotherapy involving myoablative treatments have severe toxic side effects with long term consequences like hearing and vision complications [100, 101]. NB treatment demands alternate effective approaches to tackle it.

Recently, it has been reported that various nanomaterials have great potential for NB cancer therapy because of their unique physiochemical properties and biological activities [NB]. These nanomaterials have the potential to interact exceptionally with biomolecules existing on the surface as well as inside of the cells due to their enormous smaller sizes as compared to biomolecules [102, 103]. Furthermore, among the plenteous types of nanomaterials, family of magnetic nanomaterials have exposed great potential in targeted cancer therapy because of their distinctive behavior in magnetic field [104]. These magnetic nanomaterials, Fe_3O_4 , Fe_2O_3 , CoPt etc., are highly efficient as they can be guided to the specific part of the body using external applied magnetic field for cancer diagnostics and therapy [105-108]. But their potential applications are hinders as they are highly toxic towards the healthy cells at higher concentrations [109, 110]. Thus, to overcome these discrepancies, new approaches for safer cancer therapy are severely needed to be exploited. Good substitute for that purpose are metal oxide (MO) nanomaterials as they have harmless and nontoxic nature towards healthy cells reported by various research groups [106, 111]. Anticancer activity of pure CeO_2 nanoparticles has been reported by various groups [112, 113] but undoped CeO_2 nanoparticles exhibit weak ferromagnetism which hampers its application in targeted cancer therapy [114]. A strong enough ferromagnetism can be originated in CeO_2 nanoparticles via selective doping of transition metal (TM) [115].

Furthermore, TM doping into CeO₂ nanoparticles matrix can lead to enhanced V_o formation which are very important for inhibition of cancer cells by nanomaterials [84]. An illustration of magnetic nanoparticles base cancer therapy is given below in Fig. 1.8.

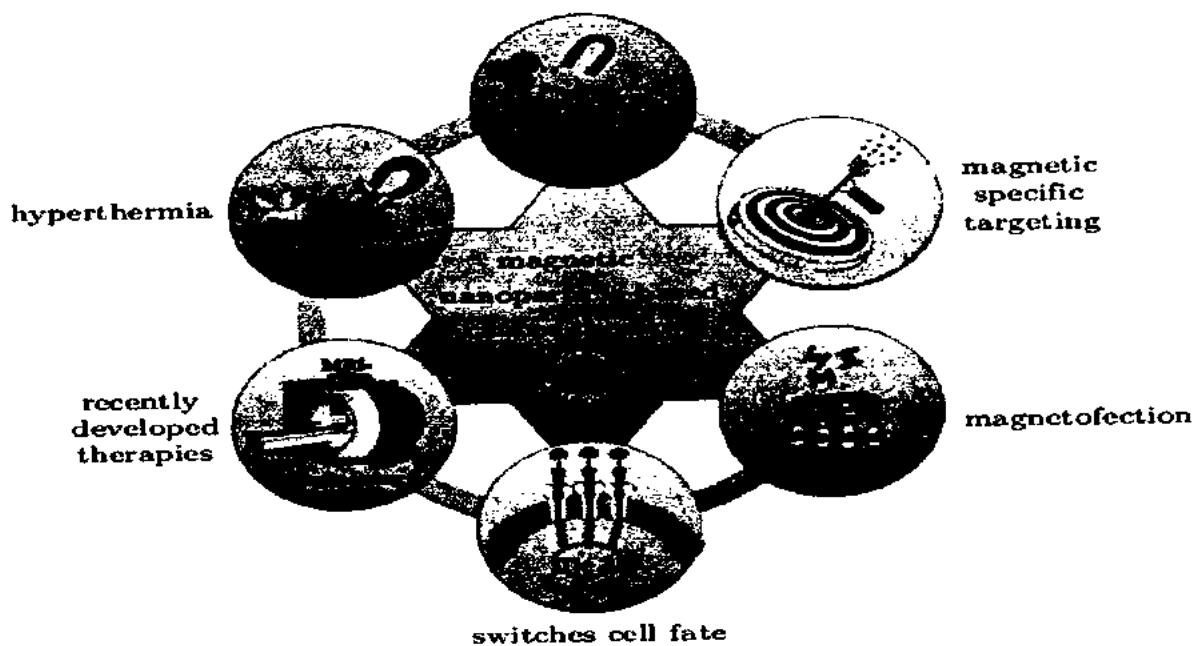


Figure 1.8: Magnetic nanoparticle based cancer therapy [105].

In CeO₂ structure, there exists two different ionic states (Ce³⁺, Ce⁴⁺) at the same time prompting V_o formation at its surfaces. This make CeO₂ nanostructures a vital nanomaterial for various biological applications [113]. These fascinating features of CeO₂ nanoparticles make them a potential for reactive oxygen species (ROS) generation which in turns plays a vital role for judgment of anticancer activity [116]. By illumination of light on CeO₂ nanoparticles, electron-hole pairs are generated and due to their interaction with oxygen on the surface and water molecules, various types of ROS (super oxides anions, super oxides radicals, hydroxyl radicals, H₂O₂ etc.) is generated [117]. It is a well noticed fact that cytotoxicity of CeO₂ nanoparticles is highly sensitive to ROS generation [118]. The generated ROS may result in to cell death by means of various mechanisms such as apoptosis, lipid peroxidation and cell membrane damage [119, 120]. The short half-life of electron hole pair is the main hurdle in this process as they recombine before interacting with the water and

oxygen. It is reported that introduction of various dopants in the host matrix can create defects in nanomaterials which act as trapping centers for photo dynamically produced electrons causing enhancement of ROS generation [121, 122].

Fig. 1.9 illustrating the importance of material composition, bonded surface species, electronic structure, surface coatings, solubility and the contribution of interactions with other environmental factors (e.g. UV and visible light activation).

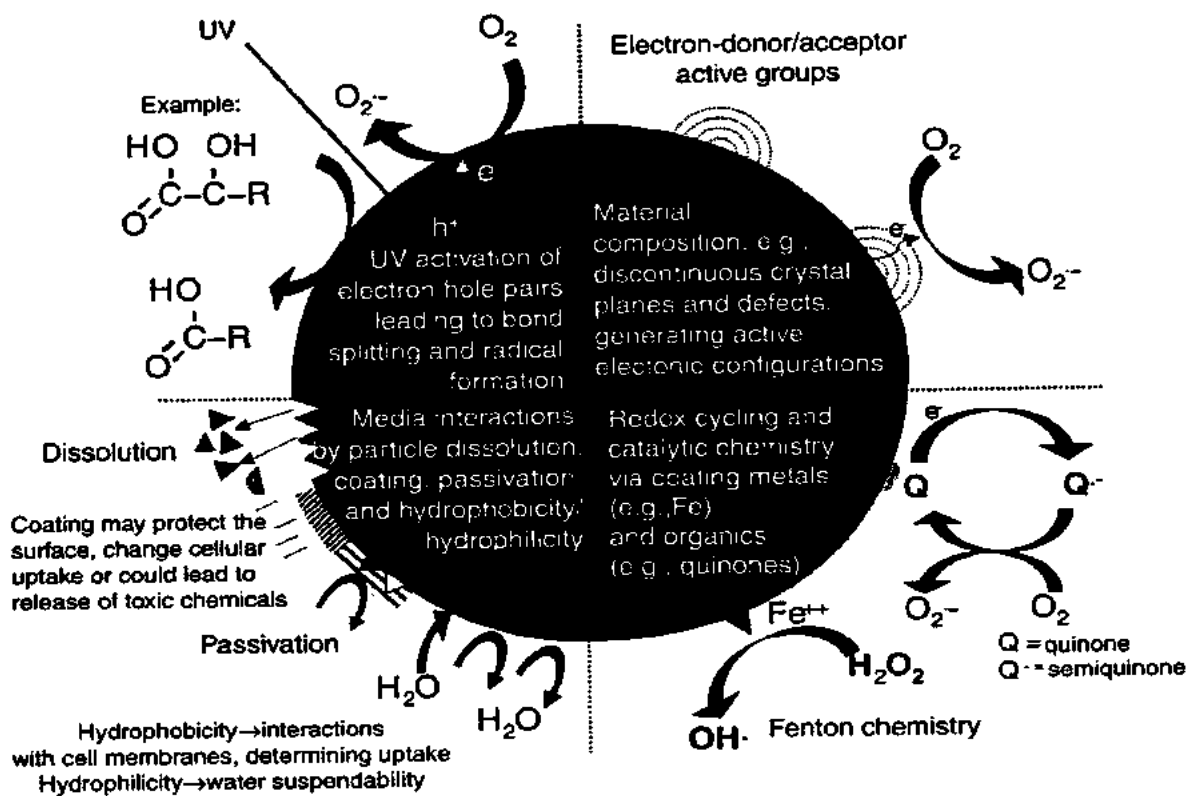


Figure 1.9: Possible mechanisms by which nanomaterials interact with biological tissues

[123].

1.3 Statement of Problem

The development of nanotechnology devices has recently become one of the most emerging fields of research in the physical sciences. Enhancing the surface area without increasing the device dimension leads to more efficient devices based on surface controlled phenomena such as in solar cells, sensors, detectors, targeted drug delivery, antibacterial

agents and photocatalysis. Numerous research groups have developed techniques that utilize metal oxide nanostructures to fabricate devices. However, widespread utilization of nanotechnology is often hindered by the conflicting demands for precise control of size, shape, morphology, their physical properties and low-cost mass production. It is therefore necessary to develop and establish a technology that allows for rapid low cost production of high surface area nanostructures with desired properties. Soft chemical routes are low cost versatile methods which can be used to synthesize CeO₂ nanostructures. Furthermore, the different properties of the CeO₂ nanostructures need to be tailored according to the demands.

Despite multiple research approaches, the cancer and its hazards are serious issues worldwide. This requires the development of new novel anticancer agents instead of radiation therapy which have selective toxicity towards various cancer cell lines. In this regard, numbers of MOs nanostructures such as TiO₂, ZnO, CeO₂, CuO, SiO₂, SnO₂ and MgO have shown great potential due to their toxic nature towards cancer cell lines without harming healthy cells. Among these CeO₂ is thought to be most stable and active anticancer agent due to its excellent redox activity. The major problem is that the cancer activities of all of these MOs are still very low which needs to be enhanced by introducing dopants, defects, impurities and tailoring of optomagnetic properties.

1.4 Aims and Objectives of the Thesis

- ❖ Synthesis of CeO₂ nanostructures with controlled particle size and morphology by a simple, cost effective and easily reproducible coprecipitation technique.
- ❖ Optimization of various synthesis parameters (such as reaction temperature, reactants, morality etc.) in order to get ultrafine and uniform nanostructures.
- ❖ Successful doping of TM ions at cationic site of host matrix of CeO₂.
- ❖ Tailoring of physical properties of the prepared CeO₂ nanostructures by introducing different impurities such as

- i. **Control over the size and shape of nanostructures.**
- ii. **Introduction of structural defects**
- iii. **Tuning of optical bandgap to make it visible light activated and luminescent material.**
- iv. **To enhance FM at RT for spintronics devices and target cancer therapy.**
- v. **Improving dielectric property to utilize in EMW gate material etc.**
- vi. **Enhancing anticancer activity against most hazardous and complicated cell lines.**

Chapter No.2

Synthesis and Characterization Techniques

2.1 Nanotechnology and Nanomaterials

Nanotechnology is the technology of design, synthesis and applications of nanostructured materials. It is a vital technology which helps us to understand as well as to tune the physical and chemical properties of the nanomaterials. Nanomaterials are the materials having at least one dimension in the range of individual atom or molecule to submicron. These materials are quite different in physicochemical as well as in applications as compared to their bulk counterpart. At nano scale, discovery of novel materials, processes, versatile phenomena, new theoretical and experimental approaches regarding research make us able to provide a plenty of innovative and fruitful nanostructured materials. Now it is possible to synthesize unique and desired nanostructured materials. In fact this field has opened new corridors and venues in science and technology.

2.1.1 Size effects

Nanomaterials are distinguished from their bulk counterparts on the basis of size difference. Upon diminishing the particle size, various properties of nanomaterials are distinctly enhanced and tuned which in turns make them a class of novel materials owing tremendous new practical applications. This tuning of various physicochemical properties is linked with the fact that the reduction of particle size results into enhanced performance of surface atoms as their surface to volume ratio (surface area) increases [124]. This fact is well elaborated in the Fig. 2.1. It is obvious from the figure that surface atoms effect becomes more dominant when palladium particle size is scale down to 10nm. Furthermore, it is observed that unexpected and improved catalytic activity of metal nanoparticles is achieved

with diameter ranging from 1-2nm in catalysis of gold nanoparticles while it is a fact that gold is chemically inert in bulk form [125].

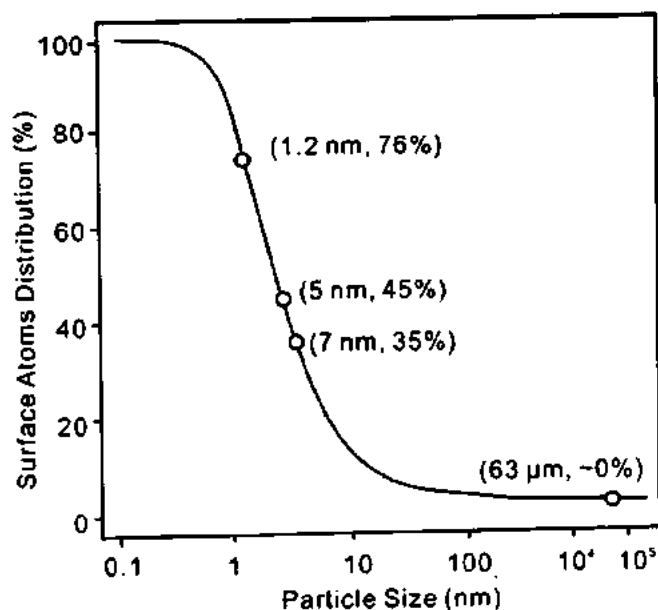


Figure 2.1: The plot of percentage of surface atoms as a function of particle size [124].

2.1.2 Classification of nanomaterials

Nanomaterials are generally categorized into three major types: zero, one, and two dimensional nanostructures.

- Zero-dimensional nanostructures include nanoparticles, single crystal, amorphous as well as polycrystalline particles with variety of morphologies like cube, sphere and platelets owing all dimensions less than 100 nm range. The interesting feature of zero-dimensional nanostructures is that they are referred as “quantum dot” when their particle sizes are sufficiently small (<10 nm) and quantum confinement effect is perceived.
- One-dimensional (1D) nanomaterials involve the nanomaterials having two dimensions lesser than the 100 nm range. 1D nanomaterial includes nano wires, nano tubes, nano rods, nano fibrils or fibers and nano whiskers. It is found that nano fibers

exhibit a higher aspect ratio (length to thickness ratio) as compared to nano rods or whiskers.

- Two-dimensional (2D) nanomaterials are the materials having only one dimension in the range of nanoscale (<100nm). Nano-sheets and thin films are the typical examples of these kinds of nanomaterials.

2.2 Synthesis Techniques

Novel physical properties and potential application of nanostructured materials can be explored by controlling their particle size, surface area and morphology. Generally speaking, the method employed is the key factor which determines the above mentioned characteristics. Thus ability to develop dynamic fabrication techniques to synthesize desired nanomaterials is very essential. Their controlled fabrication can be achieved in numerous ways. We can make a broad classification which divides these synthesis techniques into either built from atom by atom (bottom up) or constructing them from reformation of atoms from bulk (top down). A schematic representation of both approaches is shown in Fig. 2.2.

2.2.1 Bottom-up approach

Bottom-up approach is the self-assembly of desired nanomaterials from the bottom: atom by atom, molecule by molecule or cluster by cluster. This technique is capable to synthesize engineered nanostructures having perfect edges and surfaces. It is possible to engineer the functionalities of overall nanostructured systems by controlling the size, morphology and internal as well as surface chemistry of the constituent's basic building blocks. Some typical examples of bottom-up approaches are: chemical co-precipitation, self-assembly, sol-gel, hydrothermal, solvothermal, thermal evaporation, chemical vapor deposition (CVD), physical vapor deposition (PVD) and gas phase agglomeration etc. [126].

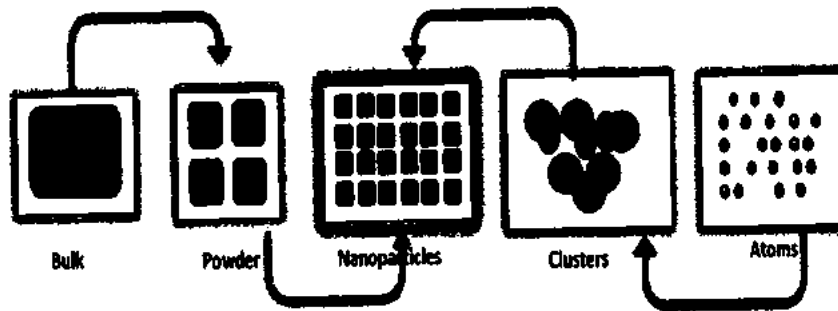


Figure 2.2: A Schematic representation of the top-down and bottom-up approaches

2.2.2 Top-down approach

This approach is the inverse of bottom-up approach and it involves successive slicing or cutting of a bulk material to achieve nano sized materials. The various synthesis techniques to fabricate nanostructured materials involving this approach are: ball milling (mechanical milling, cryomilling and mechanochemical bonding), embossing, etching, printing, molding, skiving, erosion and lithography etc. Top-down approach is however, a bit disadvantageous as it has a very limited control over morphology, particle size, possessing wide particle size distribution and time taking. Moreover, a biggest problem with this approach is the occurrences of surface structure imperfections and also the processed crystallographic patterns are damaged significantly. The existence of these imperfections in this approach is a big challenge in the design and fabrication of potential nano devices. On the contrary, bottom up approach is very handy and is free from these drawbacks. Furthermore, the desired structure of nanomaterials with the appropriate properties can easily be synthesized via this approach. Hence most of the researcher tends to prefer bottom-up approaches.

CeO₂ nanostructures are of great interest for researchers with a host of technological applications, for example, catalysts to eliminate toxic auto exhaust gases, fuel cells, oxygen sensors, electrochromic thin films, various biological applications [127]. As all of the useful

applications of CeO₂ nanostructures are strictly dependent upon the morphology, particle size and surface area of the nanostructures. In order to tune the properties of CeO₂ nanostructures, it is highly essential to develop a synthesis technique through which we can control these properties. Several attempts have been made to synthesize CeO₂ nanostructures via various chemical routes. F. Zhou et al. has reported the size-control synthesis of CeO₂ crystallites in spherical morphology [128] by employing hydrothermal method while N. Zhang et al. synthesized the rod-like morphology of CeO₂ nanostructures via soft co-precipitation method [129]. Similarly various research groups have reported the variety of synthesis techniques for the preparation of nano CeO₂, for example, thermal evaporation, electro-spinning (ESP), the sol-gel etc. [130-132]. As mentioned previously, bottom-up approaches are very handy over the top-down ones, so we have followed the chemical co-precipitation technique to synthesize CeO₂ nanostructures.

2.2.3 Chemical co-precipitation method

Co-precipitation has an edge over rest of all the bottom-up approaches that it is cost effective, easy to handle, time saving and also it has a very fair control on particle size distribution and other key factors (particle size, morphology etc.). Furthermore, the stoichiometric ratio of the CeO₂ nanostructures can be precisely controlled by optimizing chemical co-precipitation method. This method involves salt precursors (nitrate, sulphate, chloride etc.) which are dissolved in various solvents (distilled water, ethanol etc.). Base agents such as NaOH, NH₄OH and KOH etc. are used to achieve precipitates like oxohydroxides. It is a difficult task to control the size and morphology of the particles in this method. It is often that some surfactants are utilized to get this control. Moreover, optimization of some synthesis parameters like reactant molarity, reaction time, stirring rate, pH value of the reaction are key factors to achieve desired morphology, size control and particle distribution.

A schematic illustration of co-precipitation is given below in the form of a flow chart in Fig. 2.3.

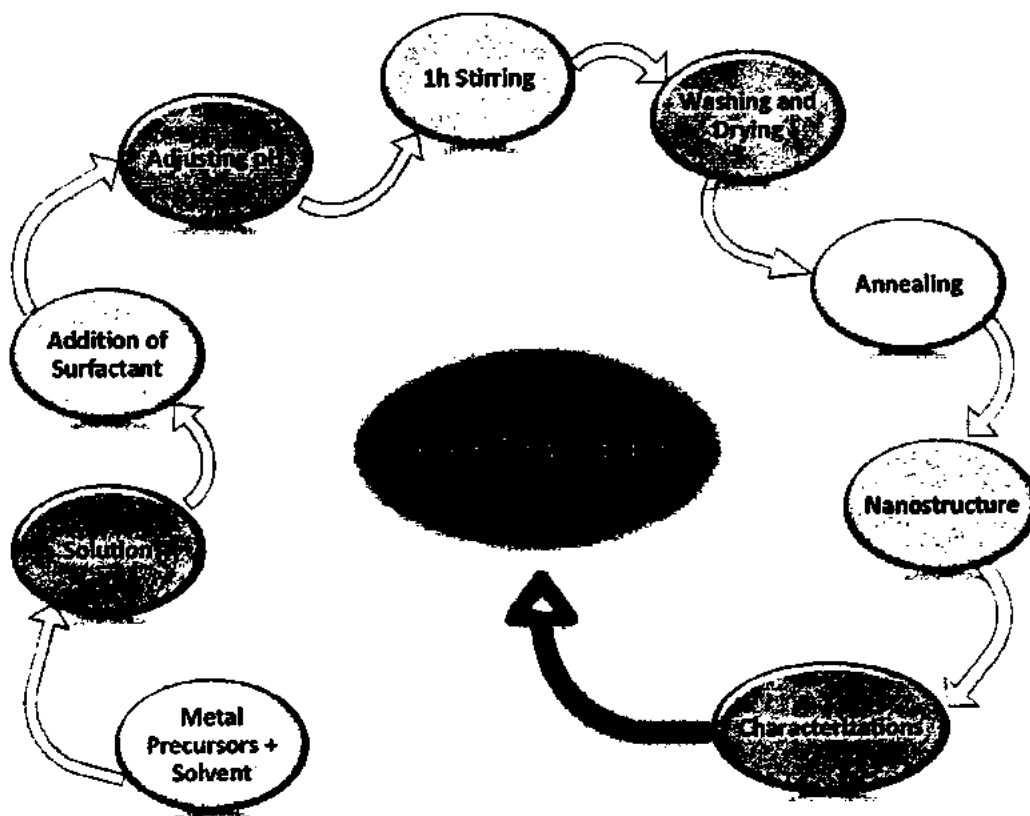


Figure 2.3: A Schematic diagram for the preparation of CeO_2 nanostructures by the chemical co-precipitation method.

In course of synthesis, high crystallinity of prepared samples was achieved by annealing at $300\text{ }^\circ\text{C}$ as un-annealed samples were found to have a lot of impurity phases and poor crystalline nature. The improvement in the crystallinity of the synthesized samples due to annealing effect may be attributed to the fact that at higher temperature, crystallites orient themselves in proper equilibrium sites due to availability of excess free energy in the system. Moreover, the various optimization steps were taken in the synthesis process to obtain the nanostructures with desired phase, morphology and crystallinity.

2.3 Synthesis Parameters Optimization

2.3.1 Reaction temperature

In order to optimize reaction temperature, both the temperature treated (hydrothermal) and un-treated (co-precipitation) chemical preparation roots were utilized. In temperature treated case, two distinct reaction temperatures 50 °C for 30 minutes and 160 °C were maintained for 24hrs, reported in the literature [133, 134]. Fig. 2.4 (a) illustrates that the XRD patterns of both the synthesized CeO₂ samples. It is well clear that the sample treated at 50 °C has no desired phases (cubic fluorite) while sample treated at 110 °C possesses the desired single phase. Thus it is obvious that reaction temperature plays a very crucial role in the growth of CeO₂ nanostructures. No proper crystal structure was developed at the reaction temperature of 50 °C which hints that there is no nucleation and crystal growth at this temperature. The nucleation and crystal growth need some energy which is not provided at this temperature.

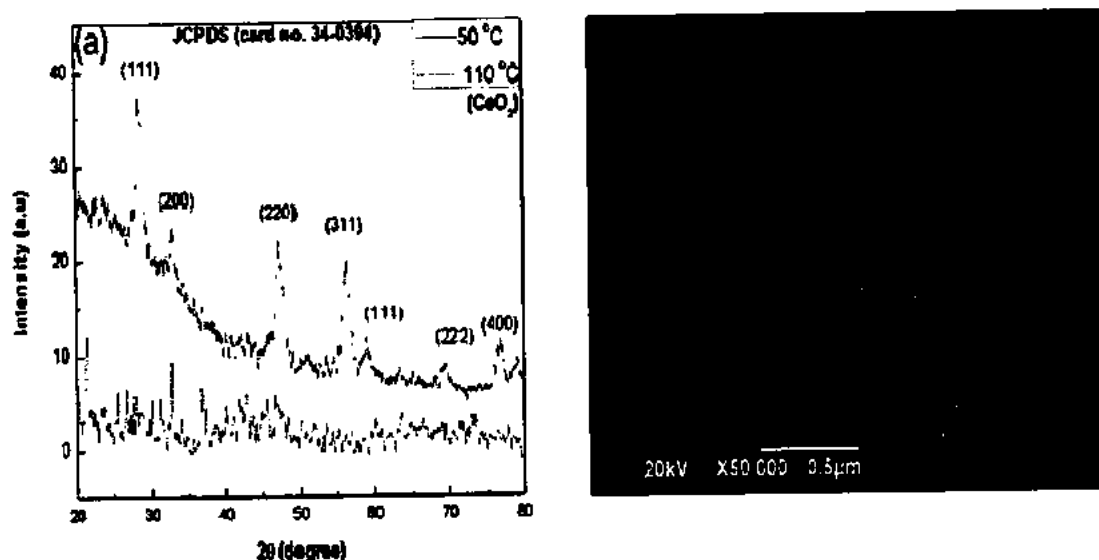


Figure 2.4: (a) XRD patterns CeO₂ prepared at distinct reaction temperatures (b) SEM micrograph of CeO₂ prepared via temperature treated synthesis

Furthermore, the sample treated at temperature 110 °C hydrothermally is found to have well sharp XRD peaks which depict the high crystallinity with no impurity phases. On

the contrary, the SEM micrograph as illustrated in Fig. 2.4 (b), of this sample exhibit poor morphology with no definite shape at nanoscale.

To tune the desired nanostructured morphology an alternative coprecipitation synthesis was carried out at different temperatures. Fig. 2.4 elaborates the XRD patterns on prepared CeO_2 samples at two different temperatures: room temperature and 90°C . It is clear from the XRD patterns that sample prepared at ambient conditions has impurity phases while sample prepared at 90°C contains a single phase, well indexed cubic fluorite structure. The multi-phase morphology of the sample prepared at room temperature may be linked to the fact that the decomposition of metal salts and formation of hydro-oxide complexes were not yet complete under these reaction conditions. Furthermore, the sample prepared at temperature 90°C is found to have well sharp XRD peaks depicting the high crystallinity with no impurity phases. This optimized reaction temperature (90°C) was utilized in the synthesis of all the desired samples of this thesis work.

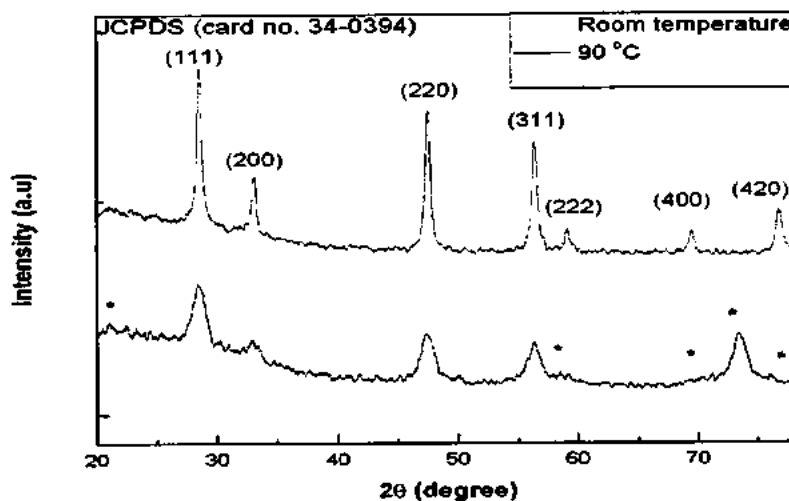


Figure 2.5: XRD patterns CeO_2 prepared at distinct reaction temperatures

2.3.2 Role of pH

The pH of solution is a key factor in the fabrication as well as the in growth yield of various semiconductor metal oxide nanostructures. In the growth mechanism of any metal

oxides, the decomposition and formation of metal ions take place just after the dissolution of metal salts in water. These generated metal ions then react with OH^- ions (formed due to NaOH decomposition) present in the solution to form metal hydroxide complexes. In such chemical synthesis, it is very interesting to notice that, NaOH has been utilized to adjust the pH values of the reaction. Optimization of a proper pH value in a solution defines the suitable quantity of available OH^- ions which is required to accomplish the nucleation of metal ions under super saturated conditions. Thus, keeping in view the importance of a suitable pH value, the pH value is well optimized in all of the performed experiments which is in the range of 10 to 11.

2.3.3 Role of surfactant

It is very important to choose a proper surfactant or capping agent to have a well control over the morphology and particle size of the synthesized CeO_2 nanostructures. In the present work, various surfactants have been tried to tune the desired morphology. The surfactants involve poly-ethylene glycol (PEG), hydrogen peroxide (H_2O_2) and acetic acid (CH_3COOH). All surfactants were used in various concentrations (0M, 0.1M and 0.2M) and better result was optimized for a surfactant concentration of 0.2M. Fig. 2.6(a-c) illustrates the SEM micrographs of the prepared CeO_2 nanostructures via PEG, H_2O_2 and CH_3COOH respectively. It is obvious from Fig. 2.6 (c) that the sample involving CH_3COOH as surfactant has a well-defined morphology comprising homogeneous nanoparticles in the range of 10-20nm. This enhanced and tuned morphology is linked to the fact that at higher surfactant concentration, fast nucleation of CeO_2 take place which in turns result into the formation of smaller nanoparticles. The addition of surfactant controls the particle size by binding the CH_3COO^- ions to the different surfaces of CeO_2 which in turns modify the particle growth rate and orientation. These CH_3COO^- ions are formed by the dissolution of

CH_3COOH in water. Thus, on the basis of this optimization, 0.2M CH_3COOH have been utilized as surfactants in the whole experimental part of this thesis work.

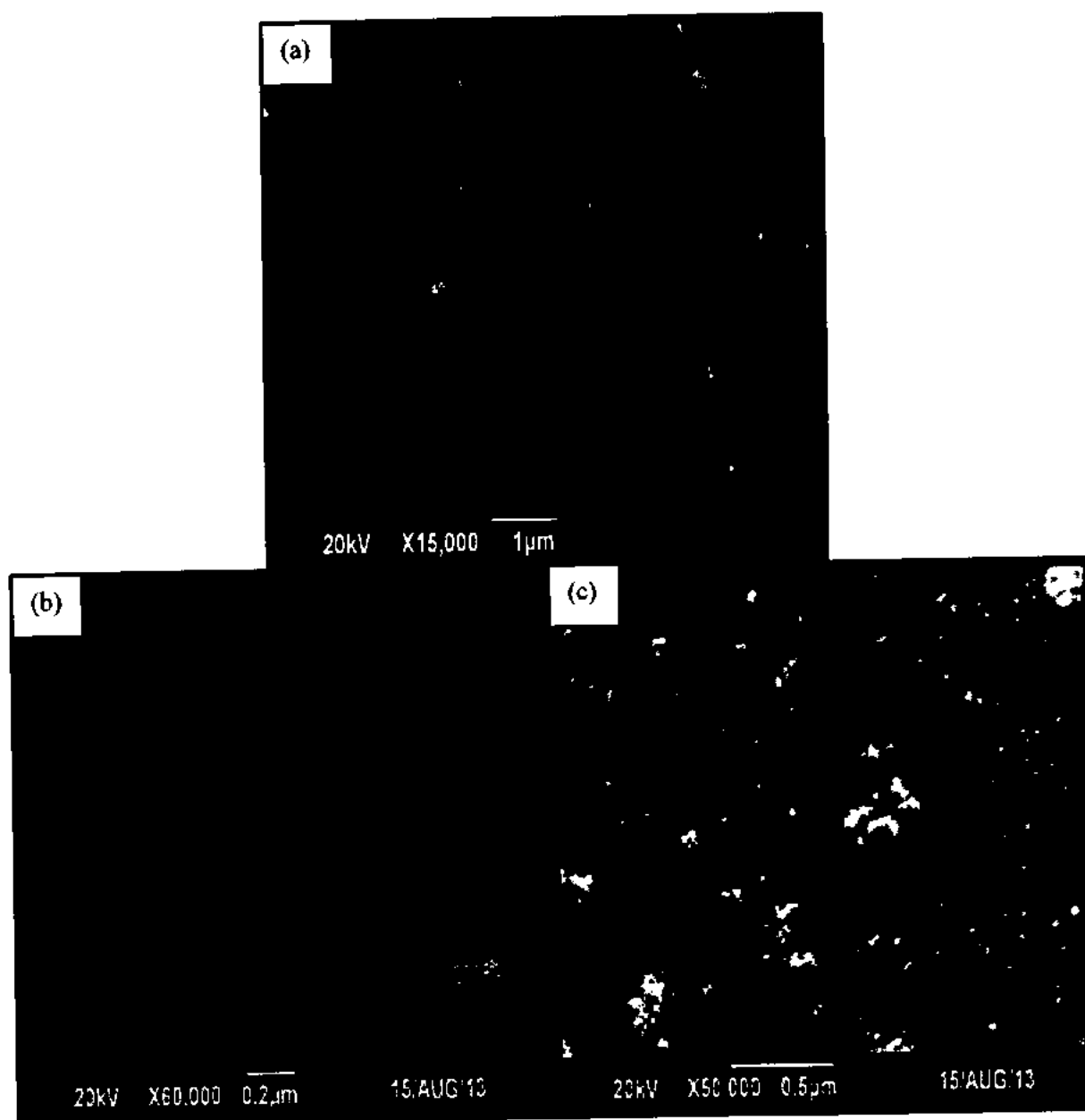


Figure 2.6: SEM micrographs of synthesized CeO_2 prepared using various surfactants

(a) 2% PEG, (b) 2% H_2O_2 , (c) 2% CH_3COOH

2.4 Synthesis Procedures

2.4.1 Synthesis of CeO₂ nanostructures

Chemical co-precipitation method was utilized for the synthesis of bare CeO₂ nanostructures using distilled water as solvent. Chemicals consumed during synthesis were cerium nitrate hexahydrate (Ce(NO₃))₆H₂O, sodium hydroxide (NaOH) and acetic acid (CH₃COOH). First of all, 0.1 M solution of (Ce(NO₃))₆H₂O was prepared in distilled water and was positioned into fume-hood on hot plate (90°C) for 20 minutes magnetic stirring at 500 rpm. Then capping agent (2 mL CH₃COOH) was added to the above solution to control particle size. After that 1 M NaOH basic solution was added drop-by-drop into the above solution until pH value extends up to 10. Now again solution was stirred for 1hr under the same temperature and stirring rate. After cooling, distilled water was again used to wash and collect the precipitates via centrifugation. The drying of washed precipitates was achieved by placing them into an electric oven at 80 °C for overnight. Then dried precipitates were grinded into powder form using mortar and pestle which was further annealed for 2hrs at 300 °C to achieve their improved crystallinity. For doped CeO₂ nanostructures, same chemical co-precipitation procedure was adopted except the addition of different dopant precursors.

2.4.1.1 Synthesis of Co doped CeO₂ nanostructures

Co doped CeO₂ nanostructures were prepared by the above procedure. Different molar concentration of iron chloride-hexahydrate (CoCl₂)₆H₂O was used to synthesize 3%, 5% and 7% Co doped CeO₂ nanostructures i.e. 0.03, 0.05 and 0.07 M solution of (CoCl₂)₆H₂O were added to (Ce(NO₃))₆H₂O solution.

2.4.1.2 Synthesis of Fe doped CeO₂ nanostructures

Fe doped CeO₂ nanostructures were prepared by the above procedure. Different molar concentrations of iron chloride-hexahydrate (FeCl₃)₆H₂O were used to synthesize 3%, 5%

and 7% Fe doped CeO₂ nanostructures i.e. 0.03, 0.05 and 0.07 M solution of (FeCl₃).6H₂O were added to (CeNO₃).6H₂O solution.

2.4.1.3 Synthesis of Ni doped CeO₂ nanostructures

Ni doped CeO₂ nanostructures were prepared by the same procedure. Different molar concentrations of nickel chloride-hexahydrate (NiCl₂).6H₂O were used to synthesize 3%, 5% and 7% Ni doped CeO₂ nanostructures i.e. 0.03, 0.05 and 0.07 M solution of (NiCl₂).6H₂O were added to (CeNO₃).6H₂O solution.

2.4.1.4 Synthesis of Mn doped CeO₂ nanostructures

Mn doped CeO₂ nanostructures were prepared by the above procedure. Different molar concentrations of manganese chloride tetrahydrate (MnCl₂).4H₂O were used to synthesize 3%, 5% and 7% Ni doped CeO₂ nanostructures i.e. 0.03, 0.05 and 0.07 M solution of (MnCl₂).4H₂O were added to (CeNO₃).6H₂O solution.

2.5 Cell Culture, Anticancer Activity and Cytotoxicity of CeO₂

Nanostructures

Human cancer cell line SH-SY5Y (ATCC CRL-2266) and human normal cell line HEK-293 (ATCC CRL-1573) were purchased from American Type Culture Collection (Manassas, VA, USA). Both kind of cells were kept in Dulbecco's Modified Eagle's Medium (DMEM) (Sigma Aldrich) supplemented with 10% fetal bovine serum (FBS) and grown at 37°C in a humidified incubator (CO27, Newburns wick, Scientific Co.) supplemented with 5% CO₂. 96-well plates (Corning Incorporated, USA) were seeded by 1×10⁴ cells/well and allowed to attach to the surface for 24 hours prior to treatment. Sonication of nanoparticles was carried out for 30 min at 40W to avoid nanoparticles agglomeration prior to the cell exposure. Both types of cells were treated with the suspension of undoped and Co doped CeO₂ nanoparticles (20 mg/ml). Each performed experiment involved sample control, media

control and untreated cells as negative controls. CCK-8 analysis was utilized for Cell viability measurements.

Intra-cellular reactive oxygen species (ROS) study was performed by 2', 7'-dichlorodihydrofluorescein diacetate (H2DC-FDA: 25mM) assay, flow cytometry, using a fluorescence microscope (Hitachi, Tokyo, Japan). In flow cytometry, the level of produced oxidative stress was examined with the help of dichloro-dihydro-flourescein diacetate (DCFH-DA) assay. The diffusion of this assay in each cell line gives the value of ROS produced. This (DCFH-DA) assay can easily be oxidatively tuned into a fluorescent derivative because it is highly sensitive to ROS variation especially in an atmosphere containing the different factors like hydrogen peroxide, superoxide anion with other cofactors. The cells treated with nanoparticles for 24 hours were washed with PBS and incubated with DCFDA dye (20 μ M) for 30 minutes at 37 °C in dark. The ROS generation was studied via flow cytometry

2.6 Characterization Techniques

The synthesized samples were characterized by powder X-rays diffraction (XRD), which can provide the structural information of the sample such as lattice constants, cell volume, X-ray density, crystallite size, phase transformation temperature, particle size and composition of the samples. Morphological analysis is done using SEM while vibrational properties and structural defects (V_o) were examined by Raman spectroscopy. SSA of the synthesized samples was analyzed by BET analysis. Electrical resistivity measurement, ϵ' and ϵ'' give informations about the conduction mechanism. Hysteresis loops provide informations about the M_s , coercivity (H_c) and remanance (M_r). The instruments used for characterization are described as follows.

2.6.1 X-ray diffraction (XRD)

X-rays are electromagnetic radiations with wavelength in the range of angstrom (\AA) and are capable to interact with electronic cloud of the atoms in the crystal. As their

wavelength is comparable to the inter-atomic spacing in the crystals so they fulfill the necessary condition of the diffraction. XRD is the most suitable, powerful, general and nondestructive technique for examining the various crystals structure as no elaborate sample preparation is required [135]. Using this technique, one can detail the information on impurity phases, structures and texture (preferred crystal orientations) of the crystals. Moreover, structural parameters like crystal defects, crystallinity and average grain size can also be estimated using this versatile technique. In XRD, Sample is exposed to X -rays of known wavelength (λ) and due to their interaction with electrons present in the atoms on each crystal plane elastic scattering occurs (Fig. 2.7). Those scattered X-rays which fulfill the Bragg's condition (Eq. 2.1) interfere constructively and give rise to a signal which is identified by the detector part of the XRD setup.

$$2d\sin\theta = n\lambda \quad (2.1)$$

Where n is an integer, λ being the wavelength of the incident beam, θ the angle of incidence and d is the diffracting planes spacing. These constructively interfered X-rays results into distinct diffraction peaks located at specific angles. The pattern of these diffraction peaks at a given angle (2θ) is the characteristics feature of every material which distinguishes it from other materials. Furthermore, crystallinity quality, crystallite sizes and crystal structure can be found from these diffraction patterns using crystallography. A sample with high crystallinity possesses consistent d -spacing and sharp narrow peaks with higher intensity and vice versa. While amorphous materials (atoms arranged in random fashion) fail to expose detectable signals so no diffraction peaks are achieved. We have examined the XRD patterns of all the synthesized bared as well as doped CeO_2 nanostructures in powder form using PANalytical X-ray diffractometer, Model: 3040/60 X'Pert PRO made in Netherland, with radiations $\text{CuK}\alpha$

X-rays having wavelength of 1.54 Å. In this course of study, XRD was performed in the range of 20° - 80° (2θ) with step size 0.2° (2θ).

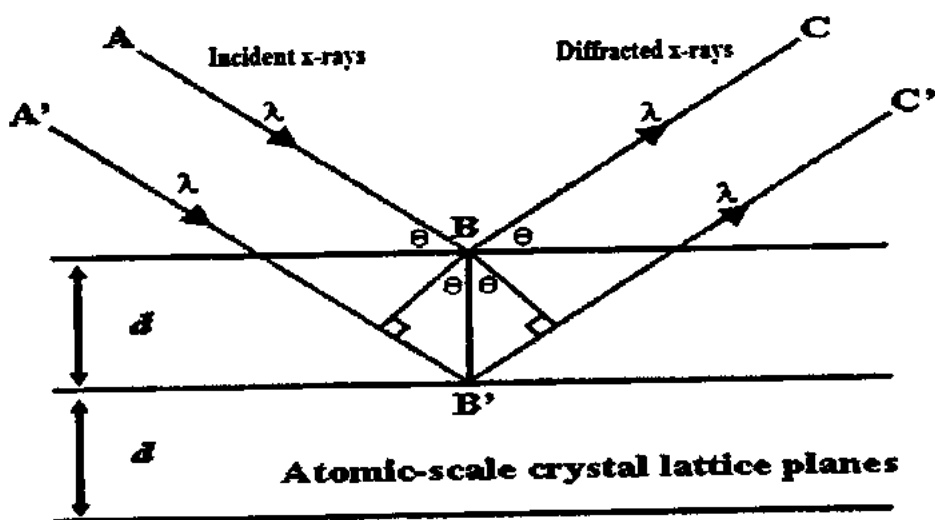


Figure 2.7: Diffraction of X-rays from a crystal [136].

2.6.2 Scanning electron microscopy (SEM)

SEM is a highly vital tool to investigate the surface structure of the nanostructures. It can be utilized to produce three dimensional images of the specimen surfaces from which we can examine the diameter, thickness, length, orientation, density and shape of the nanostructures. SEM utilizes a high energy focused electron beam with extremely short wavelength to produce much higher resolution images as compared to that of conventional microscope. An electron gun is used to produce a beam of electrons which is focused on the specimen placed in the vacuum conditions using electromagnetic lenses. Interaction of this electron beam with the sample results into the generation of various types of signals including X-rays, secondary electrons (SE), light, auger electrons and backscattered electrons. The intensity of all of the generated signals is picked by the mounted detectors. The observed electronic intensity is converted into light intensity which results in the formation of visual image that can be seen digitally. SE generated near the sample surface usually possess low energy ($<50\text{eV}$) and are responsible to produce images with best quality and high resolution

[137]. Moreover, conducting coating of gold, silver etc. is used for non-conducting samples to avoid from surface charging. In the present study, we marked dimensions of few nanoparticles in the SEM micrograph and then find their mean to obtain average particle size. In this thesis work, surface morphologies of the synthesized samples were examined using SEM (JEOL, SEM, Model JSM6490LA).

2.6.3 Raman spectroscopy

Raman spectroscopy is a versatile, efficient and non-destructive technique which is utilized to investigate the structural defect, microstructures as well as the chemical information of the sample. Moreover, this technique is very vital and sensitive to detect the presence of minor impurity phases which even couldn't be noticed by XRD. The theoretical origin of this technique roots to an Indian Physicist Prof. C.V. Raman as this spectroscopy utilizes the Raman scattering in its action. In this spectroscopy, the interaction between polarizability ellipsoid of a vibrating molecule and light induced oscillating dipole is responsible for the origin of Raman bands that is; when sample is exposed to a beam of monochromatic light, scattering of light occurs due to its interaction with electric dipole of molecules in the samples. This scattering results into the excitation of molecules to the higher vibrational energy levels. The light may suffer one of the following scattering phenomena:

- **Raleigh scattering:** scattered light owing the same frequency as that of incident one,
- **Stokes scattering:** scattered light owing the lower frequency than the incident light,
- **Anti-Stokes scattering:** scattered light owing the greater frequency than the incident light.

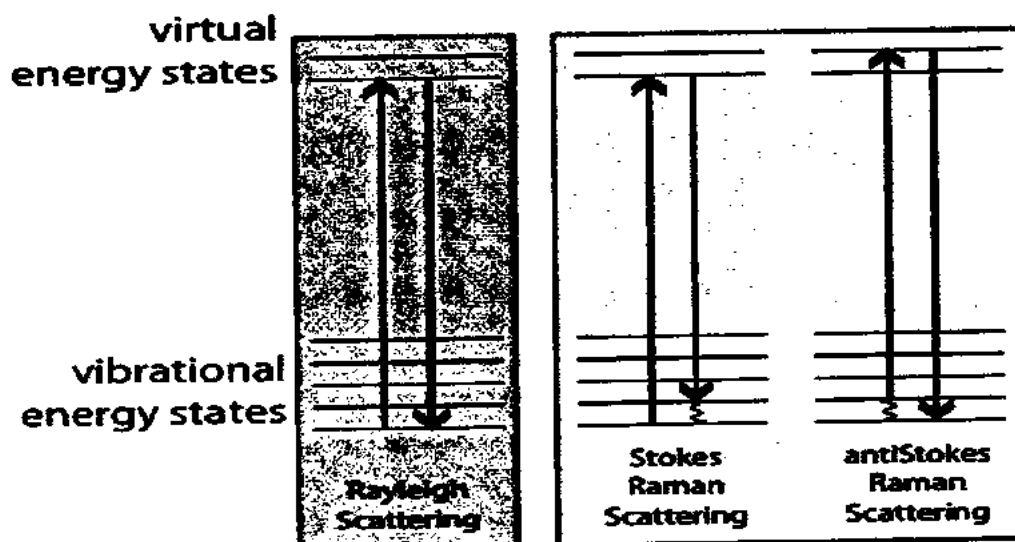


Figure 2.8: An illustration of various types of Scattering related to Raman spectroscopy

[138]

Raman spectroscopy is concerned with Stokes scattering and resulting slight shift in frequency is called Raman shift. This Raman shift is the characteristics feature of the molecule that corresponds to “finger-print” properties like vibrational or phonon frequencies, structural defects and chemical information of the sample. In present work, this spectroscopy is utilized to study the crystal defects (V_o) as well the vibrational mode of the synthesized samples as a plot between normalized intensity of incident light and Raman shift.

2.6.4 Ultra violet visible (UV-Vis) spectrometry

UV-Vis is a fascinating and non-destructive technique which is most commonly used to investigate the optical properties of the various nanomaterials in terms of its band gap (E_g). It involves the absorption, transmission and reflectance of electromagnetic radiations, in UV as well as in visible region (200nm – 800nm), from the material under investigation. This irradiation of electromagnetic radiations results into electronic transition inside the sample. In this case absorbed or transmitted light is the characteristics of its chemical structure. The absorbed light in this phenomenon follows the following relation:

$$A = \log_{10} \left(\frac{I_0}{I} \right) = \epsilon(\lambda)CL \quad (2.2)$$

Where I_0 and I are the intensities of incident and absorbed light, A is the absorbance, L (cm) stands for cell path length, C is the solution concentration (moles/Ltr.) and ϵ is for the molar absorptivity (liter/mole/cm). The spectrum of UV-Vis plot is obtained by a graphical representation of transmitted or absorbed light by the sample as a function of wavelength.

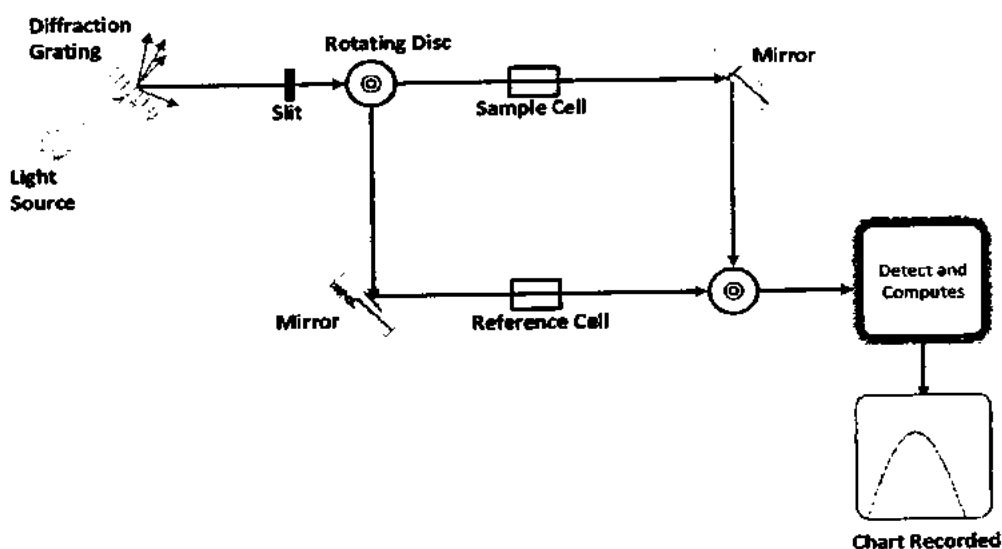


Figure 2.9: Principle of UV-VIS Spectroscopy.

In the present work, UV-Vis spectroscopy, PerkinElmer Lambda 200 UV/VIS/NIR absorption spectrometer, is utilized by taking the solution (1mg/ml) of the synthesized nanostructures in distilled water. The absorption from the distilled water effects are subtracted from the final results. The schematic illustration of UV-Vis set up is shown in Fig. 2.10.

2.6.5 Vibrating sample magnetometer (VSM)

VSM is the most popular scientific technique invented by Simon Foner in 1955 and is used to investigate the magnetic properties of the various magnetic materials. VSM is capable to take measurements for a sample in various forms like powder, solids, thin film etc. Moreover, this

technique has also a distinction due to its high accuracy, capability to study magnetic moment as a function of magnetic field, temperature, angle and time. Most of the VSM has the facility to perform its measurements over a wide range of temperature exploring new era of research. In VSM measurements, sample is placed in a sensing coil and is made to oscillate sinusoidally by using piezoelectric oscillating material in the presence of a uniform magnetic field. The resulted changing magnetic flux will result into an induced emf in the coil which is proportional to the magnetic moment of the sample. This signal is then collected by the locking amplifier built-in the instrument and finally transmitted into computer setup (software) which gives the hysteresis loop of the magnetic samples. Interpretation of the hysteresis loop gives the detail information about the magnetic properties like: M_r , M_s , H_c etc. of the material. A schematic illustration of the VSM setup is shown in the Fig. 2.11

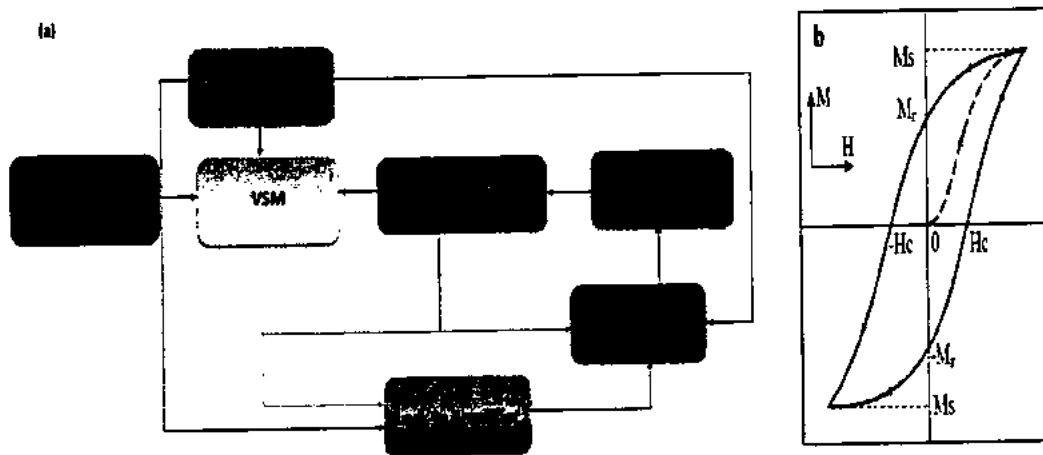


Figure 2.10: (a) A general setup of VSM, (b) a hysteresis loop [139].

2.6.6 Brunauer-Emmet and Teller (BET) SSA analyzer

Brunauer-Emmet and Teller (BET) analysis is a most common and versatile technique used for the precise calculation of SSA of various nanomaterials [140]. BET analysis involves adsorption of multi-layer nitrogen (N_2) usually measured as a function of relative pressure with the help of an analyzer which is fully automated. This analysis encompasses

pore area and external area evaluation to find the total SSA in the units of m²/g which in turns gives the detail information about the surface porosity and particle size effects in numerous practical applications.

In order to find SSA, prior to the analysis, de-gassing of the sample is achieved by heating it upon a certain temperature (300 °C) in vacuum conditions for overnight to get rid of the moisture trapped inside the pores of a given material. Then the sample is dosed in well controlled increments by some adsorptive, usually N₂, under the cryogenic temperature conditions (77K). The pressure of the gas is made to equilibrate after each adsorptive dose and quantity of adsorbed gas is determined. In case of mono-layer adsorption, adsorbed quantity at each pressure defines an adsorption isotherm which provides the quantity of adsorbed gas required in mono-layer adsorption over the surface of sample. By knowing the area covered by each a molecule of adsorbed gas; SSA can be determined by multipoint BET method. The following BET adsorption isotherm equation is used to find the precise value of SSA.

$$\frac{1}{w\left(\frac{P}{P_0}-1\right)} = \left[\frac{1}{W_m C} + \frac{C-1}{W_m C \left(\frac{P}{P_0}\right)} \right] \quad (2.3)$$

For the solution of BET equation a liner plot of 1/[W (P/P₀)-1] against P/P₀ is required.

Where P/P₀ is relative pressure, w is the volume of adsorbed gas at STP, W_m being volume of adsorbed gas to form monolayer at STP and C is BET constant. Also W_m is given by

$$W_m = \frac{1}{s + i} \quad (2.4)$$

Here, s is the slope and i stands for y-intercept of BET plot. Total surface area(S_t) is,

$$S_t = \frac{W_m N A_{cs}}{M} \quad (2.6)$$

Here, A_{cs} is the cross-sectional area of N₂ molecule. SSA is then calculated by dividing S_t by weight of the sample,

$$SSA = \frac{S_t}{w} \quad (2.7)$$

2.6.7 Electrical measurements using LCR meter

The inductance, capacitance and resistance (LCR) meter is versatile instrument which provides accurate, economical and rapid testing of various materials up to multi-frequencies ranges. LCR meter is capable of automatic measurements of inductance (L), resistance (R), capacitance (C), impedance, quality factor, AC resistance, conductance and also dissipation factor. Furthermore, ϵ' as well as dielectric loss measurements are made from L,C and R data.

A typical LCR meter consists of a regulated power supply (S), owing wide range of amplitude and frequency to provide ac voltage to the sample shown in Fig. 2.11. When a variable voltage (using rheostat) is applied to the given sample, current is set up which flows to the pair of operational amplifiers (A and A') whose output is a signal which is proportional to the current I_R . A four wire Kelvin connection is used separately from which two wires carry test current and two wires detect the voltage across the sample. These voltage and current signals are multiplied with two reference signals one in phase with power supply signal and other with a phase contrast of 90° to obtained real and imaginary parts of the required IV data. Finally, these signals are fed to the microprocessor (M) which gives the proper conversion of these signals into required data points.

To investigate the electrical properties of synthesized nanostructures, LCR meter (Wayne Kerr 6500 B Impedance analyzer) was utilized. For this purpose, pellets of 8.0 mm diameter and 2.0 mm thickness for all the synthesized nanostructures were made with the help of hydraulic presser. Then sintering of these pellets was carried out in an electric oven at about 180°C for 3 hours. The electrical contacts to the circular faces of the synthesized pellets were made by silver paste coating on their both sides. All the AC measurements were carried out at ambient conditions and in the frequency range of 1 KHz to 5MHz. ϵ' was calculated using the relation,

$$\epsilon' = \frac{C \times d}{A \times \epsilon_0} \quad (2.4)$$

Where C is for the capacitance (farad) of the pellet, d being the pellet thickness (meter), A the cross-sectional area of the flat circular surface of the pellet (m^2) while ϵ_0 is the permittivity of free space. The ϵ'' was obtained by multiplying ϵ' with the dissipation factor (D) found experimentally. At the end, the AC conductivity (σ_{ac}) was calculated from the equation

$$\sigma_{ac} = 2\pi\epsilon_0\epsilon' \tan \delta \quad (2.5)$$

$$\text{Where, } \tan \delta = \frac{\epsilon''}{\epsilon'}$$

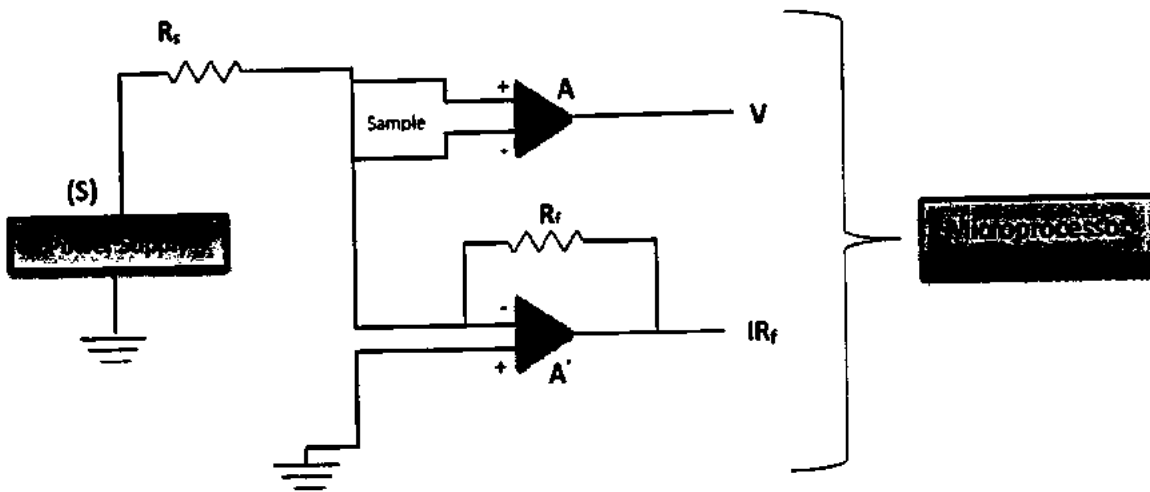


Figure 2.11: Schematic diagram of LCR meter.

Chapter No.3

Synthesis, Characterization and Anticancer Study of Co Doped CeO₂ Nanoparticles

3.1 Introduction

Being the highly abundant material, CeO₂ is technologically very vital owing to its larger sphere of applications, for instance in catalysts [141], oxygen sensors [142], solid oxide fuel cells (SOFC) [143], thin films of electro-chromic stuff [144], optical polishing agents [145], luminescence [28], UV adsorbents [29] and humidity sensors [30]. Moreover, it is also very fascinating material for its versatile solicitations in the domain of spintronics, optoelectronics and magnetic data storage devices because of its partially 4f filled electronic structure [23]. CeO₂ based dilute magnetic semiconductors (DMSs) have attracted huge amount of interest recently due to their similar structural parameters to that of well-established Si material. Owing to these characteristic, CeO₂ based DMSs can be easily integrated on Si based electronic devices [146].

However, the DMSs have huge potential in electronic industry only if they exhibit RTFM. In this regard, a lot of endeavors have been done in TM-doped CeO₂ nanomaterials [147-150] as well as in thin films [151-154]. It is mostly seen that a fraction of Ce ions exist in the Ce³⁺ form in CeO₂ and this reduction in positive charge is compensated by a corresponding number of V_o. Owing to large surface area to volume ratio at nanoscale, CeO₂ nanomaterials have a unique electronic structure with novel characteristics as compared with its bulk counterpart. The modification in shape and particle size results in the formation of surface defects such as V_o, which endows it with the ability to exist in either Ce³⁺ or Ce⁴⁺ state on the particle surface [28]. These V_o are considered to be a possible origin to enhance ferromagnetism in CeO₂ nanomaterials [153, 154]. The cation Ce in mixed state of Ce³⁺/Ce⁴⁺ redox reactions are also responsible for the outstanding biological properties of CeO₂

nanostructures [155]. In addition, the dopant with different ionic states in CeO₂ host matrix can generate more structural defects in order to gain charge neutrality [156] which leads to enhance physical and biocompatibility of it. The transition metal Co is thought to be an excellent dopant for CeO₂ because of its different ionic states and good activator of ferromagnetic behavior [157]. It can also induce large number of V_o defects in CeO₂ matrix, which are crucial for both magnetic and anticancer applications of CeO₂. There are very few reports available on the anticancer activity of Co doped CeO₂ nanoparticles to date. Therefore, undoped and Co doped CeO₂ nanoparticles have been prepared via cost effective and simple chemical route. The Co doping driven effects on the structural, morphological, surface area, optical, magnetic, dielectric and anticancer properties of the CeO₂ nanoparticles have been studied in detail.

3.2 Results and Discussion

3.2.1 Structural and morphological investigations

Fig. 1 shows XRD patterns of the synthesized undoped and Co doped CeO₂ samples. It is manifested that all the prepared samples demonstrate single phase cubic fluorite structure and no additional peak related to cobalt or any other impurities are identified in these samples. All diffraction peaks can be well indexed to the pure cubic fluorite-type structure of CeO₂ according to JCPDS (card no. 34-0394). It can be clearly seen from Fig. 3.1(a) that with the increase in Co concentration, the intensities of all diffraction peaks and full width at half maximum (FWHM) in XRD patterns increases which is attributed to the difference in ionic radii of Co²⁺ (0.72 Å) and host cation Ce⁴⁺ (0.92 Å) ions. This change in radii also influenced the crystalline growth of CeO₂ with the increase of dopant concentration [86]. It is also found that the main peaks have a slight shift towards the higher angle as shown in the Fig. 3.1 (b) which confirms the successful doping of Co into the host lattice [158].

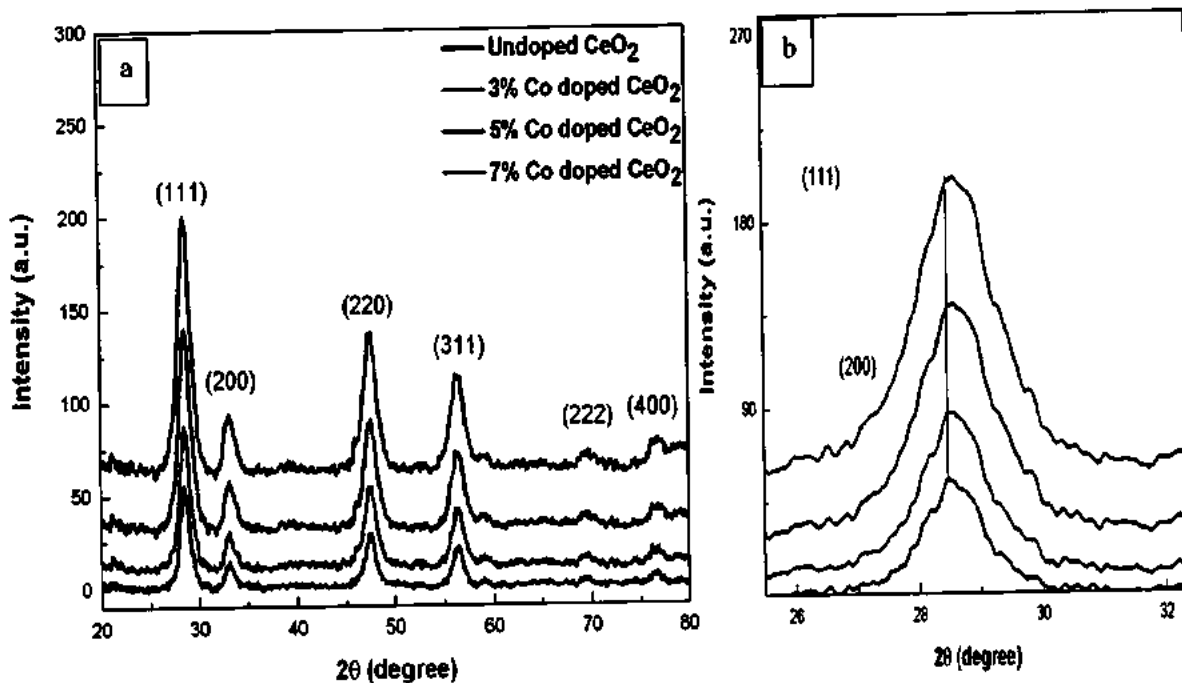


Figure 3.1: a) XRD patterns of the prepared samples and b) Co loading induced shift in the (111) plane

In order to calculate the crystallite size of all the synthesized samples, Scherer's formula is employed at major planer peak of reflection. The approximate average crystallite size for undoped CeO₂ is found to be 8 nm, which is observed to decrease down to 4.5 nm with the increase in Co doping level. This change in crystallite size can be due to the difference in Pauling electro-negativities of dopant (1.88) and host cation ions (1.12) during the growth process of crystal. Furthermore, the lattice constants have been calculated using the following relation:

$$a = b = c = \frac{d}{\sqrt{h^2 + k^2 + l^2}} \quad (3.1)$$

where $a = b = c$ are lattice constants, d represents inter planer spacing and h, k and l are Miller indices. It is found that the lattice parameter of the undoped nanocrystalline CeO₂ is 5.427 Å, which is higher than that of its bulk one (5.4113 Å). The evolution in lattice parameter of nanoparticles might be due to the increase in the V_o defects [20]. The lattice constant value of CeO₂ is observed to decrease upon Co doping as listed in Table 3.1. This

decrease may be attributed to the lattice contraction due to the substitution of smaller sized Co^{2+} ions on the sites of larger size Ce^{4+} ions [159].

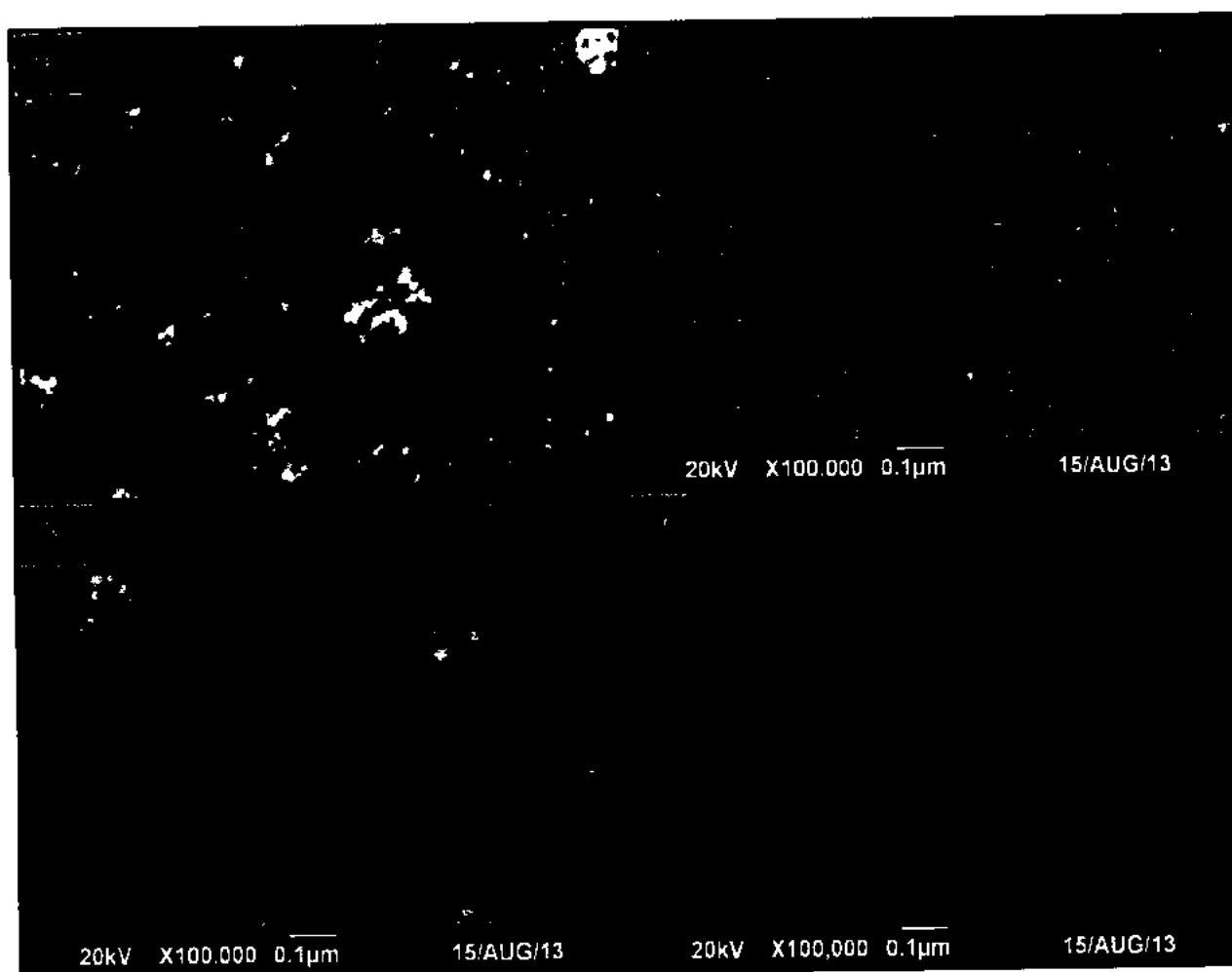


Figure 3.2: SEM images of $\text{Ce}_{1-x}\text{Co}_x\text{O}_2$ nanoparticles. (a) undoped CeO_2 , (b) 3% Co doped CeO_2 , (c) 5% Co doped CeO_2 , (d) 7% Co doped CeO_2

Fig. 3.2 depicts the SEM images of undoped and Co doped CeO_2 samples which clearly reveal that all the prepared samples have zero dimensional (0-D) nanostructures morphology. It is very obvious from all micrographs that the nanoparticles are highly homogenous and symmetrical in size with spherical shape. The difference in valence states, ionic radii and Pauling electro-negativities of Co and Ce cations have influenced the particle size of prepared nanoparticles (8-20 nm) as observed in Fig. 3.2.

3.2.2 Analysis of surface area

Fig. 3.3 shows the plot of surface area as a function of Co dopant concentration in CeO₂ host matrix. Quantitative calculations from this graph depict an interesting finding that the Co doping has significantly enhanced the Brunauer-Emmett-Teller Specific Surface Areas (BETSSA) from 234 to 344 m²g⁻¹ of CeO₂ nanoparticles. This high BETSSA as result of Co doping further clearly confirms the decrease in particle size as observed in the above structural and morphological investigations. Previously in the literature, a SSA of 152 m²g⁻¹ has been reported using Pr as dopant in CeO₂ matrix [160]. N. Sabari Arul et al. have also enhanced the BETSSA from 52 m²g⁻¹ to 132 m²g⁻¹ by doping different concentrations of Co into CeO₂ nanorods prepared via co-precipitation method [159]. Y. Song et al., have achieved BETSSA of 83 m²g⁻¹ for CeO₂ nanoparticles fabricated by facile surfactant-assisted solvothermal route [161]. The observed high value of BETSSA up to 344 m²g⁻¹ in the Co doped CeO₂ nanoparticles as compared to the previously reported values makes them potential in different applications from electronics to nano-medicines.

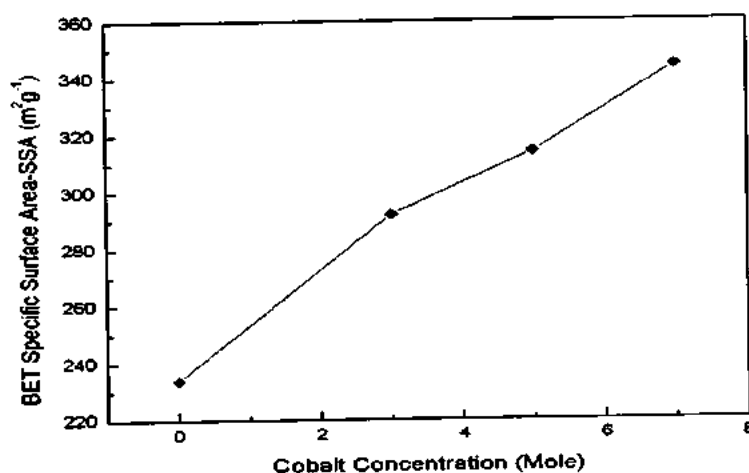


Figure 3.3: BET-SSA Analysis of Ce_{1-x}Co_xO₂ nanoparticles

3.2.3 Raman and optical characterizations

Fig. 3.4 depicts the Raman spectra of the synthesized nanoparticles. Raman spectra of undoped CeO_2 nanoparticles exhibit a prominent peak at 445 cm^{-1} , which has huge shift from the characteristic Raman active mode known as F_{2g} mode for bulk CeO_2 (465 cm^{-1}) [73]. This peak shift is often associated with V_o and phonon confinement effects due to the small particle size [71]. Furthermore, it can also be seen from Fig.3.4 that the Co doping has significantly suppressed the peak intensity of F_{2g} Raman active mode and systematically broadened the width of this mode peak. These variations (such as shift toward lower frequency, decrease in peak intensity and broadening in width of the F_{2g} mode peak) observed in characteristic peak of CeO_2 Raman spectra confirm the formation of its crystal structure with plenty of V_o defects [73]. The presence of V_o in these nanostructures may be due to the enhancement of BETSSA of prepared nanostructures as observed in XRD, SEM and BET results. These defects (V_o) may play important role to tune the physical characteristics (M_s and E_g) of these synthesized nanoparticles.

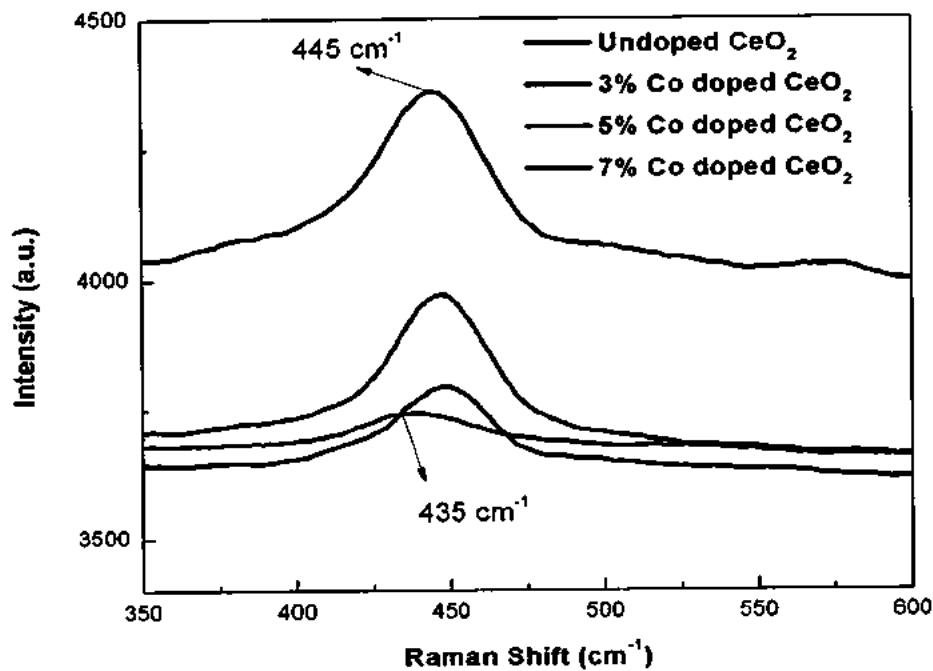


Figure 3.4: Raman spectra of the prepared nanoparticles

The optical properties of the synthesized undoped and Co doped CeO₂ nanoparticles have been examined by UV-visible spectrophotometer. Fig. 3.5(a) illustrates the UV-visible absorption spectra of the undoped and Co doped CeO₂ nanoparticles which demonstrate the presence of prominent absorption peak at 312 nm for all samples. The positions of the absorption peaks of undoped and Co doped CeO₂ nanoparticles confirm that they possess fluorite cubic structure [162]. The approximate bandgap of the synthesized nanoparticles is calculated using the relation for direct bandgap:

$$(\alpha hv)^2 = A (hv - E_g) \quad (3.2)$$

where α is the optical absorption coefficient, hv is the photon energy, E_g is the direct bandgap energy and A is a constant [163]. The plot of $(\alpha hv)^2$ versus energy has been drawn and shown in Fig. 3.5 (b). The band gap energies have been obtained by extrapolating the straight part of the curve to energy axis. The estimated energies values of direct band gap of undoped and Co doped CeO₂ nanoparticles are marked in Fig. 3.5(b). It has been observed that bandgap (E_g) of Co doped CeO₂ nanoparticles have significant red shifts (0.01 eV, 0.29 eV and 0.34 eV for Co_{0.03}Ce_{0.97}O₂, Co_{0.05}Ce_{0.95}O₂ and Co_{0.07}Ce_{0.93}O₂ respectively) as compared to the undoped CeO₂ nanoparticles ($E_g = 3.19\text{eV}$). This shift is higher than the reported values of red shifts [164]. In order to preserve the charge neutrality after substitution of divalent or trivalent Co ions for Ce ions in CeO₂ matrix, V_o are produced at the interface between the grains of Co doped CeO₂ nanoparticles [164]. These V_o significantly tuned the electronic structure of CeO₂ by introducing a red shift in the absorption band edge via hybridization of Ce 4f, Co 3d and O 2p orbitals [115]. Similar results are also reported for some other metal oxides [165].

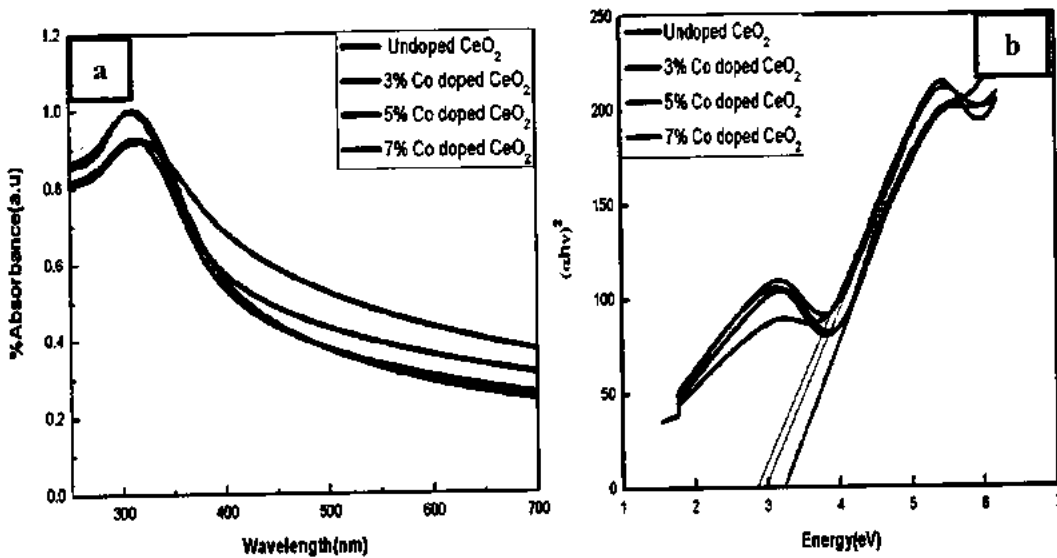


Figure 3.5: (a): UV-Vis absorption spectra of the CeO₂ nanoparticles (b): Plots of $(\alpha h\nu)^2$ as a function of photon energy E for the synthesized nanoparticles

3.2.4 Dielectric properties

In order to investigate dielectric properties of the prepared nanoparticles, the undoped and Co doped CeO₂ nanoparticles have been pressed into circular pellets of 8 mm diameter and 1.2 mm thickness. ϵ' , ϵ'' and σ_{AC} have been measured with different AC frequency range using the formulae in listed in equations 2.4 and 2.5.

Fig. 3.6 (a) shows the plot of ϵ' as a function of AC frequency in the range of 3 KHz- 5 MHz at room temperature. This graph indicates the decrease in ϵ' with the increase in AC frequency up to 2 MHz and then has a constant trend. Maxwell-Wagner has explained such behavior in his model by suggesting that charge carriers can easily tunnel into the grains. These carriers accumulate at the grain boundaries under the influence of external field which leads to a large polarization owing to high ϵ' at low frequency [166]. Furthermore, it is also found from Fig. 3.6 (a) that ϵ' increases with Co doping level. This increase in ϵ' with Co doping may be due to the higher dielectric polarization as compared to that in undoped CeO₂ [167].

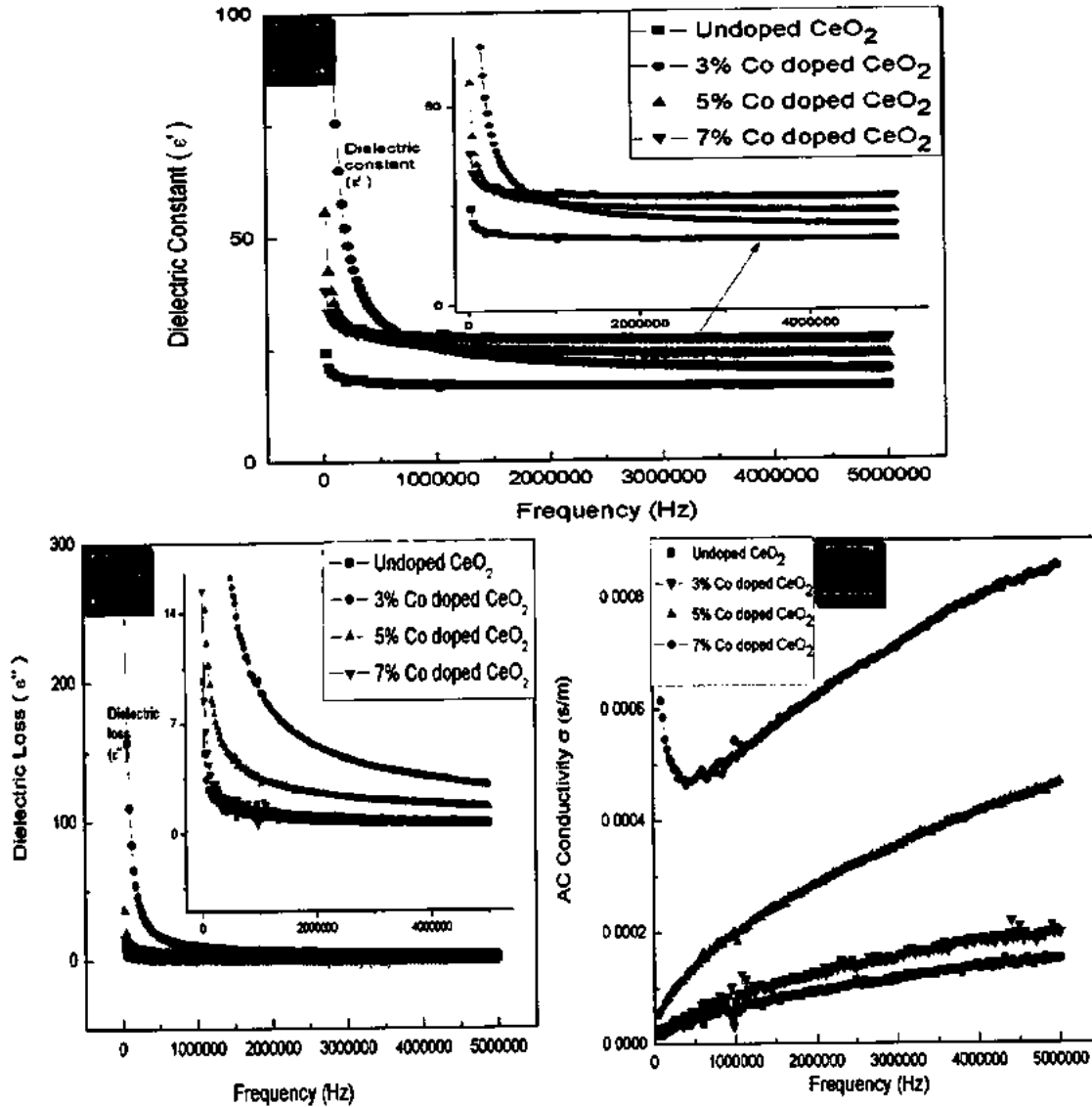


Figure 3.6: (a): Dielectric Constant (ϵ'), (b): Dielectric Loss (ϵ''), (c): AC conductivity (δ_{AC}) variations as a function of AC frequency

Fig. 3.6 (b) shows the variation of ϵ'' as a function of frequency in the range of 3 KHz- 5 MHz. It is observed that there is a decrease in ϵ'' with the increasing AC frequency for all the synthesized nanoparticles. This decrease in ϵ'' as a function of AC frequency can be understood on the basis of high resistivity at grain boundaries as explained by Koop's model [168]. The exchange of electrons at these grain boundaries requires extra energy; as a result ϵ'' is higher at lower frequency. However, at higher frequency, the resistivity is comparatively lesser so grains themselves are thought to play a dominant role. It can be also observed from Fig. 3.6 (b) that value of ϵ'' also increases with Co doping into CeO₂ matrix. This decrease in

ϵ'' can be due to the requirement of more energy for the exchange of electrons between Ce ions and Co ions [167].

Fig. 3.6 (c) demonstrates the plot of σ_{AC} as a function of frequency for undoped and Co doped CeO₂ nanoparticles. It is interestingly observed that σ_{AC} of CeO₂ is significantly increased with Co doping. This increase in σ_{AC} of CeO₂ with Co content can be due to the presence of V_o as observed in Raman results. These V_o leads to more free charge carriers in the system [167].

3.2.5 Magnetic study

Fig. 3.7 displays M-H curves of undoped and Co doped nanoparticles carried out at room temperature. It is remarkably observed that the prepared nanoparticles exhibit RTFM. The saturated magnetization (M_s), coercive field (H_c) and magnetic remanence (M_r) for all the samples are carefully calculated and are listed in Table 6.1. It is found from M-H loops that the Co doping in the host matrix has enhanced M_s , while decreased the H_c and M_r values of CeO₂ nanoparticles. The most interesting feature is that undoped CeO₂ nanoparticles exhibited RTFM with M_s value 0.0083 emug⁻¹ that is greater than the previously reported M_s and H_c values for undoped CeO₂ [17, 169]. Several other research groups have also reported the RTFM behavior of CeO₂ [114, 170,171]. The exact origin of RTFM in REMO is yet not completely clear. However, the interactions between electron spin moments resulting from the V_o at the particle surface are believed to be responsible for the FM in CeO₂ nanostructures.

The observed RTFM for Co doped CeO₂ nanoparticles in this case may be explained on the basis of F-center exchange (FCE) coupling that involves both V_o and transition metal (TM) as reported by many research groups [88,153]. In FCE mechanism, a F-center is formed when an electron is trapped in V_o. The V_o constitutes groups with two Co ions i.e., Co-V_o-Co. Moreover, an electron trapped in V_o subjugates an orbital which overlaps with the shell

of adjacent Co ions. According to the Hund's rule and Pauli Exclusion Principle, the trapped electrons should have spins in direction parallel to the neighboring two Co ions, which lead to arise the observed FM ordering. As it is well known that CeO_2 at nanoscale itself is bending to form a V_o that's why it is considered to be potential for oxygen storage medium. Furthermore, in order to maintain the charge neutrality in the system, the divalent or trivalent Co doping ions lead to more V_o in doped CeO_2 nanoparticles [172]. It is also interestingly observed that the H_c values have been decreased with Co doping which indicates the magnetic phase transition towards super-paramagnetic behavior of the synthesized Co doped CeO_2 nanoparticles. The expected super-paramagnetism phase can be arisen in nanoparticles due to their extremely small crystallite sizes as seen in structural investigations. Similar results are previously reported for TM doped ZnO nanostructures [173].

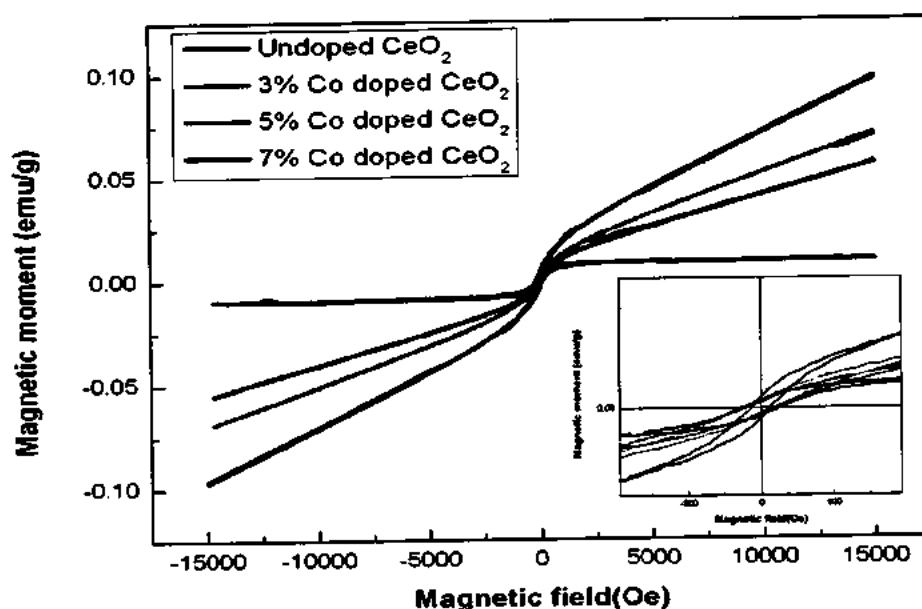


Figure 3.7: M-H loops of undoped and Co-doped CeO_2 nanoparticles (Inset of the figure shows opened loops)

3.2.6 Differential cytotoxicity analysis

Cancer remains one of the major causes of mortality in the world for many past decades [174]. Recently, inorganic nanoparticles with strong magnetic characteristics have attracted enormous attention in cancer therapy and diagnosis [105, 175-77]. The cell viability of both healthy and cancerous cells is depicted in Fig. 3.8. It can be observed that undoped, 3 and 5% Co doped CeO_2 nanoparticles have inhibited the cell viability of the cancerous cells almost by 40% without harming the healthy cells. This behavior of these nanoparticles indicates their selective/differential cytotoxicity. At 7% Co doping, the particles become toxic to normal cells as well. The toxicity of the synthesized undoped and Co doped CeO_2 nanoparticles is mostly associated with generation of reactive oxygen species (ROS). It is reported that the potential redox characteristics of CeO_2 nanoparticles play major part in ROS generation [66].

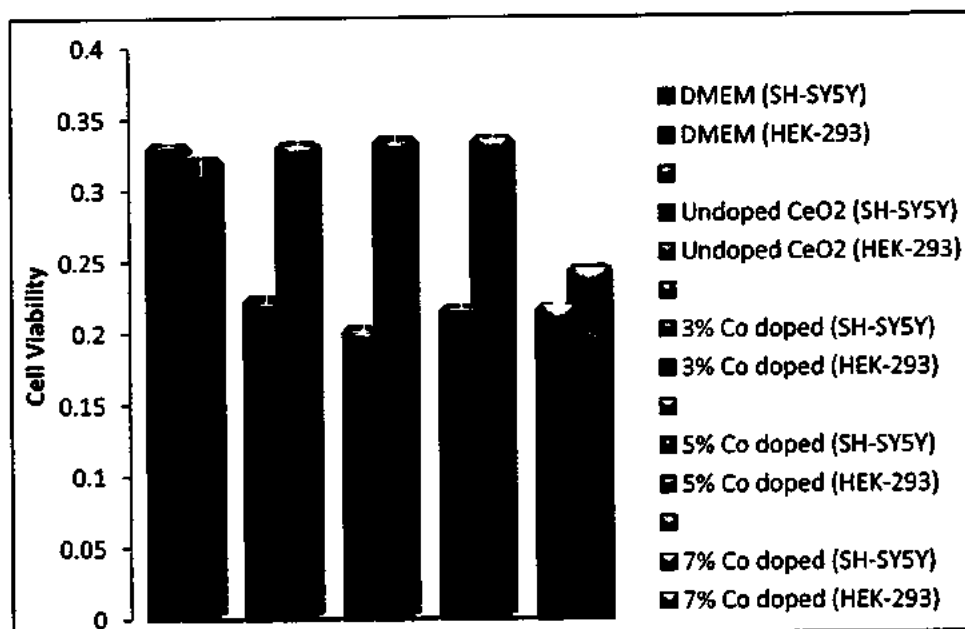


Figure 3.8: Effect of undoped & Co doped CeO_2 nanoparticles on Neuroblastoma & HEK-293 cells viability

In order to verify whether the differential cytotoxicity of the prepared nanoparticles is due to ROS generation or not, we performed the ROS generation study. Uncontrolled and excess production of ROS in cells always has damaging effects on the cells. Therefore

exposing the cells to external chemicals induces oxygen containing radicals in the cells which create imbalance in the amount of ROS within the cells. The excess ROS generation causes oxidative stress in the cells thus leading to destruction of cells via cell membrane rupture, apoptosis and even necrosis [178].

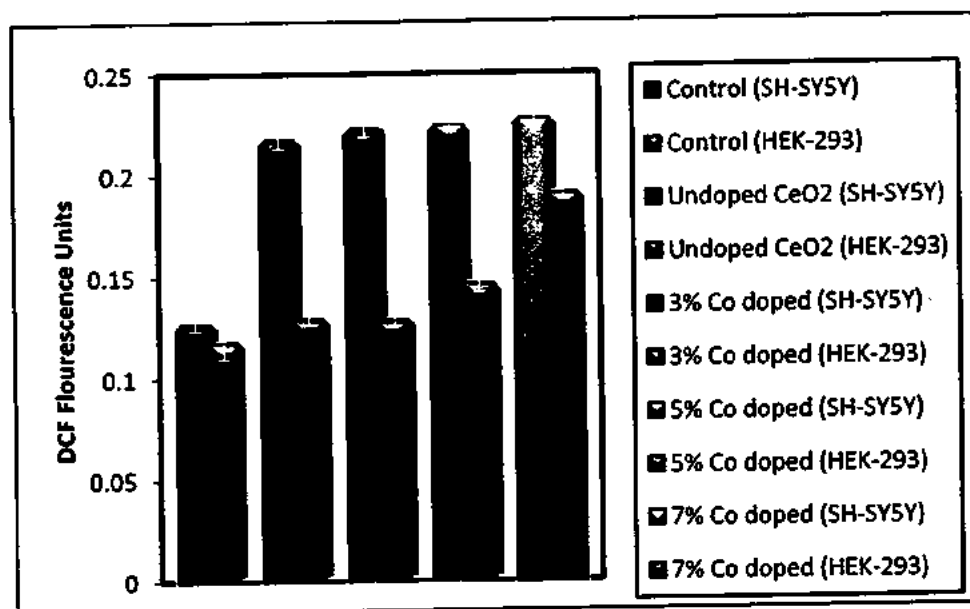


Figure 3.9: Reactive oxygen species (ROS) production in Neuroblastoma & HEK-293 Cells after incubation with undoped and Co doped CeO₂ nanoparticles

Fig. 3.9 shows the ROS generation in both healthy and cancerous cells. It is found that the toxicity of the prepared nanoparticles strictly follow the ROS generation pattern. The undoped and Co doped CeO₂ nanoparticles generate significant amount of ROS in cancerous cells while negligible amount of ROS is produced in healthy cells. The 7% Co doped CeO₂ particles cause an increase in intracellular ROS in normal cells as well which explains why the particles are toxic to these cells. Our detailed study confirms that ROS generations play very important role in the toxicity of the CeO₂ nanoparticles. Here, a question arises that why undoped and Co doped CeO₂ nanoparticles are not generating higher amounts of ROS in healthy cells. Healthy cells may provide basic atmosphere that supports the redox cycle between +3 and +4 oxidation states of CeO₂ nanoparticles, thus resulting in no significant

increase in ROS in the cell. However cancer cells have slightly acidic atmosphere which doesn't support this redox cycle between oxidation states rather increases the generation of free radicals by oxidation of lipids, proteins and various enzymes present in the cancer cells, thus increasing ROS level in the cell and hence oxidative stress that causes cell death [179]. These prepared nanoparticles exhibit the sufficient anticancer activity while demonstrating safe behavior towards healthy cells. This behavior along with the RTFM nature makes them potential for targeted cancer therapy. As due to their magnetic nature, these nanoparticles can be guided towards the specific part of the body with the help of external applied magnetic field.

Chapter No.4

Synthesis, Characterization and Anticancer Study of Fe Doped CeO₂ Nanoparticles

4.1 Introduction

The defects chemistry and other physio-chemical properties of CeO₂ nanostructures can be tuned by different ways such as thermal annealing, ion beam irradiation and selective metal doping [122]. Among these, metal doping is considered to be an easy and effective tool and has been widely used by various research groups to modify the electrical, optical, catalytic and magnetic properties of CeO₂ nanostructures [87, 180-182]. In this thesis work Fe is used as dopant for CeO₂ nanostructures owing to following reasons;

- i. It can induce ferromagnetism in CeO₂ nanostructures which is potential in spintronics and targeted cancer therapy [182].
- ii. It can reduce the band gap of CeO₂ nanostructures to great extent which is useful for their photodynamic activity [180].
- iii. It can make possible fenton reactions, which helps in its photodynamic activity by producing large number of hydroxyl radicals [182, 183].

Several authors have reported synthesis and characteristics of Fe doped CeO₂ nanostructures. D. Channei et al. have reported Fe doping induced enhancement in the photocatalytic degradation activity of CeO₂ thin films and proposed that Fe ions act as electron acceptors or donors [180]. S. Phokha et al. have reported RTFM in Fe doped CeO₂ nanospheres [87]. From the current available literature, we have reached the conclusion that Fe doping may induce RTFM and enhance the anticancer activity of CeO₂ nanostructures by acting as electron donor or acceptor, generating defects and fenton reactions. Therefore in this study, Fe doped CeO₂ nanoparticles have been prepared and characterized for structural,

Raman, optical, electrical and magnetic characteristics. Moreover, cytotoxicity of the synthesized nanostructures has been determined towards health and cancerous cells.

4.2 Results and Discussions

4.2.1 Structural and morphological investigations

The structural characteristics and phase purity of the prepared $\text{Fe}_x\text{Ce}_{1-x}\text{O}_2$ nanoparticles have been examined by XRD. Fig. 4.1(a) depicts XRD patterns of the synthesized nanostructures. Each of the peaks in XRD patterns can be well indexed to cubic fluorite structure of CeO_2 according to the JCPDS (card no. 34-0394) with no extra phases linked with Fe or other impurities. The peaks intensities have been observed to decrease systematically with Fe doping which demonstrates a decrease in the crystallinity of the samples. Moreover, it has been found that at higher Fe doping, the (111) has slight shift towards higher angle as shown in Fig. 4.1(b) which may be associated with the variations in lattice parameters by doping.

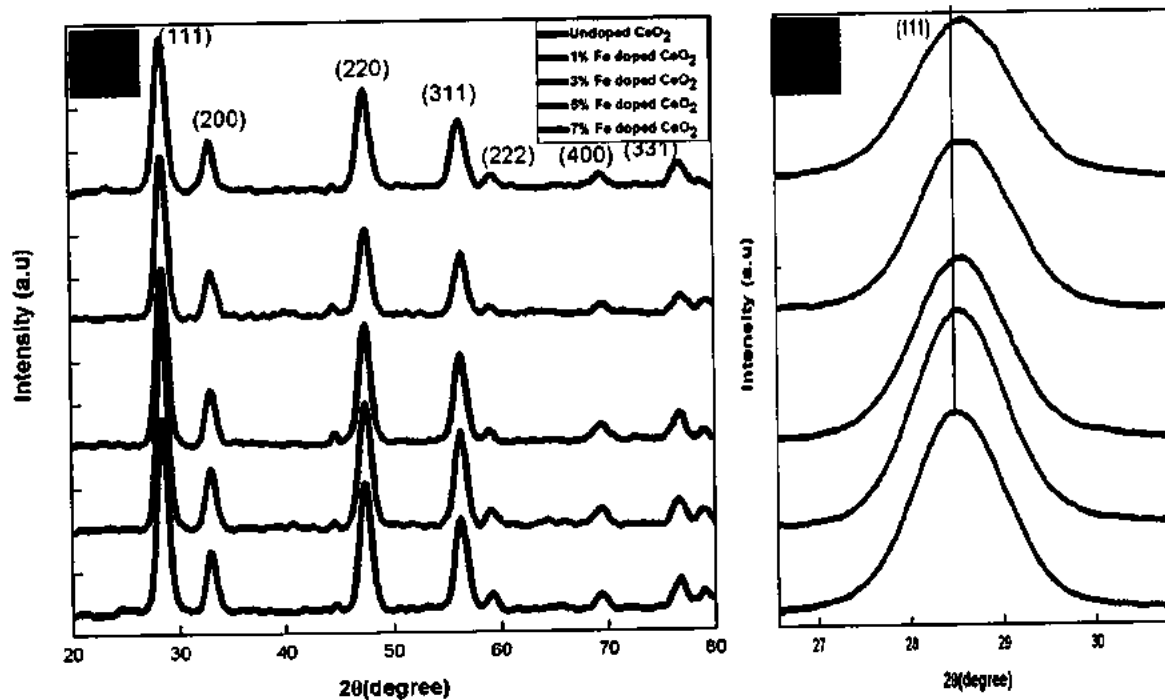


Figure 4.1: a) XRD patterns of the prepared samples b) shift in the (111) plane with Fe doping

The lattice parameters and average crystallite sizes are found to slightly decrease with Fe doping (Table 6.1) which may be due to the replacement of larger ionic radii Ce ions (1.01 Å) by a smaller ionic radii Fe ions (0.64 Å) [184]. The absence of the extra phases, decrease in lattice parameters and crystallite size clearly shows the successful doping of Fe ions into CeO₂ host matrix.

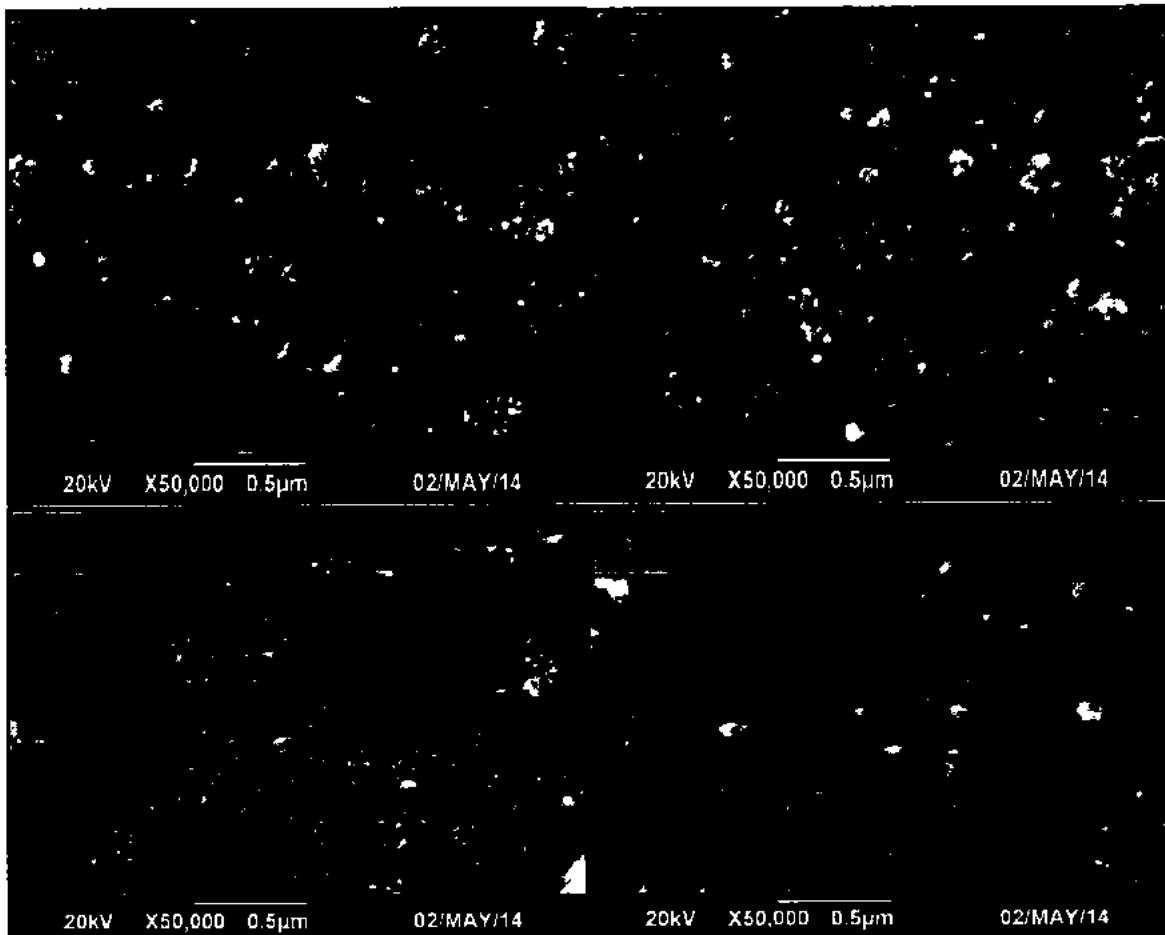


Figure 4.2: SEM images of (a) 1% (b) 3% (c) 5% and (d) 7% Fe doped CeO₂ nanoparticles

The synthesized samples morphologies and particle sizes have been studied by SEM and shown in Fig. 4.2. The shape of the particles is found to be mostly spherical with the presence of small number of nanorods in Fe doped CeO₂ samples. The average particle size of the undoped CeO₂ sample is 28 nm which is observed to decrease down to 22 nm with the increase in Fe doping level as listed in Table 6.1. In 5% and 7% Fe doped CeO₂ samples there are some large micron sized particles which may be due to agglomeration of small particles

into large aggregates. This agglomeration can be due to increase in the difference of charge in crystal by replacing Fe with Ce as well as ferromagnetic nature particles of Fe doping. It is concluded from SEM results that highly ultrafine nanoparticles of $\text{Fe}_x\text{Ce}_{1-x}\text{O}_2$ can be synthesized by chemical co-precipitation technique.

4.2.2 Analysis of surface area

Chemical and biological reactivity of nanomaterials is highly sensitive to SSA (surface to volume ratio) offered by the materials. So it is very vital to have an exact idea about SSA to have well understanding of its various properties. As we proceed from bulk to nano, number of the available abundant reactive sites on the surface of NPs as well as the free surface energy increases with increasing SSA [48, 49]. Moreover, magnetic properties of the materials are also very dependent on SSA of the material [50, 51].

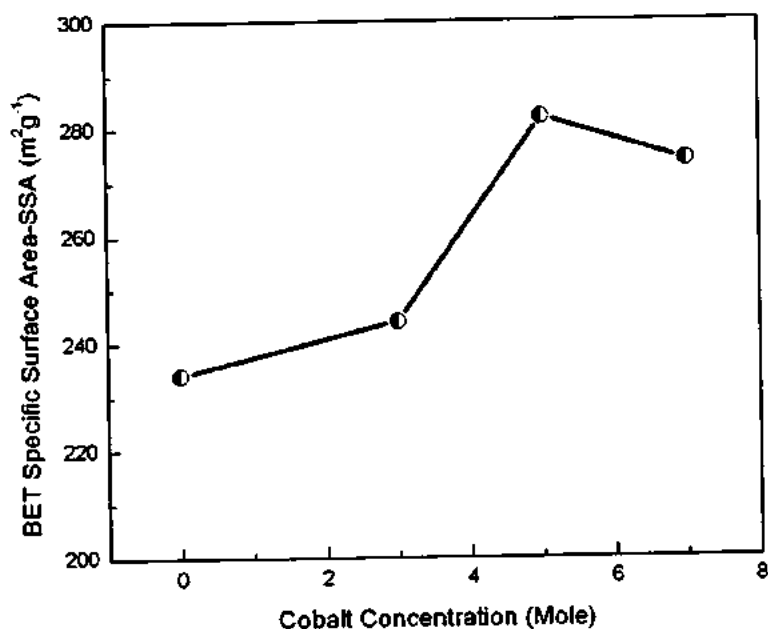


Figure 4.3: BET-SSA Analysis of $\text{Ce}_{1-x}\text{Fe}_x\text{O}_2$ nanoparticles

BET technique has been employed to calculate the SSA of the prepared undoped and Fe doped CeO_2 nanoparticles which works on the principle of nitrogen adsorption-desorption. The SSA obtained for as prepared CeO_2 nanoparticles is found to be $234 \text{ m}^2/\text{g}$ and is slightly

enhances by Fe doping in the host matrices as shown in Fig. 4.3. This enhancement in the SSA with Fe doping of CeO₂ nanoparticles may be linked to the slight decrease in the particles with doping. This higher reported value of SSA of the synthesized nanoparticles may have vital role in their cytotoxicity.

4.2.3 Raman and optical characterizations

Raman spectroscopy is useful technique for studying the structural properties of nanomaterials and their phase purities. It has a capability to detect secondary phases even at very minute level. The phase purity and cubic fluorite structure of the synthesized Fe_xCe_{1-x}O₂ nanoparticles have been validated via Raman spectroscopy. Fig. 4.4 shows the Raman spectra of Fe_xCe_{1-x}O₂ nanoparticles. The spectrum of undoped CeO₂ nanoparticles exhibits one clear peak at 445 cm⁻¹ which is assigned to F_{2g} mode of cubic fluorite structure of CeO₂. Furthermore, the peak intensity is found to decrease with Fe doping which shows the decrease in the crystalline quality of the nanoparticles upon doping. Hence Raman spectroscopy results confirm the XRD results.

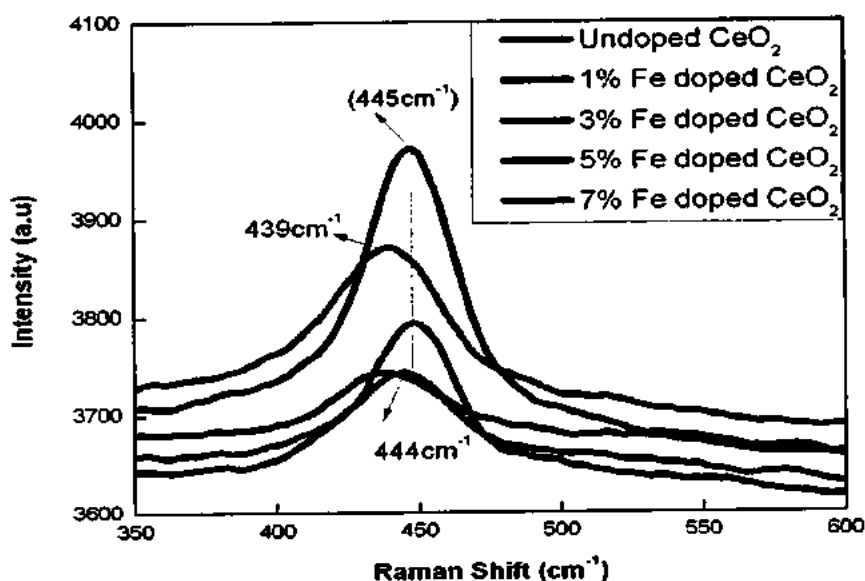


Figure 4.4: Raman spectra of the prepared nanoparticles

Moreover, a red shift, symmetric peak broadening as well as suppression of peak intensity in the F_{2g} mode peak with Fe doping can be clearly seen which may be attributed to the introduction of defects such as V_o and interstitial defects etc. into the system, as discussed in Chapter No. 3. For 5% and 7% doped nanoparticles, the red shift is smaller as compared to the 3% doped which may be linked with presence of micron size particles as depicted in SEM micrographs as Raman peak position is very sensitive to particle size.

Optical properties of $Fe_xCe_{1-x}O_2$ nanoparticles have been studied using UV-visible absorption spectroscopy. UV-visible absorption spectra of the prepared nanoparticles are shown in Fig. 4.5. A well sharp band edge absorption peak is observed for all the synthesized nanoparticles. This strong absorption peak is believed to arise from the electronic transition from 2p states of O to 4f states of Ce [185]. It can be clearly seen from the absorption spectra that absorption in the visible region is enhanced with Fe doping which might play important role in the cytotoxicity of the synthesized nanostructures. Optical band gap energies for the synthesized nanoparticles have been calculated by the Tauc relation 3.2. The calculated band energy values are 3.19, 2.75, 2.64, 2.65 and 2.5 eV for undoped, 1%, 3%, 5% and 7% Fe doped CeO_2 nanoparticles respectively. The observed band gap energy value for undoped CeO_2 nanoparticles is much smaller than bulk one. Fe doping significantly has decreased the band gap energies of all the prepared CeO_2 nanoparticles. The decrease in band gap energies may be attributed to the fact that Fe ions have created defects or impurity level below the conduction band and resulted in band gap reduction [182, 186]. The increase in band gap energies beyond certain limit of Fe doping may be understood on the basis that at higher concentration of Fe^{3+} ions, the band filling effect may arise which causes the enlargement of the band gap [187].

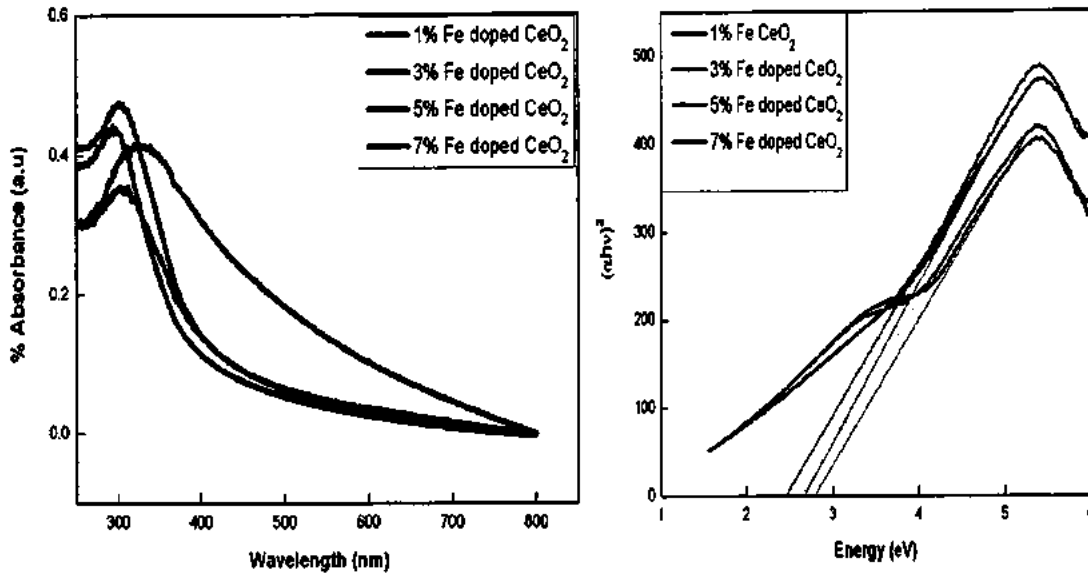


Figure 4.5: (a): UV-Vis absorption spectra of the $\text{Fe}_x\text{Ce}_{1-x}\text{O}_2$ nanoparticles (b): Plots of $(\alpha h\nu)^2$ as a function of photon energy E for the synthesized nanoparticles.

4.2.4 Dielectric properties

The dielectric properties of the synthesized undoped and Fe doped CeO_2 nanoparticles have been investigated by making their circular pellets of same dimensions and using the same method as mentioned in last chapters and then ϵ' , ϵ'' and σ_{AC} have been measured over a wide range of AC frequency (3 KHz- 5 MHz).

Figure 4.6 (a) depicts the influence of Fe doping on σ_{AC} of synthesized CeO_2 nanostructures. In all the samples, σ_{AC} is approximately constant at low frequencies and then increases above a definite characteristic point with the increase in frequency, following power law, which indicates that the σ_{AC} is directly proportional to the AC frequency. Also, it is observed from Fig. 4.6 (a) that at any frequency, σ_{AC} of CeO_2 nanostructures increases with the increase in Fe doping concentration levels. This variation of σ_{AC} with AC frequency may be linked with the fact that when Fe^{3+} ions replaces Ce^{4+} ions it is more probable that with Fe doping there will be more free electrons in the system which may increase the σ_{AC} of CeO_2

nanostructures. Moreover, in order to accomplish charge neutrality, defects will be created in the host lattice which in turn will lead to enhanced σ_{AC} .

The ϵ' for all the synthesized samples were calculated using the formula given in equation (2.5) as mentioned in Chapter No. 2. The effect of Fe doping on ϵ' for all the synthesized samples is shown in Fig. 4.6 (b). This graph indicates the decrease in ϵ' with the increase in AC frequency up to 2 MHz and then has a constant trend. This decline in ϵ' may be attributed to the fact that the charge carriers can easily tunnel into the grains but these charge carriers gather at the grain boundaries under the influence of external field which leads to a large polarization owing to high ϵ' at low frequency [166]. Moreover, it is also vividly observed from Fig. 4.6(a) that Fe doping results into the enhancement of ϵ' which may be linked to the fact that TM ion dopant introduces the higher dielectric polarization as compared to that in bare CeO₂ [167].

Effect of Fe doping on the variation of ϵ'' as a function of frequency in the prescribed range is shown in Fig. 4.6 (c). The decrease in ϵ'' is observed with the increasing AC frequency for all the synthesized nanoparticles. This decrease in ϵ'' as a function of AC frequency can be linked to the fact that extra amount of energy is required for the exchange of electrons at grain boundaries so ϵ'' is higher at lower frequency. Furthermore, Fig. 4.6(b) also depicts that for each value of AC frequency, value of ϵ'' also increases with Fe doping into CeO₂ matrix. This evaluation in ϵ'' can be linked to the fact that there is constraint of more energy for the exchange of electrons between Ce ions and Fe ions [167].

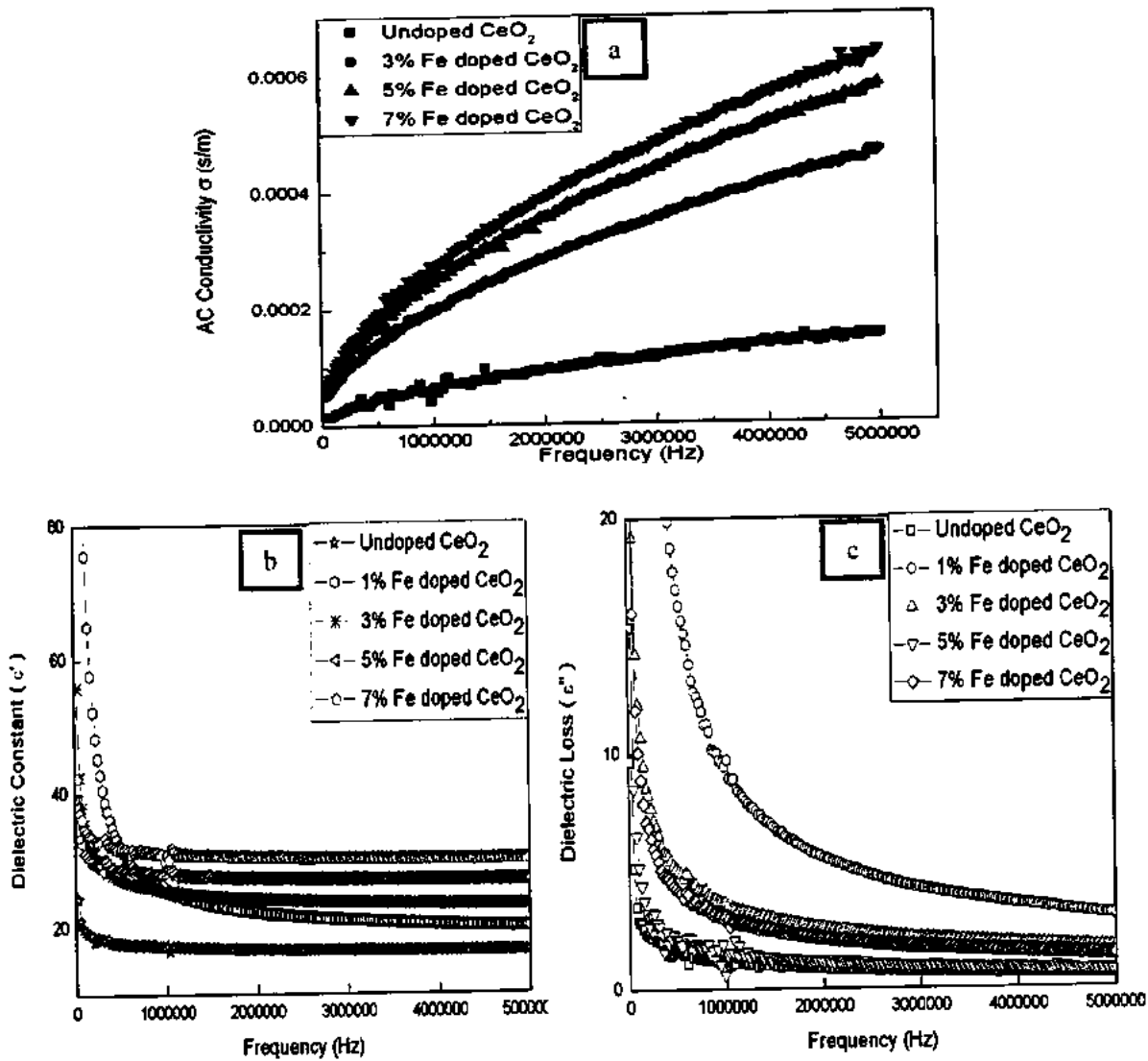


Figure 4.6: (a): Dielectric Constant (ϵ'), (b): Dielectric Loss (ϵ''), (c): AC conductivity (δ_{AC}), variations as a function of AC frequency

4.2.5. Magnetic study

Fig. 4.7 shows the room temperature magnetization versus magnetic field (M-H) curves for the Fe_xCe_{1-x}O₂ nanoparticles. The synthesized undoped nanoparticles exhibit weak RTFM, which is observed to enhance with the increase in Fe doping level. The M_s value of pristine CeO₂ nanoparticles is found to be 0.0083 emu/g which increases up to 0.0126 emu/g for 7% Fe doped CeO₂ nanoparticles. The M_s value is observed to increase systematically with Fe doping which is in good agreement with earlier reported studies [87]. The interesting thing to be noticed is that RTFM is also observed for pristine CeO₂ nanoparticles although it

is anti-ferromagnetic in bulk form. Weak RTFM is previously reported for pure CeO₂ nanostructures in literature which is assigned to the exchange interaction between electron spin moment of Ce ions and V_o (i.e. Ce³⁺ - V_o - Ce³⁺) [179].

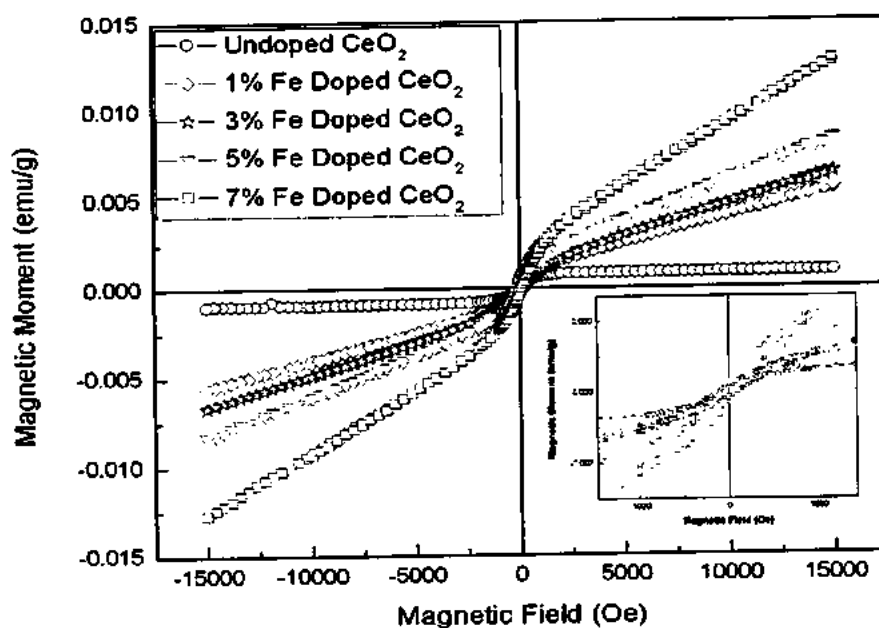


Figure 4.7: M-H loops of undoped and Fe doped CeO₂ nanoparticles (Inset of the figure shows opened loops)

These V_o can trap an electron and form F-center, which make up a bound polaron [88, 114, 171]. The increase in the M_s value upon Fe doping may be understood on the fact that Fe doping into CeO₂ matrix lead to enhanced level of V_o which will lead to more exchange integrations with Ce³⁺ and enhance magnetization [188, 189]. Moreover, the Fe³⁺ ions doping can also lead to enhance magnetic characteristics via same exchange interaction (i.e. Fe³⁺ - V_o - Ce³⁺) [87]. Both type of bound polarons can overlap the neighboring polarons and lead to long range RTFM in CeO₂ nanoparticles.

4.2.6 Differential cytotoxicity analysis

Cytotoxicity of Fe_xCe_{1-x}O₂ nanoparticles has been determined towards Neuroblastoma cancer & HEK-293 healthy cells via CCK-8 assay. Cell viability of these cells treated with

the synthesized nanoparticles for 24 h is shown in Fig. 4.8. It is observed that viability of healthy cells remain unchanged comparing to the controlled cells after treatment, which demonstrates the bio-safety of these nanoparticles. However, Neuroblastoma cancer cells viability is reduced to almost half by undoped CeO₂ nanoparticles and is found to reduce further with Fe doping. It can be seen from Fig. 4.8 that cancer cells viability is systematically reduced with the increase in Fe doping concentration. These findings confirm the differential or selective cytotoxicity of pristine and Fe doped CeO₂ nanoparticles.

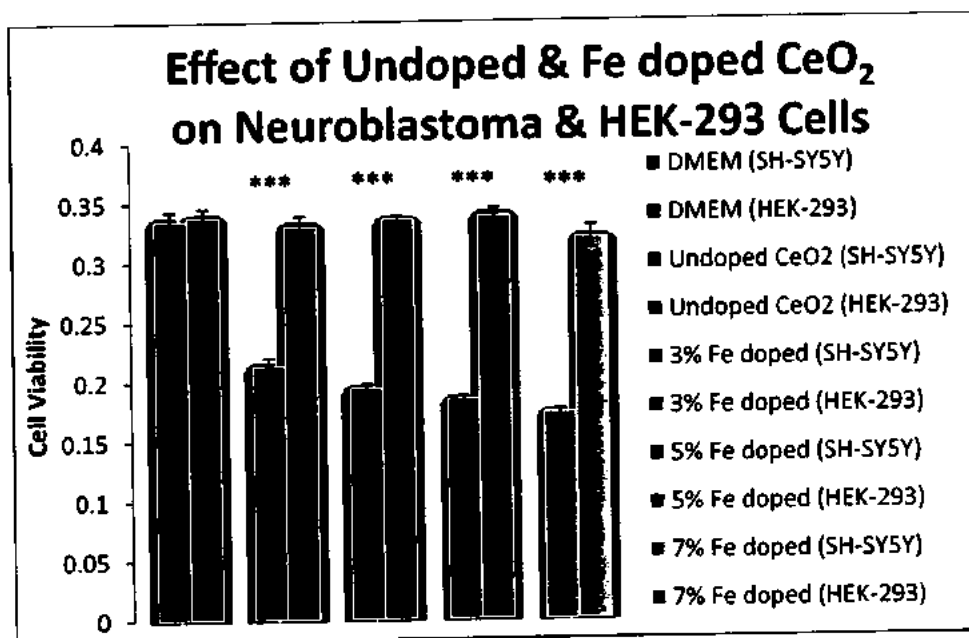


Figure 4.8: Effect of undoped & Fe doped CeO₂ nanoparticles on Neuroblastoma & HEK-293 Cells viability

The cytotoxicity of CeO₂ nanoparticles is reported to be due to ROS generation, oxidative stress, electrostatic interactions between cells and nanoparticles and damaging of cell membranes [118, 190 and 191]. Upon illumination of light, electron hole pairs are generated in CeO₂ nanoparticles which interact with water molecules and oxygen on the surface to produce various types of ROS likewise hydroxyl radicals, super oxides ion and H₂O₂ etc. [192]. The generated ROS can lead to cell death via different mechanisms such as lipid peroxidation, apoptosis and cell membrane damage [120, 121]. But the main issue is the

short half-life of electron hole pair, which can recombine before interacting with the water and oxygen. It is reported that defects in nanomaterials act as trapping centers for photodynamically produced electrons [112]. Moreover, doping in nanomaterials leads to the formation of crystal defects which results in the enhancement of ROS generation [112, 122]. In our case, Raman spectroscopy and magnetic studies confirmed the enhancement in V_o with Fe doping. Hence, the anticancer activity of the synthesized CeO_2 nanoparticles and enhancement of it with Fe doping may be attributed to ROS generation. Enhancement in ROS generation with defects is still questionable.

We have experimentally investigated the ROS generation caused by $Fe_xCe_{1-x}O_2$ nanoparticles both in healthy and cancer cells. Fig. 4.9 demonstrates high level of ROS generation in case of cancerous cells which is also observed to increase with Fe doping level. But, no or negligible enhancement in ROS generation as compared to control has been found for healthy cells. Hence, it is confirmed that the selective toxicity of the synthesized nanoparticles is due to ROS generation. The difference in the level of ROS generated by $Fe_xCe_{1-x}O_2$ nanoparticles in two different types of cell lines may be understood on the basis of atmosphere provided by them. Healthy cells provide basic environment to nanoparticles which resist ROS generation while cancerous cells provide slightly acidic atmosphere which assists ROS production [179]

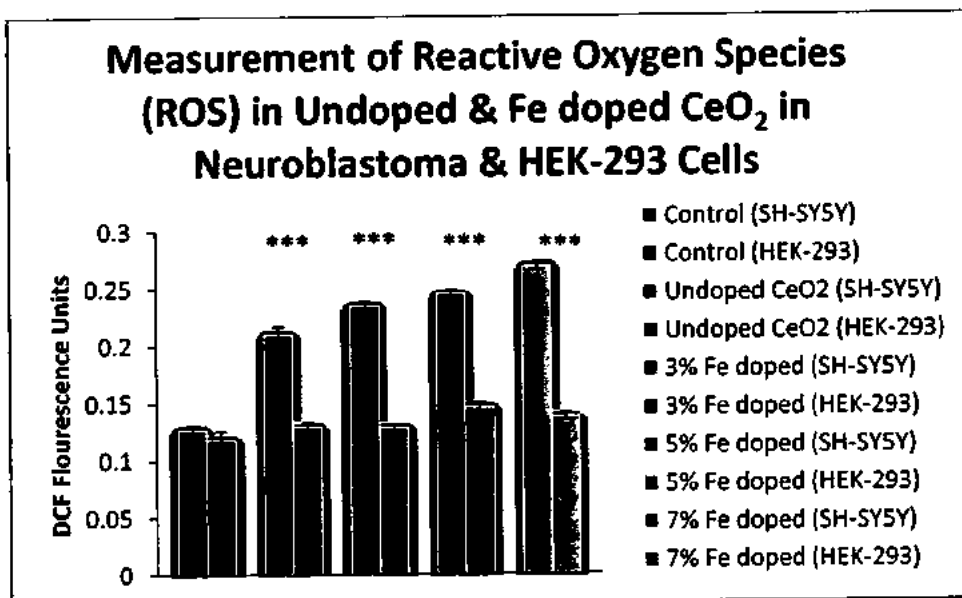


Figure 4.9: Reactive oxygen species (ROS) production in Neuroblastoma & HEK-293 Cells after incubation of undoped and Fe doped CeO₂ nanoparticles

Chapter No.5

Synthesis, Characterization and Anticancer Study of Ni Doped CeO₂ Nanoparticles

5.1 Introduction

CeO₂ is a very promising material having numerous applications at nanoscale especially in medical field such as anticancer activity [112, 113]. Undoped CeO₂ nanoparticles exhibit weak ferromagnetism which hinders its application in targeted cancer therapy [114]. However, strong enough ferromagnetism can be originated in CeO₂ nanoparticles via transition metal (TM) doping [115]. Furthermore, TM doping into CeO₂ nanoparticles matrix can lead to enhanced V_o formation which are very important for inhibition of cancer cells by nanomaterials [87]. In this study, Ni is doped as TM into CeO₂ nanoparticles because Ni ions can be easily substituted on the sites of Ce ions because of its smaller ionic radii. Previously, Ni dopant has been reported to enhance the ferromagnetic and catalytic activity of CeO₂ nanostructures which hints its possible applications in targeted cancer therapy [193, 151]. This dopant is selected as till date there is no article published on the anticancer activity of Ni doped CeO₂. Keeping this in view, Ni dopant induced effects on the ferromagnetic and cytotoxicity of the CeO₂ nanoparticles synthesized by facile chemical method has been studied.

5.2 Results and Discussions

5.2.1 Structural and morphological investigations

The typical XRD patterns of the Ni_xCe_{1-x}O₂ samples annealed at 300 °C are depicted in Fig. 5.1 (a). The peak positions in the XRD patterns of the synthesized samples exhibit the typical cubic fluorite structure of CeO₂. The absence of NiO or any other impurity phases reveal phase purity of the prepared samples. It can be observed from the patterns in Fig.

5.1(b) that there is a slight shift towards higher angles with Ni doping in host matrix. This might be due to lattice contraction initiated by the dopant ions. Furthermore, it also hints the possible substitution of Ni ions on the sites of Ce ions.

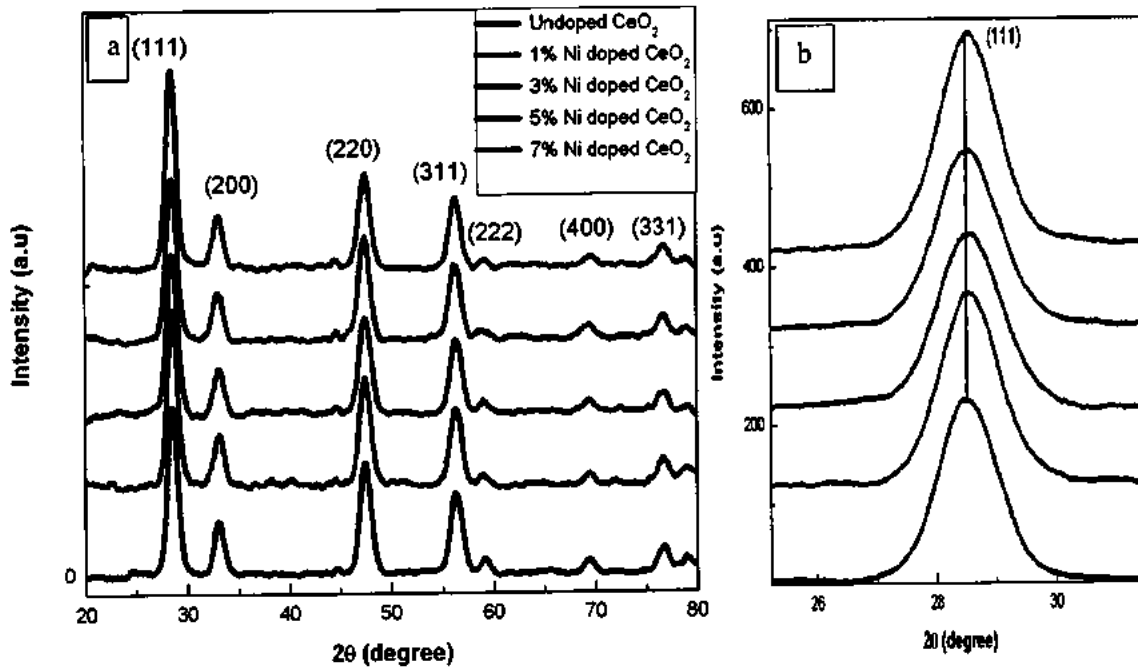


Figure 5.1: a) XRD patterns of the prepared samples and b) Ni loading induced shift in the (111) plane

The crystallite sized (D) and lattice constants ($a = b = c$) have been calculated through the relations (5.1) and (3.1) respectively.

$$D = \frac{0.89\lambda}{\beta \cos\theta} \quad (5.1)$$

The crystallite size for undoped CeO₂ sample is calculated to be 7 nm which has been decreased down to 5 nm with Ni doping. Moreover, the value of lattice constant “a” is also decreased with Ni doping as can be seen from Table 6.1. This decrease in microstructural parameters of CeO₂ with the introduction of Ni dopant may be explained as larger ionic radii of Ce⁴⁺ (1.01 Å) ions are being replaced by smaller ionic radii Ni²⁺ (0.69 Å) ions. This difference in the ionic radii of the host and dopant ions leads to reduction of crystallite size and lattice contraction [151].

Morphologies of the synthesized samples have been examined by SEM. Fig. 5.2(a) - (d) depicts the typical morphology of the $\text{Ni}_x\text{Ce}_{1-x}\text{O}_2$ samples. SEM micrographs clearly indicate the spherical particles like nanostructure morphologies for all samples. The synthesized samples have homogenous particle size shape distribution. The average particle size is observed to decrease from 28 nm down to 22 nm as listed in Table 6.1. Similar decrease in the average crystallite size with Ni doping has also been seen in XRD results.

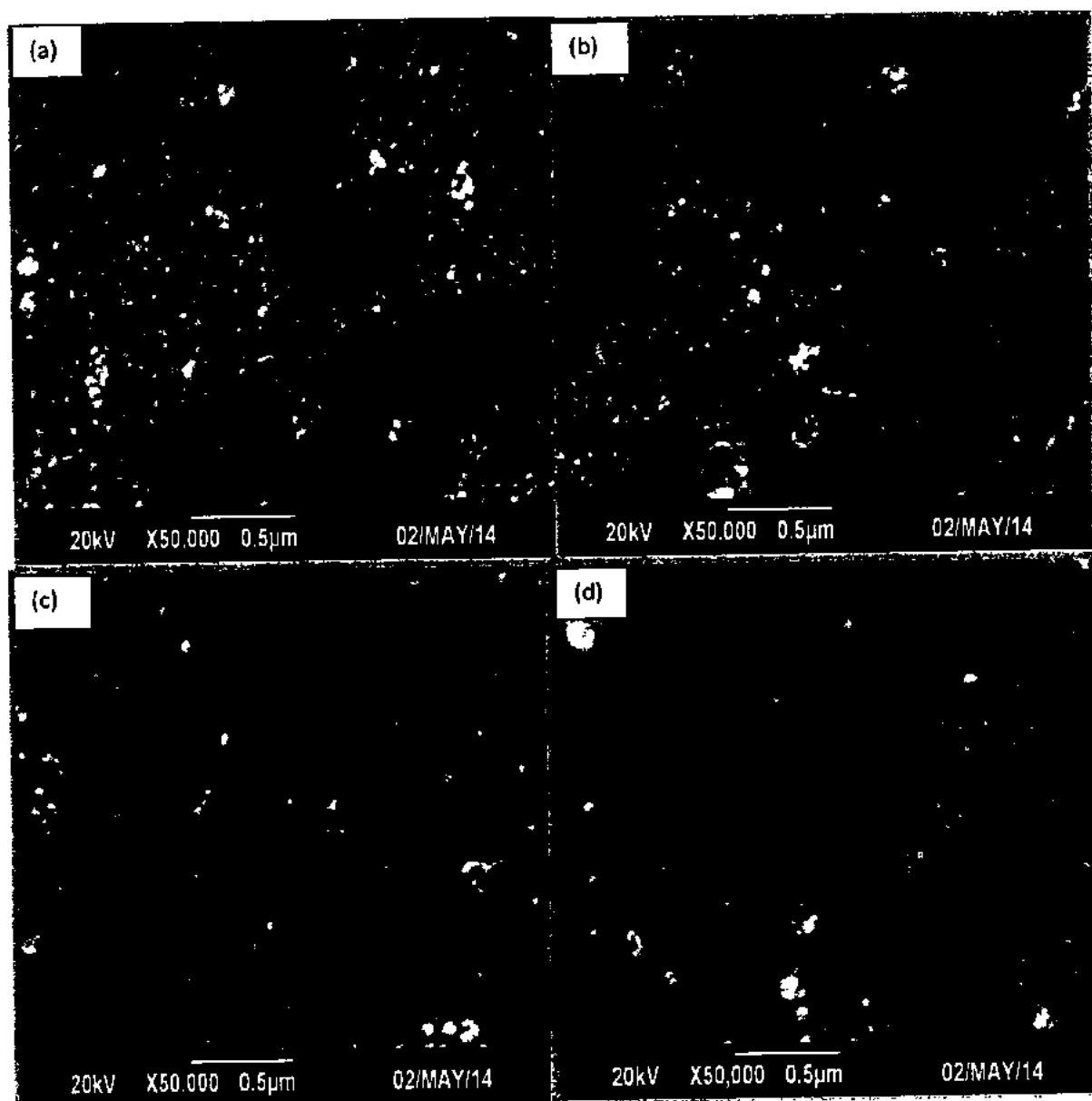


Figure 5.2: SEM images of prepared CeO_2 nanoparticles with (a) 1% (b) 3% (c) 5% and (d) 7% of Ni doping

5.2.2 Analysis of surface area

Nanomaterials are believed to be more reactive both chemically and biologically as compared to their bulk ones mainly because of higher surface area (surface to volume ratio). Therefore, exact knowledge about the surface area of the synthesized nanoparticles is crucial for understanding their physical properties. SSA of the prepared undoped and Ni-doped CeO₂ nanoparticles has been evaluated using BET technique which is based on nitrogen adsorption-desorption. The SSA obtained for undoped CeO₂ nanoparticles is found to be 234 m²/g and is increased with the Ni doping up to 256 m²/g as shown in Fig. 5.3. Ni doping enhancement in the SSA of CeO₂ nanoparticles may be assigned to reduction in the particles with doping [194] as observed in SEM investigations. This remarkable enhancement in SSA of the synthesized nanoparticles may be very effective in tuning their physical properties and cytotoxicity.

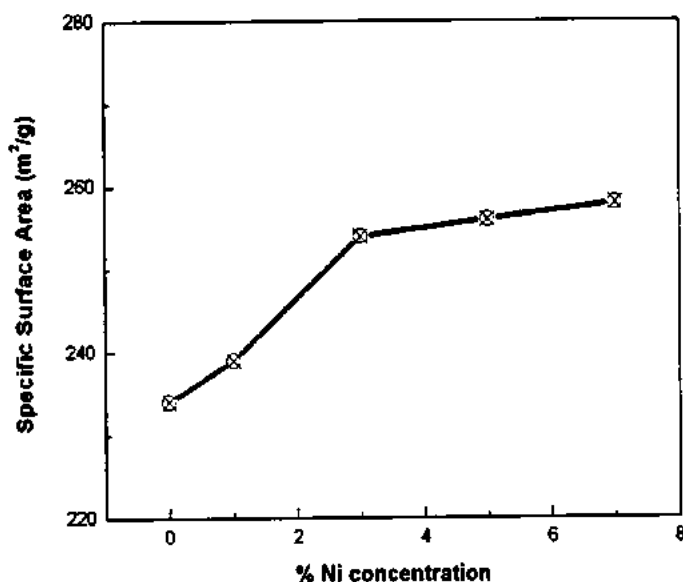


Figure 5.3: BET-SSA as a function of Ni doping percentage in host CeO₂ nanoparticles

5.2.3 Raman and optical characterizations

The microstructural properties of the synthesized samples have been analyzed via Raman spectroscopy. Raman spectroscopy is very sensitive to minute amounts of impurities and also structural defects such as V_o. Therefore, in order to validate the XRD results, Raman

spectra for the synthesized samples have been recorded at room temperature in the wavenumber range of 300-700 cm^{-1} and shown in Fig. 5.4. The appearance of Raman band at 445 cm^{-1} corresponding to the first order F_{2g} Raman active mode of the cubic fluorite structure of CeO_2 for undoped sample validate the XRD results. This Raman peak has huge shift toward lower wave number region comparing to that of bulk CeO_2 which is often associated with the formation of V_o in the system [73]. The doping of Ni ions into CeO_2 lattice resulted in suppression of the F_{2g} Raman active mode which may be attributed to the formation of more V_o as a result of dopant induced effects [74].

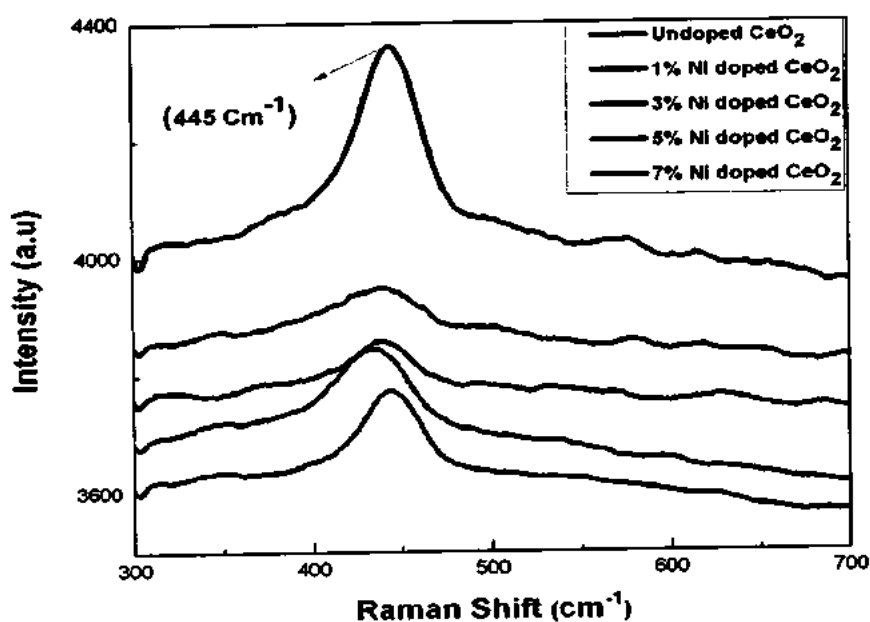


Figure 5.4: Raman spectra of the synthesized nanoparticles

Optical properties of the nanomaterials are of immense importance for the biological activities. Optical properties play major role in the photodynamic cytotoxicity of the nanomaterials while magnetic properties define the fate of nanomaterials in their application in targeted cancer therapy. Optical characteristics of the synthesized nanoparticles have been studied via UV-Vis absorption spectroscopy. Fig. 5.5 depicts the absorption spectra of $\text{Ni}_x\text{Ce}_{1-x}\text{O}_2$ nanoparticles. The absorption spectra reveal significant changes in overall absorption and the band edge absorption peak of CeO_2 nanoparticles with Ni doping. To

further elaborate the Ni doping induced effects on the optical properties of CeO₂ nanoparticles, band gap energies for the synthesized nanoparticles have been calculated using Tauc relation (3.2) as shown in the inset of Fig. 5.5. The band gap energy E_g calculated for undoped CeO₂ nanoparticles is observed to be 3.19 eV which is in good agreement with previously reported values [182]. This value of E_g drops systematically to 2.72 eV with Ni doping which indicates the significant effects of Ni ions on the optical properties of CeO₂ nanoparticles. Thurber et al. [151] observed decrease in E_g of CeO₂ nanoparticles with Ni doping which they assigned to variation in microstructural parameters such as crystallite size and lattice constants. Similar variations in microstructural parameters can also be seen in our case as listed in Table 6.1. Reduction in E_g value of CeO₂ nanoparticles has also been previously observed by other groups with Fe and Mn doping which is suggested to be due to formation of impurity level between the conduction and valance bands of CeO₂ [114]. Hence, Ni dopant induced reduction in E_g of these CeO₂ nanoparticles may be assigned to both microstructural variations as well as formation of impurity energy levels.

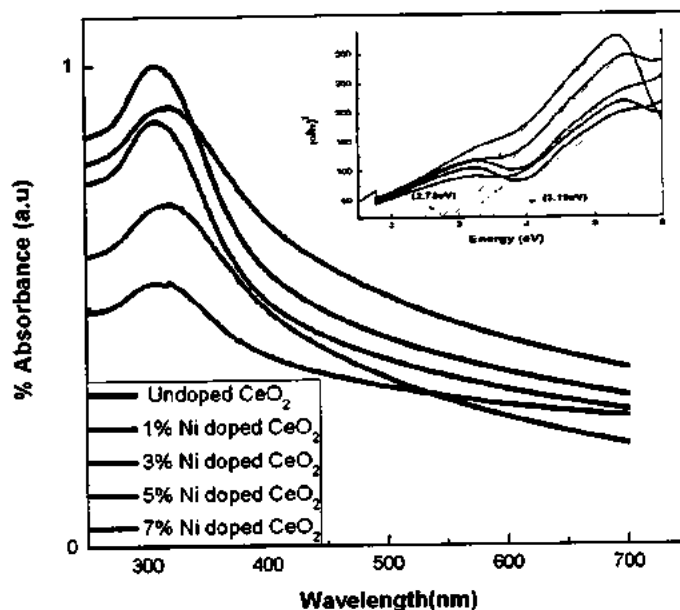


Figure 5.5: UV-visible absorption spectra of the undoped and Ni doped CeO₂ nanoparticles

(Inset shows the bandgap estimation using Tauc relation)

5.2.4 Dielectric properties

Fig. 5.6 (a) depicts the variation of ϵ' as a function of AC frequency in the range of 3 KHz- 5 MHz at ambient conditions. It is evident from the plot that all the synthesized undoped and Ni doped samples exhibit the frequency dependent trend i.e. ϵ' decreases with the increasing AC frequency. This behavior is very normal which is oftenly observed in most of the oxides and is attributed to the interfacial polarization in such materials which is explained by Maxwell-Wagner [166]. According to this model, the dielectric structure of oxides is supposed to be composed of two layers; First layer consist of conducting grains while other layer is composed of insulating grains. Thus charges gather across the grain boundaries under the action of applied external field and thus resulting into large value of polarization due to electron exchange between Ni^{2+} and Ni^{3+} ions. This polarization results into higher value of ϵ' at low frequency. Moreover, this polarization decreases with the decrease in AC frequency and finally attains a constant value due to the fact that beyond a particular frequency, exchange of electrons between cations fails to sustain their oscillations with the applied external field. Also, the larger value of ϵ' at low AC frequency may be due to many factors like V_0 , grain boundary defects and interfacial dislocation factor [195]. It is also evident that with Ni content, observed value of ϵ' is also increased which is attributed to the fact that doped sample owes higher value of dielectric polarization as compared to as prepared one [167].

Fig. 5.6 (b) elaborates the variation of ϵ'' as a function of AC frequency which depicts the decreasing trend of ϵ'' with the increasing AC frequency for all the synthesized samples. This trend of ϵ'' as a function of AC frequency can be explained using Koop's model [168] which suggests that there exists highly resistive medium at grain boundaries in the dielectric materials and excess amount of energy is required for the exchange of electrons at these grain

boundaries, so there exists higher ϵ'' at lower frequency while at lower frequency grain boundary effect is not dominant so ϵ'' is low and even eventually attains a constant value.

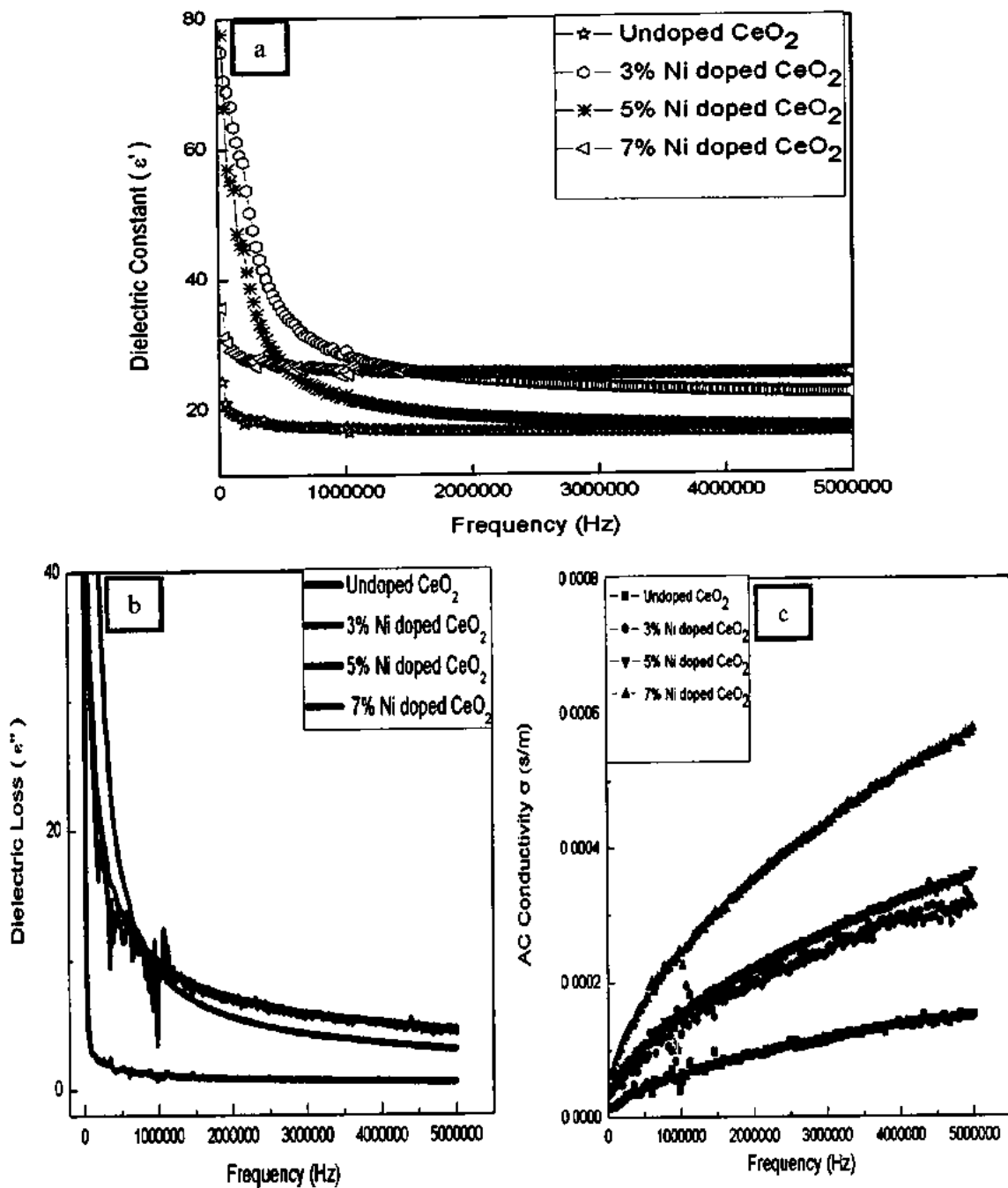


Figure 5.6: (a): Dielectric Constant (ϵ'), b): Dielectric Loss (ϵ''), (c): AC conductivity (δ_{AC}), variations as a function of AC frequency

Fig. 5.6 (c) demonstrates the influence of Ni doping on σ_{AC} as a function of AC frequency for as prepared and Ni doped CeO₂ nanoparticles. A significant enhancement in the

value of σ_{AC} is observed for all the samples with AC frequency as well as with the cation dopant content. This increase in σ_{AC} of CeO_2 with TM content can be due to the existence of V_o as observed in Raman results. These V_o leads to more free charge carriers in the system [167] thus give a significant enhancement in the value of σ_{AC} with doping. Moreover, variation of σ_{AC} with AC frequency may be associated with the reason that when Ni^{3+} ions replaces Ce^{4+} ions it is more probable that with Ni doping there will be more free electrons in the system which may increase the σ_{AC} of CeO_2 nanostructures. This enhancement in σ_{AC} and ϵ' with doping make these prepared materials very useful in many applications.

5.2.5. Magnetic study

Hysteresis loops taken for undoped and Ni doped CeO_2 nanoparticles at maximum field of 15,000 kOe are shown in Fig. 5.7. The opened loops as depicted in the inset of Fig. 5.7 indicate the ferromagnetic behavior of the synthesized nanoparticles. The ferromagnetic behavior of pristine and TM doped CeO_2 nanostructures is often associated with V_o [115]. Several research groups have previously reported RTFM in undoped CeO_2 nanostructures [88, 115]. Sundaresan et al. [179] have suggested that the exchange interaction between the spin moments of electrons originated from the surface V_o are responsible for ferromagnetic behavior of undoped CeO_2 nanostructures. Ge et al. [114] suggested that the V_o in crystal structure of CeO_2 nanocubes cause the spin polarization of the surrounding Ce ions 4f electrons which lead to their RTFM. The M_s value of CeO_2 nanostructures has been observed to increase with Ni doping as listed in Table 6.1. This enhancement in M_s values and ferromagnetic behavior of Ni doped CeO_2 nanostructures may also be explained on the bases bound magnetic polarons (BMPs) model [115, 173–179]. The BMPs are formed when the localized spins of magnetic ions i.e. Ni dopant ions in our case interact with the charge carriers bound to V_o leads to magnetic polarization of nearby local moments [114, 182 and 196]. More V_o mean formation of more BMPs. The exchange interactions between the small

amounts of Ni ions and BMPs might result in RTFM and enhanced M_s values for Ni doped CeO_2 nanostructures [115].

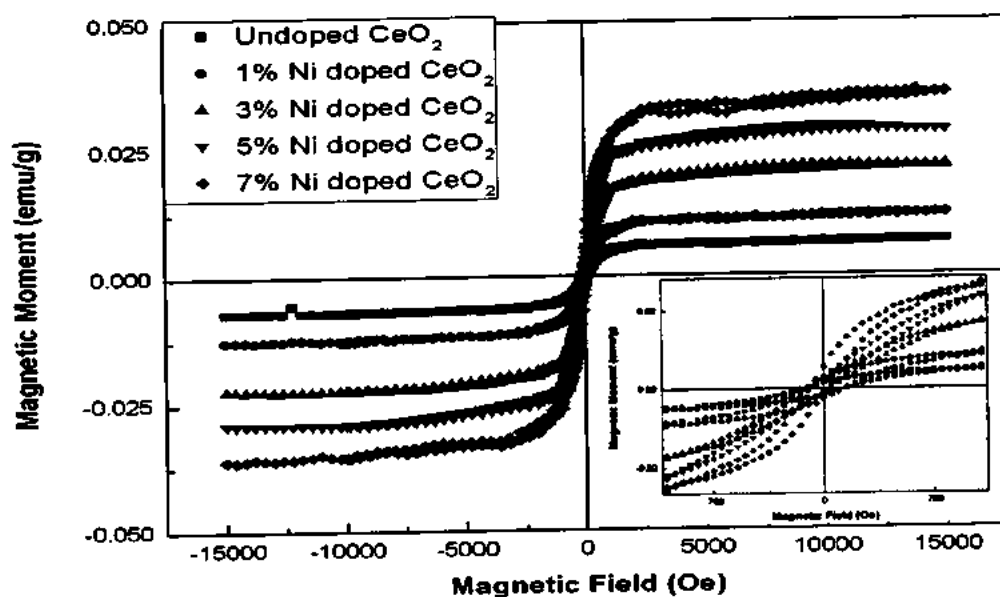


Figure 5.7: Magnetic study of synthesised samples (Inset well opened MH-loops)

5.2.6 Differential cytotoxicity analysis

The prepared $Ni_xCe_{1-x}O_2$ nanoparticles have been examined for cytotoxicity against two cell lines, SH-SY-5Y neuroblastoma cancer cell line and HEK-293 healthy cell line. These cell lines were treated with 20 $\mu\text{g/ml}$ dilutions of the synthesized $Ni_xCe_{1-x}O_2$ nanoparticles for 24 h under the visible light. The pristine CeO_2 nanoparticles have inhibited the cancer cells viability by almost 35% without harming the healthy cells viability as shown in Fig.5.8. Interestingly with the introduction of Ni dopant ions in the CeO_2 host matrix, the cancer cells viability is reduced gradually with the increase in Ni doping level while healthy cells remains unharmed. The cancer cells viability is reduced by 55% with application of 7% Ni doped CeO_2 nanoparticles. The anticancer activity of the synthesized $Ni_xCe_{1-x}O_2$ nanoparticles is quite higher as compared to that reported for other metal oxides nanostructures. Ahamed et al. [106] reported the inhibition of HepG2 and A549 cancer cell lines viability by 42 and 41% respectively using 100 $\mu\text{g/ml}$ dilutions of Fe_3O_4 nanoparticles.

ZnO: Ag nano composites (25 $\mu\text{g/ml}$ dilution) have been reported to inhibit less than 50% viability of HT144 cancer cell line [111]. Alarifiet al. [197] has found 16% reduction in the relative cell viability of MCF-7 cancer cells using 30 $\mu\text{g/ml}$ suspensions of Fe_2O_3 nanoparticles. In our case, 55% viability has been inhibited using 20 $\mu\text{g/ml}$ suspension of $\text{Ni}_x\text{Ce}_{1-x}\text{O}_2$ nanoparticles which is higher inhibition at low concentration. This higher selective cytotoxic behavior of the synthesized $\text{Ni}_x\text{Ce}_{1-x}\text{O}_2$ nanoparticles may be of high clinical interest because conventional anticancer drugs most of the time are not able to differentiate between the healthy and cancerous cells [198, 199]. The toxicity of nanomaterials depends on several factors likewise type and composition of the nanomaterials, particle size, shape and crystallinity, surface area and their level of solubility [112]. Previously, it has been reported that 20 nm CeO_2 nanoparticles induce elevated oxidative stress in human lung cancer cells via higher reactive oxygen species (ROS) production [66]. This elevated oxidative stress is suggested to the main cause of the reduction of cell viability. Moreover, differential cytotoxic nature of the CeO_2 nanoparticles is often associated with different intercellular pH values [112]. In order to confirm whether the differential cytotoxicity of the synthesized undoped and Ni doped CeO_2 nanoparticles have any correlation with ROS production or not, ROS generation study was performed and depicted in Fig. 5.9. It has been observed from Fig. 5.9 that undoped CeO_2 nanoparticles produced significantly higher amount of ROS in cancer cell line while no excessive ROS is generated in healthy cell line. Furthermore, systematic increase in ROS production in cancer cells is demonstrated with the increase in Ni doping concentration in CeO_2 host matrix. This enhancement in ROS production by CeO_2 nanoparticles with Ni doping level maybe associated with the V_o . Previously, it is reported that structural defects (V_o) in the crystal structure of Ni doped metal oxides nanostructures leads to enhanced level of ROS generation [200]. In our case, V_o are also found to be enhanced with Ni doping as depicted in Raman

spectroscopy results which may boost up the ROS generation. These prepared Ni doped CeO₂ with defective structure, narrow bandgap, high magnetic moment, high σ_{AC} , E' and with good Cytotoxicity are very useful for spintronics and cancer therapy.

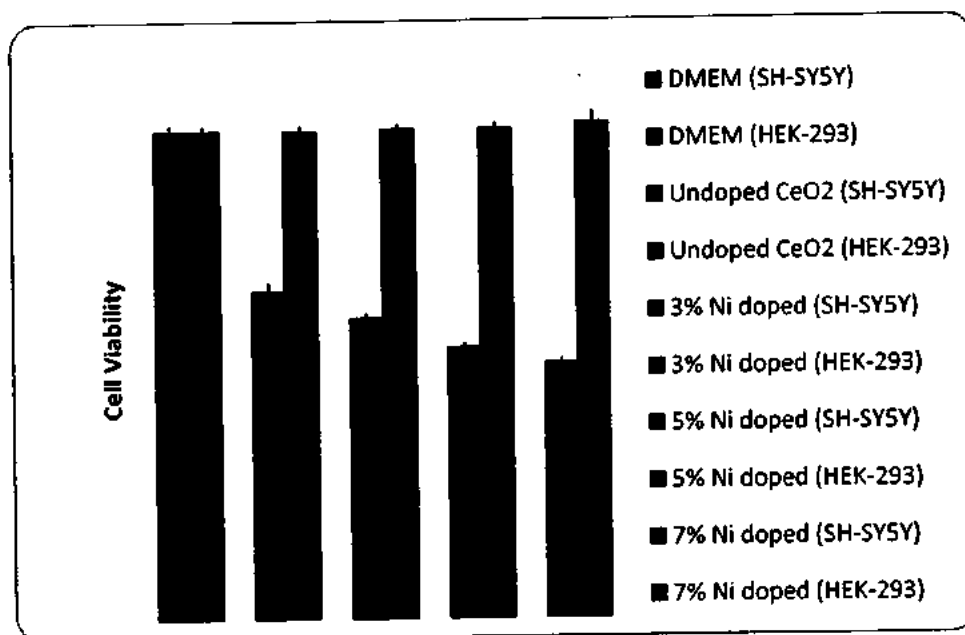


Figure 5.8: Effect of undoped & Ni doped CeO₂ nanoparticles on Neuroblastoma & HEK-293 Cells viability

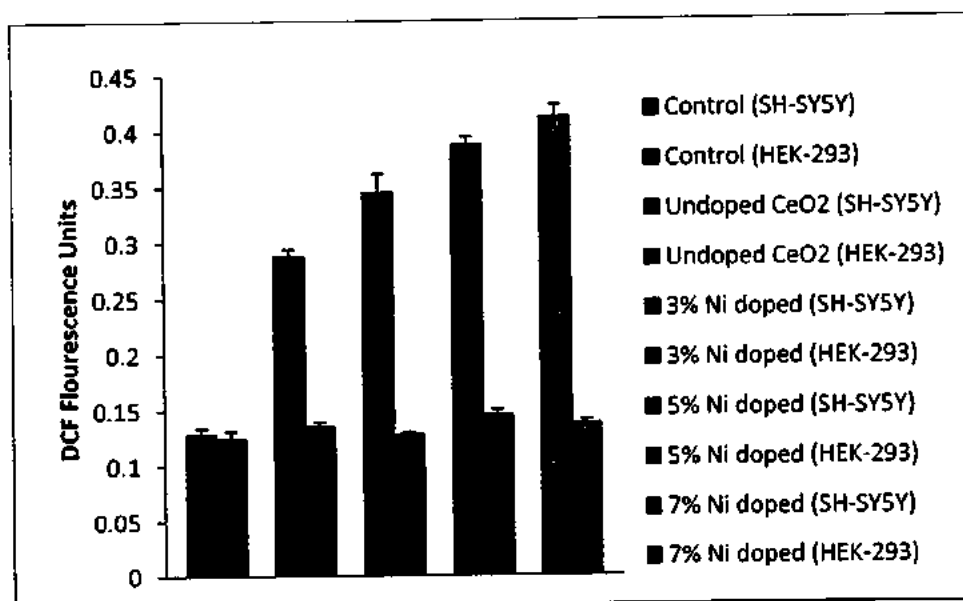


Figure 5.9: Reactive oxygen species (ROS) production in Neuroblastoma & HEK-293 Cells after incubation of undoped and Ni doped CeO₂ nanoparticles

Chapter No.6

Synthesis, Characterization and Anticancer Study of Mn Doped CeO₂ Nanoparticles

6.1 Introduction

Doping CeO₂ nanomaterials with different ionic states can be enhanced its catalytic activity remarkably because dopant can distort the lattice structure and create large number of structural defects such as V_o due to replacement of Ce⁴⁺ [201]. For instance, Fe doped CeO₂ nanoparticles have been reported to have greater photocatalytic activity as compared to undoped nanoparticles which is assigned to narrowing of band gap and larger surface area of doped nanoparticles [182]. Similarly, N. Sabari Arul et al have reported that the surface area and morphology play important role in the enhanced photocatalytic activity of Co doped CeO₂ nanorods [159]. Manganese (Mn) being one of the most common transition metal is considered to be the best dopant for CeO₂ because of its smaller ionic radii as compared to Ce ions [202]. Hence, Mn doped CeO₂ nanomaterial may solve the problems in the photocatalytic activity of CeO₂ based catalysts. In the literature, it has been reported that Mn dopant can cause the formation of large amount of defects in CeO₂ crystal structure which led to remarkably higher catalytic performance [203, 204]. It is well established fact that reactive oxygen species (ROS) play vital role in the inhibition of cancerous cells by metal oxides nanomaterials which in return depends on the defects states in the system [112, 121]. Hence, it is believed that Mn doping can lead to enhanced anticancer activity of CeO₂ nanoparticles. Till date no article is published on the anticancer activity of Mn doped CeO₂. Keeping this in view, Mn dopant induced effects on the ferromagnetic and cytotoxicity of the CeO₂ nanoparticles synthesized by facile chemical method has been studied.

6.2 Results and Discussions

6.2.1 Structural and morphological investigations

XRD characterization has been employed to investigate the phase purity and average crystallite sizes of the synthesized samples. As shown in Fig. 6.1(a), all the diffraction peaks in the XRD patterns of the synthesized samples can be well indexed to the single phase cubic fluorite structure of CeO_2 . The absence of impurity phases indicates that cubic fluorite structure is the only phase present in synthesized $\text{Mn}_x\text{Ce}_{1-x}\text{O}_2$ samples. Furthermore, the position of the main peak (111) has been shifted towards higher angles as shown in Fig. 6.1(b) which assure the successful doping of Mn ions in the CeO_2 crystal structure. It demonstrates the formation of homogeneous Ce-Mn-O solid solution [205]. This peak shift is associated with lattice contraction and distortion due the replacement of Ce^{4+} ions by smaller ionic radii trivalent Mn^{3+} ions [206]. The average crystallite sizes been calculated by Scherer formula (5.1). The calculated average crystallite size of undoped CeO_2 samples has been found to be 8 nm which is decreased down to 6 nm with Mn doping.

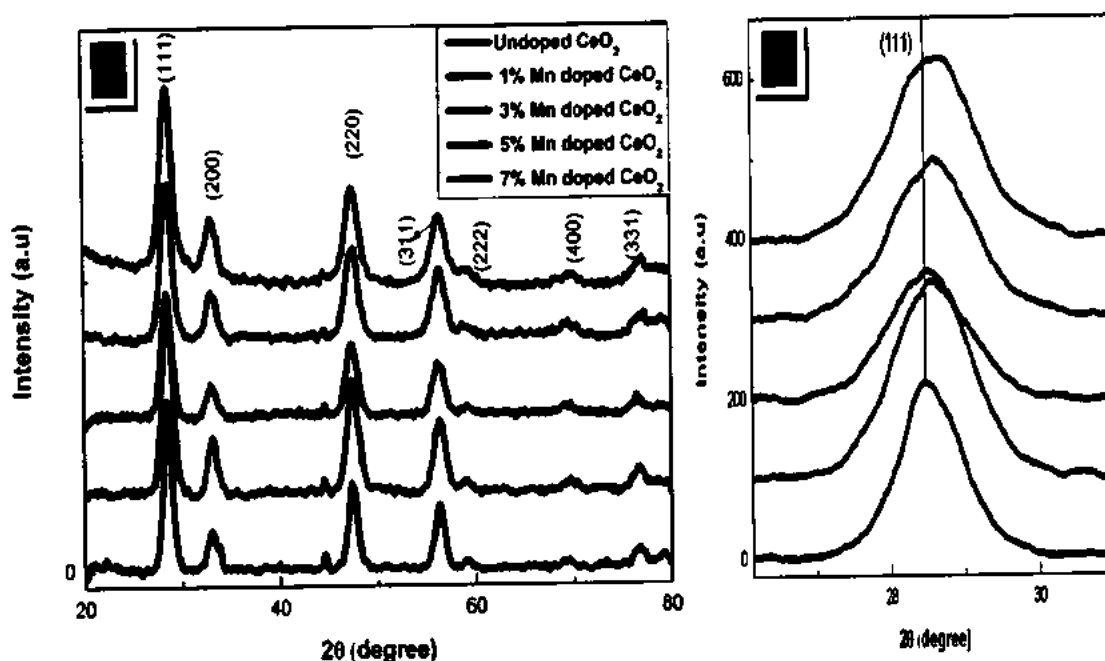


Figure 6.1: a) XRD patterns of the prepared samples and b) Shift in the (111) plane with Mn doping

SEM has been employed to obtain the surface morphology and grain sizes of the $Mn_xCe_{1-x}O_2$ nanoparticles. It can be seen from the SEM images of the synthesized samples that spherical nanoparticles have been formed both in all synthesized $Mn_xCe_{1-x}O_2$ samples. Furthermore, it has been observed that the nanoparticles are monodispersed and uniform with average particle size in the range of 30 to 41 nm as shown in Fig. 6.2 (a-d).

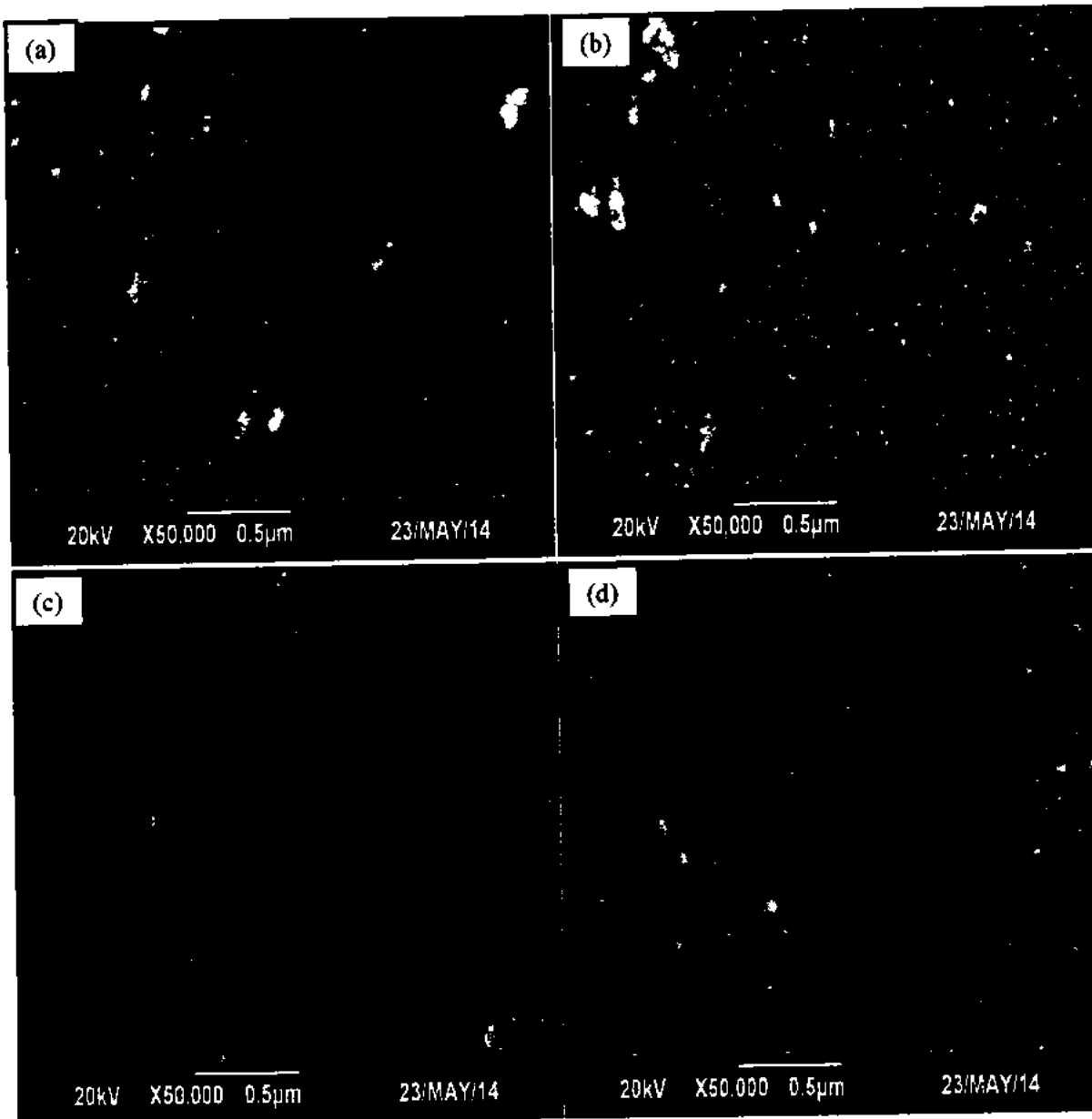


Figure 6.2: SEM images of (a) 1% (b) 3% (c) 5% and (d) 7% Mn doped CeO_2 nanoparticles

6.2.2 Analysis of surface area

The surface area is a crucial parameter for determination of the photocatalytic degradation capability of a catalyst. The SSA of the synthesized $Mn_xCe_{1-x}O_2$ monodisperse nanoparticles have been calculated using BET technique. Fig. 6.3 depicts the Mn dopant effects on the SSA of CeO_2 nanoparticles. A remarkable enhancement in the SSA of CeO_2 nanoparticles with Mn has been found which may be linked with crystallite size. It is well established phenomenon that SSA and crystallite size are inversely related to each other. It can be observed from table 6.1 that the crystallite size decreases systematically with Mn doping. Hence, the enhancement in SSA with the increase in Mn doping concentration may be attributed to the decrease in crystallite size. Previously, such kind of enhancement in SSA as a function of crystallite size has been reported for doped nanostructures as compared to undoped CeO_2 [182, 164]

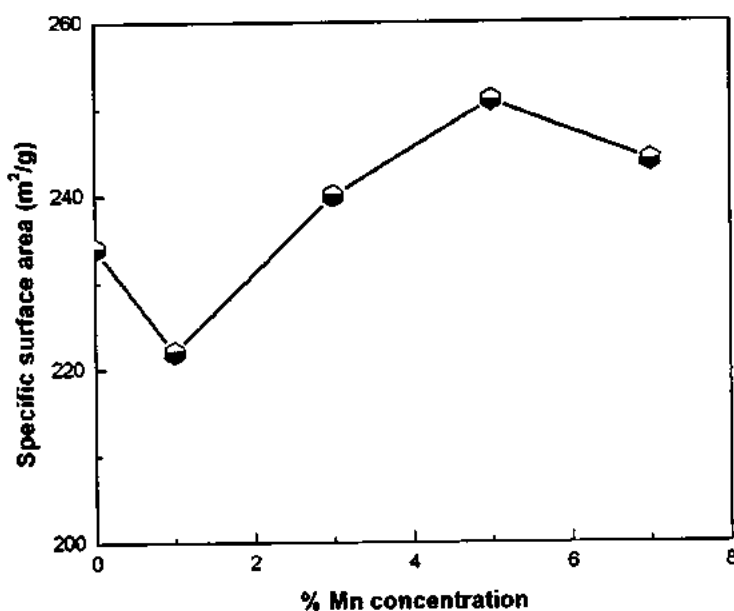


Figure 6.3: BET-SSA analysis of synthesized nanoparticles

6.2.3 Raman and optical characterizations

Raman spectroscopy has been used to further validate the phase purity of the synthesized samples. Raman spectroscopy is an effective technique to detect the possible

secondary phases which can easily flee from the detection limits of XRD. Furthermore it gives information about structural defects caused by the dopants which lead to the shift in Raman peaks. Fig. 6.4 depicts the Raman spectra of undoped and Mn doped CeO₂ synthesized samples. Well defined Raman band is observed at 445 cm⁻¹ which corresponds to the first order F_{2g} Raman active mode of the cubic fluorite structure of CeO₂. The observe Raman band has huge shift of 22 cm⁻¹ from the Raman active F_{2g} mode of bulk CeO₂ which may be attributed to the formation of V_o in crystal structure of nanocrystalline CeO₂ [73]. The only difference between the Raman spectra of undoped CeO₂ and that of Mn doped CeO₂ is the reduction in the peak intensity with doping. This reduction in peak intensity is often associated with the lattice defects (V_o) in the system which are often introduce when trivalent ions replace the tetravalent Ce ions in order to achieve the charge neutrality [74].

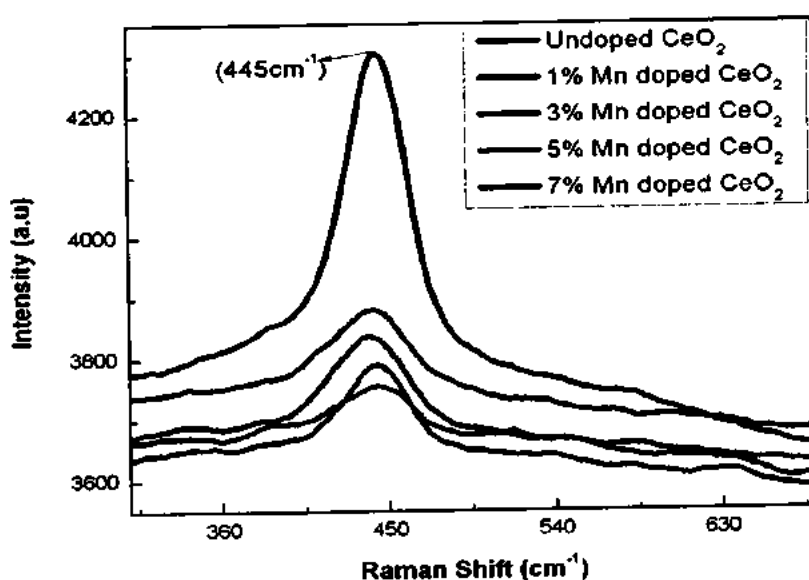


Figure 6.4: Raman spectra of the prepared nanoparticles

For Mn-O, Raman peaks appear in the range of 620-660 cm⁻¹ which are not present in the Raman spectra of Mn_xCe_{1-x}O₂ samples. This validates the XRD results about the formation of single phase cubic fluorite structure of CeO₂ for all samples. Moreover, Raman results hint the enhancement in V_o with Mn doping in CeO₂ which might potential for anticancer activity.

The exact knowledge about the optical absorption characteristics of nanomaterial is of utmost importance for their application in photocatalytic degradation of biomaterials. UV-visible absorption spectroscopy has been used to examine the optical properties of the synthesized nanoparticles. Fig. 6.5 shows the optical absorption spectra of $Mn_xCe_{1-x}O_2$ monodisperse nanoparticles in the wavelength range of 250 to 700 nm. The pristine CeO_2 monodisperse nanoparticles exhibit a typical band edge absorption peak at 312 nm. The optical band gap energies of the synthesized undoped and Mn doped CeO_2 monodisperse nanoparticles have been calculated by Tauc relation (3.2) as shown in the inset of Fig. 6.5.

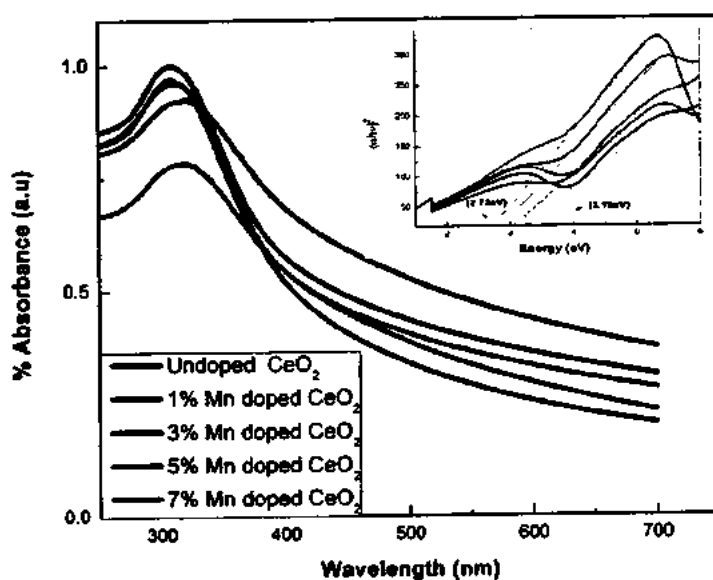


Figure 6.5: UV-visible absorption spectra of the undoped and Mn doped CeO_2 nanoparticles (Inset shows the bandgap estimation via Tauc relation)

The optical band gap energy calculated for undoped CeO_2 nanoparticles has been observed to be 3.19 eV which is systematically decreased down to 2.83 eV with the increase in Mn doping level. Such decrease in band gap energy of CeO_2 nanoparticles with Mn doping is previously reported by Xia et al [196]. They have suggested that it may be due to the formation of defects especially V_o and impurities caused by Mn doping. These V_o and impurities may form sublevel between the valance and conduction band of CeO_2 monodisperse nanoparticles which leads to narrowing of the band gap. Jie Tan et al; also

associated the narrowing of band gap of CeO₂ nanorods upon Mn doping with the creation defects and impurity states [207]. Hence, in our case the band gap reduction of CeO₂ nanoparticles with Mn doping may also be linked with formation of defects and impurity states below the conduction band originated by Mn doping. This tuned narrow band gap is potential for photo electronic nanodevices.

6.2.4 Dielectric properties

The dielectric properties of the synthesized undoped and Mn doped CeO₂ nanoparticles have been investigated by making their circular pellets and using the same method as mentioned in last chapters and then ϵ' , ϵ'' and σ_{AC} have been measured over a wide range of AC frequency (3 KHz- 5 MHz). The values of ϵ' , ϵ'' and σ_{AC} has been carefully calculated by relations (2.4) and (2.5).

Fig. 6.6 (a) depicts the variation of σ_{AC} of synthesized CeO₂ nanostructures as a function of AC frequency as well as Mn content. In all the samples, σ_{AC} is increasing with the increase in frequency, following power law, which indicates that the σ_{AC} is directly proportional to the AC frequency above a certain point. Moreover, by increasing Mn content, a definite increase in σ_{AC} of CeO₂ nanostructures is observed which may be linked with the fact that when Mn³⁺ ions replaces Ce⁴⁺ ions and give rise to more free electrons in the system which may increase the σ_{AC} of CeO₂ nanostructures. Moreover, with Mn doping, the defects (V_o) will be created in the host lattice in order to achieve charge neutrality, which in turn may lead to enhanced σ_{AC} .

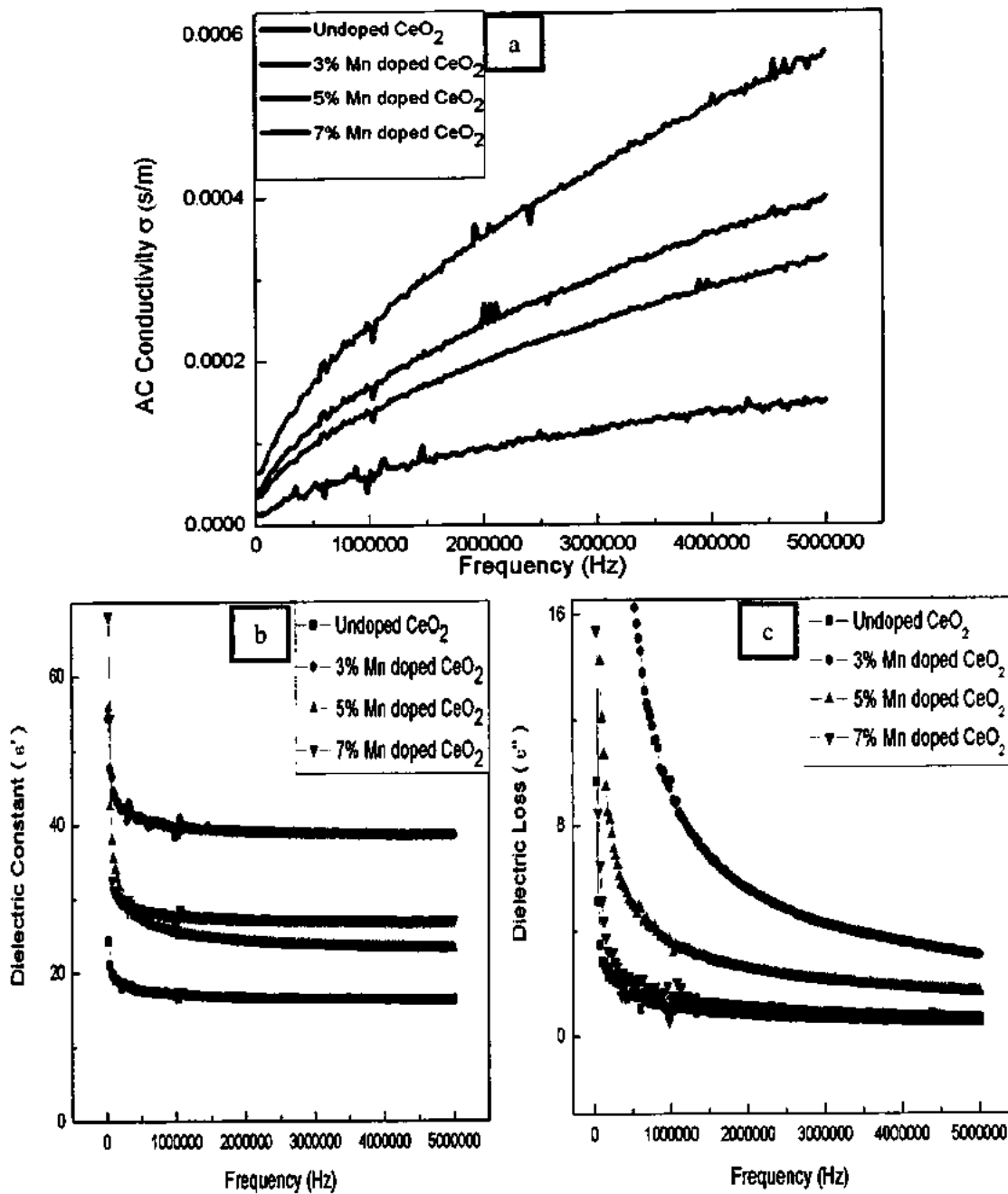


Figure 6.6: (a): Dielectric Constant (ϵ'), (b): Dielectric Loss (ϵ''), (c): AC conductivity (δ_{AC}), variation as a function of AC frequency

The Mn doping effect on the ϵ' for all the prepared samples is shown in Fig. 6.6 (b). There is a definite decrease in ϵ' with the increase in AC frequency and finally has a constant trend. This trend is due to existence of insulating grain boundaries around conducting grains. Charge carriers can easily penetrate through grains while cannot through grain boundaries so

ϵ' is high at low frequency due to large polarization effects [166]. Moreover, as TM ions owe higher ϵ' so its doping in host matrix increases its value as doping content increases [167].

Fig. 6.6 (c) depicts the variation of ϵ'' as a function of frequency as well doping content. There is a decrease in its value with frequency which may be linked to the fact that the exchange of electrons at grain boundaries extra amount of energy so ϵ'' is higher at lower frequency.

6.2.5 Magnetic study

The magnetization hysteresis (M-H) curves of the synthesized $\text{Mn}_x\text{Ce}_{1-x}\text{O}_2$ nanoparticles have been obtained at room temperature and illustrated in Fig. 6.7. It can be seen from the magnified M-H curves (shown in the inset of Fig. 6.7) that all the synthesized nanoparticles exhibit hysteresis loops which indicate the ferromagnetic behavior of the nanoparticles. The pristine CeO_2 nanoparticles exhibit weak magnetic moment as listed in table 6.1 which demonstrates their weak ferromagnetic behavior. However, Mn doping has enhanced the magnetic moment of CeO_2 nanoparticles remarkably as shown in table 6.1. The magnetic behavior of undoped CeO_2 nanoparticles has suggested to be attributed to the exchange interactions between the unpaired spins originated from surface defects (V_o) of nanoparticles [114]. The magnetic behavior of Mn doped CeO_2 nanoparticles may be explained on bound magnetic polarons (BMPs) model which suggests that the localized spins of Mn dopant ions with charge carriers which are bound to V_o [88, 207, 208]. These interactions lead magnetic polarization of surrounding moments. Now, in our case, Mn dopant can introduce V_o in the system in order to gain charge neutrality as the valance states of host and dopant are different from each other. These V_o will lead to development of BMPs and the exchange interactions of these BMPs with magnetic ions (In our case Mn) may lead RTFM in $\text{Mn}_x\text{Ce}_{1-x}\text{O}_2$ nanoparticles [115]. The increase in Mn doping level will lead to

increase amount of V_o and magnetic ions which results into enhancement in magnetic moment of the $Mn_xCe_{1-x}O_2$ nanoparticles

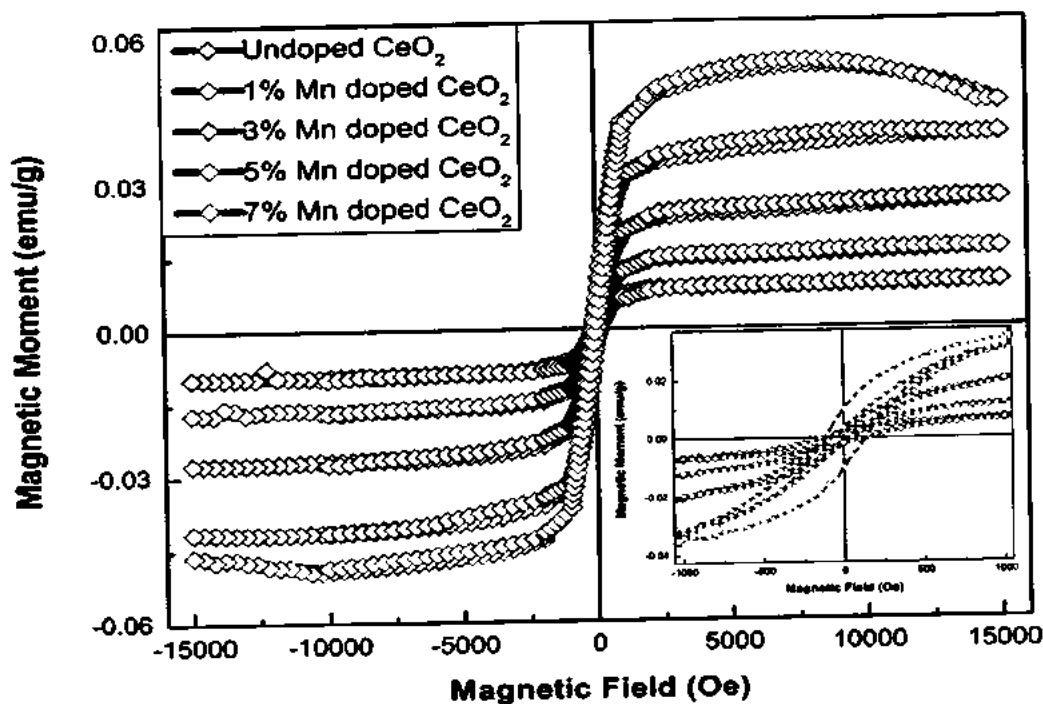


Figure 6.7: M-H loops of undoped

and Mn doped CeO_2 nanoparticles (Inset of the figure shows opened hysteresis loops)

6.2.6 Differential cytotoxicity analysis

It has been established in the previous discussions that Mn doping have shifted the band energy of the synthesized CeO_2 monodisperse nanoparticles towards visible region and also introduced RTFM. The band gap narrowing may be helpful in enhancing the photocatalytic inhibition of cancerous cells while RTFM behavior will lead targeted cancer therapy. Hence, Cytotoxicity of the synthesized $Mn_xCe_{1-x}O_2$ nanoparticles has been investigated against Neuroblastoma cancer cells & HEK-293 healthy cells via CCK-8 assay. Fig. 6.8 depict the relative cell viability of both type of cells after they are being treated for 24 hours with CeO_2 nanoparticles doped with different molar concentration of Mn i.e. 0, 1, 3, 5 and 7%. Controlled samples i.e. untreated samples are also provided for comparison. It has been observed from Fig. 6.8 that the prepared $Mn_xCe_{1-x}O_2$ nanoparticles have inhibited the

cancerous cell viability by almost 40 %. The synthesized nanoparticles have biosafe nature towards healthy cells except 7% Mn doped CeO₂ nanoparticles. This suggests the selective toxicity of the undoped, 1, 3, and 5% Mn doped CeO₂ nanoparticles while 7% Mn doped CeO₂ nanoparticles are found to be toxic for both healthy and cancerous cells.

The cytotoxicity of metal oxides nanoparticles is associated with several factors such as particle size, electrostatic interaction between nanoparticles and cells and reactive oxygen species (ROS) [191, 192]. The nanoparticles have very small sizes as compared to cells and they can penetrate the cell wall and cause cell damage. Furthermore, it has been reported that CeO₂ nanoparticles having particle size less than 20 nm remains in cells for longer time as compared to bigger particles which lead to harmful effects on cells [113]. Secondly, several types of ROS such as hydroxyl radicals, singlet oxygen and H₂O₂ etc. can be generated on the surface of nanoparticles by light induced effects [121]. The enhanced ROS generation can lead to cell death via different mechanisms such as lipid peroxidation, apoptosis and cell membrane damage [112, 113]. Different types of cells respond differently to CeO₂ nanoparticles and lead to different levels of ROS generation [113]. The pH value plays vital role in defining the CeO₂ nanoparticles toxicity. Basic pH environment leads cyto-protective effects while acid environment promotes cytotoxic effects [112]. As healthy cells and cancerous cells provide basic and acidic atmosphere respectively, therefore the synthesized undoped and Mn doped CeO₂ nanoparticles may generate different level of ROS and have differential cytotoxicity.

In order to confirm that the selectivity toxicity of the synthesized nanoparticles is due to differential level of ROS generation, we have investigated the ROS generation by the synthesized nanoparticles in the presence of healthy cells and cancerous cells. Fig. 6.9 shows the level of ROS generation in both healthy cells and cancerous cells. It has been observed that ROS generation and cell damage are closely related to each other. Hence, the differential

cytotoxicity of undoped Mn doped CeO₂ nanoparticles up to 5% doping and overall cytotoxicity of 7% Mn doped CeO₂ nanoparticles may be attributed to different levels of ROS generation. Previously, it is reported in the literature that structural defects (V_o) in the crystal structure of TM doped metal oxides nanostructures leads to greater level of ROS generation [201]. In this case, V_o are also found to be enhanced with Mn doping as depicted in Raman spectroscopy results which may boost up the ROS generation. This argument is still debatable as previously seen in Chapters No. 3 and 4, we have observed similar relation between V_o and level of ROS production for Fe and Ni doped CeO₂ nanostructures but no such a correlation has been found in case of Co and Mn doped CeO₂ nanoparticles in Chapter No. 5 and 6 respectively. Hence, more work is needed to be done in this regard.

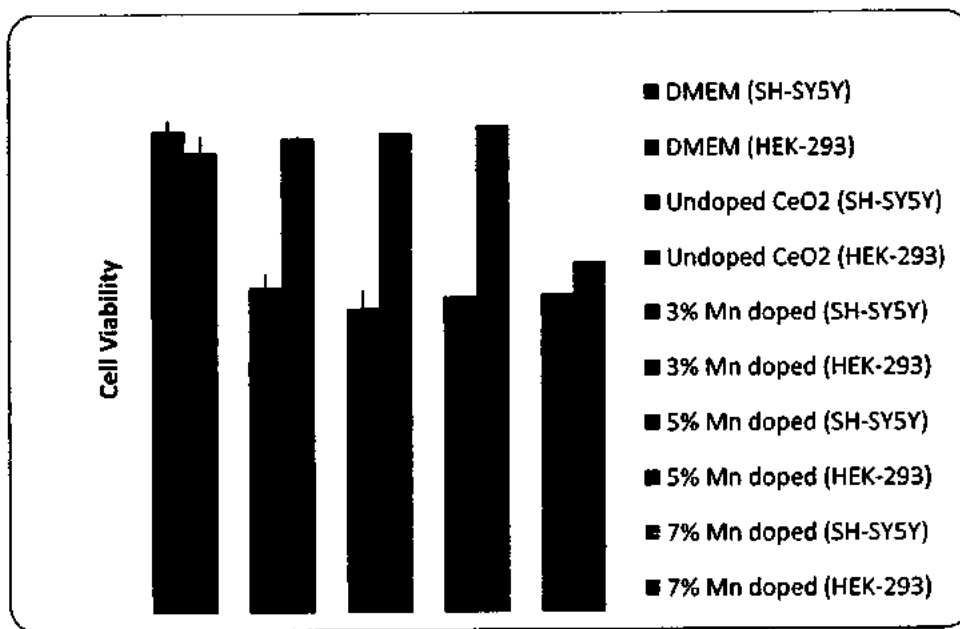


Figure 6.8: Effect of undoped & Mn doped CeO₂ nanoparticles on Neuroblastoma & HEK-293 Cells Viability

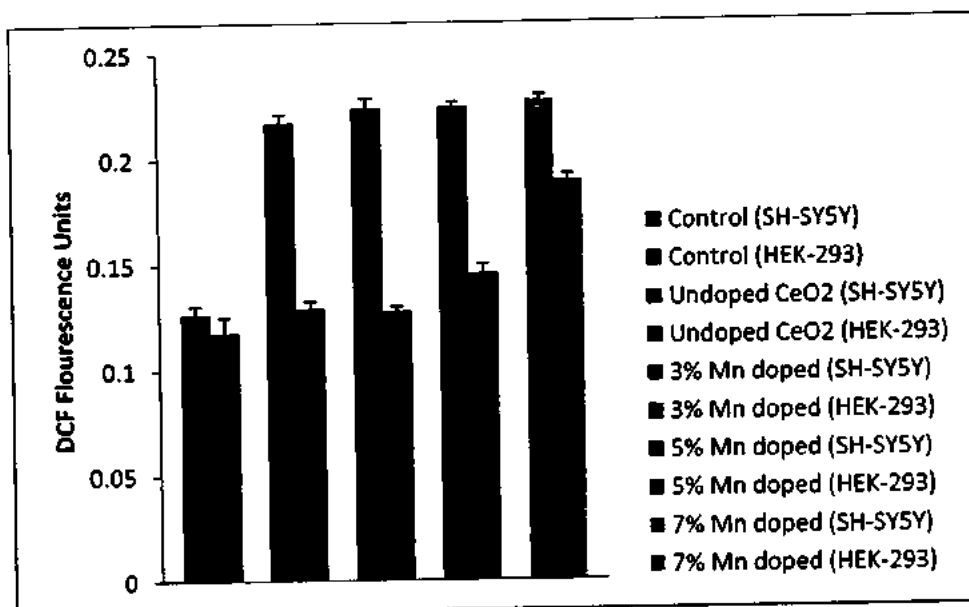


Figure 6.9: ROS production in Neuroblastoma & HEK-293 Cells after incubation of undoped and Mn doped CeO₂ nanoparticles

Table 6.1: Tabulated overview of physical properties of thesis work.

Sample	Crystallite size (nm)	Average Particle Size (nm)	Lattice Const. (nm)	Band Gap Energy (eV)	M_s (emu/g)	ϵ'			ϵ''			δ_{AC} (s/m)* 10^{-5}			Healthy Cells viability (% age)	Cancer Cells viability (% age)	
						1MHz	2MHz	4MHz	1MHz	2MHz	4MHz	1MHz	2MHz	4MHz			
$\text{Co}_{1-x}\text{O}_2$	0%	8	20	0.5421	3.19	0.0083	17	16.6	16.4	1.2	0.83	0.59	6.1	9.31	13.3	100	71
	3%	5.3	11	0.5410	3.18	0.056	26	22.2	20.3	1.4	1.11	0.83	9.2	12.3	18.2	100	63
	5%	4.5	13	0.5403	2.90	0.07	25	24.2	23.4	1.7	2.55	1.86	19.5	28.5	41.7	100	69
	7%	4.5	13	0.5390	2.85	0.97	27	27.2	27.1	7.8	5.44	3.58	51.2	61.9	80.1	71	69
$\text{Fe}_{1-x}\text{O}_2$	3%	7	30	0.5403	2.8	0.0066	31	30	29	3.1	2.5	1.98	19	28	41	100	62
	5%	6	22	0.5390	2.5	0.0084	31.2	31	30	2.8	1.7	1.54	24	35	51	100	56
	7%	4	22	0.5243	2.6	0.0126	31	32	32	3.1	2.5	1.97	26	38	57	98	53
$\text{Ni}_{1-x}\text{O}_2$	3%	6	24	0.5408	3.02	0.0213	29	24	22	3.2	5.1	5.6	12	19	28	100	63
	5%	6	28	0.5402	2.86	0.0284	22	19	17	3.7	6.4	5	16	22	32	100	53
	7%	5	22	0.5394	2.72	0.0357	25	25	25	8.1	7.1	5.3	24	36	51	100	50
$\text{Mn}_{1-x}\text{O}_2$	3%	6	21	0.5419	3.04	0.026	27	26.8	27	1.3	1.2	1.2	24	35	50	100	66
	5%	6	28	0.5390	2.91	0.039	25	24	23	2.1	2.0	2.0	17	25	35	100	68
	7%	5.5	41	0.5392	2.83	0.045	39.3	39	38	6.1	6.0	5.9	13	20	29	70	68

Conclusions

In conclusions, ultrafine and homogeneously distributed spherical CeO₂ nanoparticles have been synthesized by a facile chemical co-precipitation technique. The synthesized nanoparticles have exhibited cubic fluorite structure with lattice constant of 0.5421 nm and optical band gap energy of 3.19 eV. Interestingly, these nanoparticles have shown ferromagnetic behavior which is attributed to defects in the crystal structure of CeO₂. In order to tailor the structural, optical, dielectric and magnetic properties of prepared nanoparticles, TM ions (i.e. Co, Fe, Ni and Mn) have been doped in the host matrix of CeO₂.

The structural properties of CeO₂ nanoparticles investigated through XRD have been observed to be greatly influenced by TM ions doping. A peak shift in the main diffraction peak towards higher angles has been observed for each TM dopants. The average crystallite size and lattice constant values have also been found to decrease systematically with the increase in TM dopants concentration. These variations in the structural properties of CeO₂ nanoparticles upon doping as well as absence of secondary phases in the XRD patterns depict the successful substitution of all TM ions on sites of host cations.

Morphology and particle sizes of the synthesized undoped and doped nanoparticles have been analyzed via SEM. SEM micrographs have shown formation of spherical nanoparticles for all samples. Shape of the particles has not been affected by the introduction of dopants in the host lattice. However, average particle size has been found to decrease from 28 nm down to 22 nm with Co, Ni and Fe doping while Mn doping has increased it up to 41 nm due to difference of ionic charge as well as ferromagnetic nature of dopants.

Raman spectroscopy has been used to detect the existence of any secondary phases which may flee from the detection limit of XRD as well as the defects chemistry of the synthesized nanoparticles. Raman results corroborated well with XRD results and confirm the

formation of single phase cubic fluorite structure for undoped and TM doped CeO₂ nanoparticles. Raman spectra of undoped CeO₂ has exhibited a prominent peak at 445 cm⁻¹ which is characteristic F_{2g} peak of cubic fluorite structure of CeO₂. This peak has huge down shift of 18 cm⁻¹ counter to bulk which may be attributed to small particle size and presence of defects in the crystal structure of CeO₂. TM doping has resulted in shift towards lower wavenumbers overall and also lead to suppression and broadening of this peak. This behavior depicts the enhancement in structural defects in host lattice upon doping such as V_o which have been observed to vital for controlling the physical properties especially magnetic behavior and cytotoxicity of CeO₂ nanoparticles.

Optical properties of CeO₂ nanoparticles have been also significantly influenced by TM doping level. It is concluded that band gap energy of CeO₂ nanoparticles can be greatly tuned via TM doping. All the four different TM dopants have led to the narrowing of the optical band gap of CeO₂ nanoparticles which has been assigned to several factors such as V_o, formation of impurities level between the conduction and valence band and variation in structural parameters. Ni dopant has been observed to be most effective in narrowing the band gap of CeO₂ nanoparticles. It has decreased the optical band gap energy of CeO₂ nanoparticles by 0.47 eV which make it potential for visible light activated photoelectronic nanodevices.

TM doping has been found to tailor the dielectric characteristics of CeO₂ nanoparticles. Overall, ϵ' , ϵ'' and δ_{AC} of CeO₂ nanoparticles have been observed to increase significantly with TM doping concentration. σ_{AC} of CeO₂ nanoparticles has been increased more by Co dopant as compared to other dopants. However, Ni dopant has increased the ϵ' and ϵ'' CeO₂ nanoparticles more efficiently comparing to Fe, Co and Mn dopants which make CeO₂ potential for spintronics nanodevices.

All the synthesized nanoparticles have exhibited ferromagnetic behaviour. TM dopants have significantly influenced the magnetic properties of CeO₂ nanoparticles. The M_s value of CeO₂ nanoparticles has been found to increase with the increase in TM doping level. Co doping has been observed to be more effective in enhancing the M_s values of CeO₂ nanoparticles. It has increased its value from 0.0066 emu/g to 0.97 emu/g. This enhancement in magnetic properties of CeO₂ nanoparticles with TM doping level is assigned to V_o and TM ions concentration. This ferromagnetic behavior and tuned optical band gap of the synthesized nanoparticle at room temperature makes potential for spintronics and biological applications.

Finally, the synthesized nanoparticles have been found to have differential cytotoxic nature. They are observed to be toxic towards cancerous cells while nontoxic towards healthy cells at nanoparticles concentration of 20 µg/ml. Co and Mn dopants are not so much effective in enhancing the cytotoxicity of CeO₂ nanoparticles. While Ni and Fe dopants have remarkably increased the cytotoxicity of CeO₂ nanoparticles towards SH-SY5Y cancer cells while having biosafe nature towards healthy cells. This enhancement has been observed to be strongly correlated with the level of ROS produced by the synthesized nanoparticles.

The above findings in this thesis work show that TM doping has tailored the physical properties of CeO₂ nanoparticles which make it highly potential in spintronics, visible light activated optoelectronics devices and targeted nano therapeutic.

References

- [1] D. Schubert, R. Dargusch, J. Raitano, S.W. Chan, *Biochemical and Biophysical Research Communications*, 31, (2006) 86-91.
- [2] B.H. Davis, S.N. Russell, P.J. Reucroft, R.B. Shalvoy, *J. Chem. Soc. Faraday Trans.*, I 76, (1980) 1917-1922.
- [3] K. Tanabe, M. Misono, Y. Ono, H. Hattori, *New Acids and Bases*, Kodansha, Tokyo; Elsevier, Amsterdam-Oxford-New York-Tokyo, 51, (1989) 41-47.
- [4] E.M. Kennedy, N.W. Cant, *Appl. Catal.*, 75, (1991) 321-330.
- [5] S. Sato, R. Takahashi, T. Sodesawa, N. Yamamoto, *Catal. Commun.*, 5, (2004) 397-400.
- [6] A. Igarashi, N. Ichikawa, S. Sato, R. Takahashi, T. Sodesawa, *Appl. Catal. A*, 300, (2006) 50-57.
- [7] M. Kobune, S. Sato, R. Takahashi, *J. Mol. Catal. A*, 279, (2008) 10-19.
- [8] M. Matsuzawa, *J. Appl. Phys.*, 74, (1994) 111-115.
- [9] X. Ni, Y. Wang, F. Guo, P. Yao, M. Pan, *Journal of Rare Earths*, 30, (2012) 437-441.
- [10] A.L. Gal, S. Abanades, *The Journal of Physical Chemistry C*, 116, (2012) 13516-13523.
- [11] J.M. Coronado, A.J. Maira, A. Martinez-Arias, J.C. Conesa, J. Soria, *Journal of Photochemistry and Photobiology A: Chemistry*, 150, (2002), 213-221.
- [12] B. Brabu, S. Haribabu, M. Revathy, S. Anitha, M. Thangapandiyan, K.R. Navaneethakrishnan, C. Gopalakrishnan, S.S. Murugan, T.S. Kumaravel, *Toxicology Research*, 4, (2015) 1037-44.

- [13] M. Ghiasi, A. Malekzadeh, *Superlattices and Microstructures*, 77, (2015) 295-304.
- [14] K.C. Taylor. J.R. Anderson, M. Boudart (Eds.), *Catalysis, Science and Technology*, Springer-Verlag, Berlin, 5, (1984)120-123.
- [15] S. Damyanova, B. Pawelec, K. Arishtirova, M.M. Huerta, J.L. Fierro, *Applied Catalysis A: General*, 15, (2008) 86-96.
- [16] H. Yahiro, K. Eguchi, H. Arai, *Solid State Ionics*, 31, (1989) 71-75.
- [17] E. Aneggi, M. Boaro, C. Leitenburg, G. Dolcetti, A. Trovarelli , *Journal of Alloys and Compounds* 408, (2006) 1096-1102.
- [18] J.A. Borm, D. Paul, S. Robbins, T. Haubold, H. Kuhlbusch, K. Fissan, R. Donaldson, *Particle and fiber toxicology*, 1, (2006) 11.
- [19] T. Mori, J. Drennan, Y. Wang, J.G. Li, T. Ikegami, *Journal of Thermal Analysis and Calorimetry*, 1, (2002) 309-19.
- [20] C. Suryanarayana, *International Materials Reviews*, 40, (1995) 41-64.
- [21] T. Chikyow, S.M. Bedair, L. Tye, N.A. El-Masry, *Applied physics letters*, 22, (1994) 1030-32.
- [22] C. Sun, H. Li, L. Chen, *Energy and Environmental Science*, 5, (2012) 8475-8505.
- [23] A.I. Tok, F.Y.C. Boey, Z. Dong, X.L. Sun, *Journal of materials processing technology*, 190, (2007) 217-222.
- [24] V.K. Ivanov, O.S. Polezhaeva, G.P. Kopitsa, A.E. Baranchikov, Y.D. Tretyakov, *Inorganic Materials*, 44, (2008) 272-277.
- [25] D. Waller, J.A. Lane, J.A. Kilner, B.C.H. Steele, *Solid State Ionics*, 86, (1996) 767-772.
- [26] T.S. Stefanik, H.L. Tuller, *Journal of European Ceramic Society*, 21, (2001) 1967-1970.
- [27] A. Tsoga, A. Gupta, A. Naoumidis, P. Nikolopoulos, *ActaMaterialia*, 48, (2000) 4709-4714.
- [28] X. Yu, P.B. Xie, Q.D. Su, *J. Phys. Chem.*, 3, (2001) 5266-5271.

- [29] L. Qian, J. Zhu, W. Du, X. Qian, *Materials Chemistry and Physics*, 115, (2009) 835-849.
- [30] C.H. Hu, C.H. Xia, F. Wang, M. Zhous, P.F. Yin, X.Y. Han, *Bulletin of Materials Science*, 34, (2012) 1033-1037.
- [31] X.D. Feng, D.C. Sayle, Z.L. Wang, M.S. Paras, B. Santora, A.C. Sutorik, T.X.T. Sayle, Y. Yang, Y. Ding, X.D. Wang, Y.S. Her, *Science*, 312, (2006) 1504-1508.
- [32] T. Masui, K. Fujiwara, K. Machida, G. Adachi, T. Sakata, H. Mori, *Chemistry of Materials*, 9, (1997) 2197-2204.
- [33] N. Imanaka, T. Masui, H. Hirai, G. Adachi, *Chemistry of materials*, 15, (2003) 2289-2291.
- [34] S. Bernal, J.J. Calvino, M.A. Cauqui, J.M. Gatica, C. Larese, J.A.P. Omil, J.M. Pintado, *Catalysis Today*, 50, (1999) 175-206.
- [35] T.S. Zhang, J. Ma, H.T. Huang, P. Hing, Z.T. Xia, S.H. Chan, J.A. Kilner, *Solid state sciences*, 5, (2003) 1505-1511.
- [36] M. Mogensen, N.M. Sammes, G.A. Tompsett, *Solid State Ionics*, 129, (2000) 63-94.
- [37] X.H. Liao, J.M. Zhu, J.J. Zhu, J.Z. Xu, H.Y. Chen, *Chemical Communication.*, 10, (2001) 937-938.
- [38] P. Patnaik, *Handbook of Inorganic Chemicals*, McGraw-Hill, 2002, ISBN 0-07-49439-8.
- [39] A. Trovarelli, *Catalysis Reviews*, 38, (1996) 439-520.
- [40] H. Matzke, Academic Press Inc., London, (1981) 155-232.
- [41] T.X.T. Sayle, S.C. Parker, C.R.A. Catlow, *Surface Science*, 316, (1994) 329-336.
- [42] J.C. Conesa, *Surface Science*, 339, (1995) 337-352.
- [43] K. Zhou, X. Wang, X. Sun, Q. Peng, Y. Li, *Journal of Catalysis*, 229, (2005) 206-212.
- [44] H.X. Mai, L.D. Sun, Y.W. Zhang, R. Si, W. Feng, H.P. Zhang, H.C. Liu, C.H. Yan, *The Journal of Physical Chemistry B*, 109, (2005) 24380-24385.

- [45] K.S. Lin, S. Chowdhury, *International journal of molecular sciences*, 11, (2010) 3226-3251.
- [46] R.J. Aitken, M.Q. Chaudhry, A.B.A. Boxall, M. Hull, *Occupational Medicine*, 56, (2006) 300-306.
- [47] Y. Ju-Nam, J.R. Lead, *Science of the Total Environment*, 400, (2008) 396-414.
- [48] E. Navarro, A. Baun, R. Behra, N.B Hartmann, J. Filser, A.J. Miao, A. Quigg, P.H. Santschi, L. Sigg, *Ecotoxicology*, 17, (2008) 372-386.
- [49] H. Zhang, B. Gilbert, F. Huang, J.F. Banfield, *Nature*, 424, (2003) 1025-1029.
- [50] R.H. Kodama, *J. Magn. Magn. Mater.*, 200, (1999)359-372.
- [51] B. Issa, I.M. Obaidat, B.A. Albiss, Y. Haik, *Int. J. Mol. Sci.*, 14, (2013) 21266-21305.
- [52] T. Hansen, G. Clermont, A. Alves, R. Eloy, C. Brochhausen, J.P. Boutrand, A.M. Gatti, C.J. Kirkpatrick, *Journal of the Royal Society Interface*, 11, (2006) 767-775.
- [53] I.L. Hsiao, Y.J. Huang, *Science of the Total Environment*, 409, (2011) 1219-1228.
- [54] S.N. Wigginton, K.L. Haus, M.F. Hochella Jr, *Journal of Environmental Monitoring*, 9, (2007) 1306-1316.
- [55] T. Takagahara, K. Takeda, *Phys. Rev. B Condense Matter*, 46, (1992) 15578-15581.
- [56] X. Zhao, C.M. Wei, L. Yang, M.Y. Chou, *Physical review letters*, 92, (2004) 236805.
- [57] A.D. Yoffe, *Advances in Physics*, 42, (1993) 173-262.
- [58] D.A.B. Miller, D.S. Chemla, T.C. Damen, A.C. Gossard, W. Wiegmann, T.H. Wood, C.A. Burrus, *Phys. Rev. Lett.*, 53, (1984) 2173.
- [59] S. Gnanam, V. Rajendran, *Journal of Nanoparticles*, 2013, (2013) 1155-60.
- [60] Z. Wang, Z. Quan, J. Lin, *Inorganic chemistry*, 46, (2007) 5237-5242.
- [61] R. Murugan, G. Vijayaprasath, T. Mahalingam, G. Ravi, *Materials Letters*, 162, (2016) 71-74.
- [62] L. Yue, X.M. Zhang, *Journal of Alloys and Compounds*, 475, (2009), 702-705.

- [63] T. Dhannia, S. Jayalekshmi, M.S. Kumar, T.P. Rao, A.C. Bose, *Journal of Physics and Chemistry of Solids*, 71, (2010) 1020-1025.
- [64] T. Suzuki, I. Kosacki, H.U. Anderson, *Solid State Ionics*, 151, (2002) 111-121.
- [65] A.S. Karakoti, N.A.M. Riviere, R. Aggarwal, J.P. Davis, R.J. Narayan, W.T. Self, J. McGinnis, S. Seal, *Journal of Medicine*, 60, (2008) 33-37.
- [66] W. Lin, Y.W. Huang, X.D. Zhou, Y. Ma, *International journal of toxicology*, 25, (2006) 451-457.
- [67] K. Nakamoto, *Infrared and Raman Spectra of Inorganic and Coordination Compounds*; 5th; John Wiley & Sons: New York, 1997.
- [68] W. Weber, K. Hass, J. McBride, *Phys. Rev. B*, 48, (1993) 178-185.
- [69] V.V. Pushkarev, V.I. Kovalchuk, J.L. d'Itri, *Phys. Chem. B*, 108, (2004) 5341-5348.
- [70] S. Colis, A. Bouaine, G. Schmerber, C. Ulhaq-Bouillet, A. Dinia, S. Choua, P. Turek, *Phys. Chem. Chem. Phys.* 14, (2012) 7256-7263.
- [71] V.D. Araujo, W. Avansi, H.B. de Carvalho, M.L. Moreira, E. Longo, C. Ribeiro, M.I.B. Bernardi, *Cryst. Eng. Comm.*, 14, (2012) 1150-1154.
- [72] C. Chappert, A. Fert, F.N.V. Dau, *Nature materials*, 6, (2007) 813-823.
- [73] T. Bland, K. Lee, S. Steinmuller, *Physics World*, 21, (2008) 24-28.
- [74] S.A. Wolf, D.D. Awschalom, R.A. Buhrman, J.M. Daughton, S.V. Molnar, M.L. Roukes, A.Y. Chtchelkanova, D.M. Treger, *Science*, 294, (2001) 1488-1495.
- [75] R. Janisch, P. Gopal, N.A. Spalding, *Journal of Physics: Condensed Matter*, 17, (2005) 657.
- [76] D. Ferrand, J. Cibert, A. Wasiela, C. Bourgonon, S. Tatarenko, G. Fishman, T. Andrearczyk, J. Jaroszynski, S. Kolesnik, T. Dietl, B. Barbara, D. Dufeu, *Physical Review B*, 63, (2001) 085201.

- [77] K.W. Edmonds, K.Y. Wang, R.P. Champion, A.C. Neumann, N.R.S. Farley, B.L. Gallagher, C.T. Foxon, *Appl. Phys. Lett.*, 81, (2002) 4991.
- [78] D. Chiba, K. Takamura, F. Matsukura, H. Ohno, *Applied Physics Letters*, 82, (2003) 3020.
- [79] Y.J. Matsumoto, M. Murakami, T.J. Shono, T. Hasegawa, T. Fukumura, M. Kawasaki, P. Ahmet, T. Chikyow, S.Y. Koshihara, H. Koinuma, *Science*, 291, (2001) 854-856.
- [80] Y. Matsumoto, R. Takahashi, M. Murakami, T. Koida, X.J. Fan, T. Hasegawa, T. Fukumura, M. Kawasaki, S.Y. Koshihara, H. Koinuma, *Japanese Journal of Applied Physics*, 40, (2001) 1204.
- [81] K. Ueda, H. Tabata, T. Kawai, *Applied Physics Letters*, 79, (2001) 988.
- [82] S.B. Ogale, R.J. Choudhary, J.P. Buban, S.E. Lofland, S.R. Shinde, S.N. Kale, V.N. Kulkarni, J. Higgins, C. Lanci, J.R. Simpson, N.D. Browning, S.D. Sarma, H.D. Drew, R.L. Greene, T. Venkatesan, *Physical Review Letters*, 91, (2003) 077205.
- [83] S.N. Kale, S.B. Ogale, S.R. Shinde, M. Sahasrabudhe, V.N. Kulkarni, R.L. Greene, T. Venkatesan, *Appl. Phys. Lett.*, 82, (2003) 2100.
- [84] J. Philip, N. Theodoropolou, G. Berera, J.S. Moodera, B. Satpati, *Applied Physics Letters*, 85, (2004) 777-779.
- [85] J. Sacanell, M.A. Paulin, V. Ferrari, G. Garbarino, A.G. Leyva, *Applied Physics Letters*, 100, (2012) 172405.
- [86] S. Phokha, S. Pinitsoontorn, S.i Maensiri, *JOURNAL OF APPLIED PHYSICS* 112, (2012) 113904.
- [87] S. Phokha, S. Pinitsoontorn, S. Maensiri, *Nano-Micro Lett.*, 5, (2013) 223-233.
- [88] J.M.D. Coey, M. Venkatesan, C.B. Fitzgerald, *Nature Materials*, 4, (2005) 173-179.
- [89] M.J. Calderon, S.D. Sarma, *Annals of Physics*, 322, (2007) 2618-2634.

- [90] P.R. Keating, D.O. Scanlon, G.W. Watson, *Journal of Physics: Condensed Matter.*, 14, (2009) 405502.
- [91] H. Toyosaki, T. Fukumura, Y. Yamada, K. Nakajima, T. Chikyow, T. Hasegawa, H. Koinuma, M. Kawasaki, *Nature Materials*, 3, (2004) 221-224.
- [92] L.R. Shah, B. Ali, H. Zhu, W.G. Wang, Y.Q. Song, H.W. Zhang, S.I. Shah, J.Q. Xiao, *Journal of Physics: Condensed Matter.*, 21, (2009) 486004.
- [93] S.G. Penn, L. He, M. Natan, *J. Nanoparticles for bio analysis Curr. Opin. Chem. Biol.*, 7, (2003) 609-615.
- [94] O. Yamamoto, *Int. J. Inorg. Mater.*, 3, (2001) 643.
- [95] G. Oberdorster, E. Oberdorster, J. Oberdorster, *Nanotoxicology, Environ. Health Perspect.*, 113, (2005) 823-839.
- [96] A.Y. Chow, *Nature Education*, 3, (2010) 7-12.
- [97] G.S. Dite, A.S. Whittemore, J.A. Knight, E.M. John, R.L. Milne, I.L. Andrulis, M.S. Southey, M. MRE, G.G. Giles, A. Miron, A.L. Phipps, D.W. West, J.L. Hopper, *British journal of cancer*, 103, (2010) 1103-1108.
- [98] L.M. Wagner, M.K. Danks, *J. Cell Biochem*, 107, (2009) 46-57.
- [99] T.A. Ishola, D.H. Chung, *SurgOnco*, 116, (2007) 149-156.
- [100] W.L. Hobbie, *Pediatric Blood & Cancer*, 51, (2008) 679-683.
- [101] B.H. Kushner, K. Kramer, M. PLaQuaglia, S. Modak, K. Yataghene, N.V. Cheung, *J. Clin. Oncol*, 22, (2004) 4888-4892.
- [102] R. Seigneuric, L. Markey, D.S.A. Nuyten, C. Dubernet, C.T.A. Evelo, E. Finot, C. Garrido, *Curr. Mol. Med.*, 10, (2010) 640-652.
- [103] Z. Liu, F. Kiessling, J. Gatzjens, *Journal of Nanomaterials*, 2010, (2010) 894303.
- [104] R. Hao, R. Xing, Z. Xu, Y. Hou, S. Gao, S. Sun, *Advanced Materials*, 22, (2010) 2729-2742.

- [105] Y. Jing, H.D. Yan, M.Z. Yousaf, H.Y. Long, G. Song, *Chin. Phys. B*, 22, (2013) 027506.
- [106] M. Ahamed, A. Hisham, M.A. Alhadlaq, M. Khan, M. J.Akhtar, *Journal of nanoparticle research*, 15, (2013) 1-11.
- [107] S. Alarifi, D. Ali, S.Akhtani, M. S. Alhader, *Biological trace element research*, 159, (2014) 416-424.
- [108] X. Meng, H.C. Seton, L.T. Lu, I.A. Prior, N.T.K. Thanh, B. Song, *Nanoscale*, 3, (2011) 977-984.
- [109] J.E. Kim, J.Y. Shi, M.H. Cho, *Archives of toxicology*, 86, (2012) 685-700.
- [110] U.O. Hafelli, J.S. Riffle, L.H. Shekhawat, A.C. Baranauskas, F. Mark, J.P. Dailey, D. Bardenstein, *Molecular pharmaceutics*, 6, (2009) 1417-1428.
- [111] S. Arooj, S. Nazir, A. Nadhman, N. Ahmad, B. Muhammad, I. Ahmad, K. Mazhar, R. Abbasi, *Beilstein J. Nanotechnol.*, 6, (2015)570-582.
- [112] M.S. Wason, J. Zhao, *Am. J. Transl. Res.* 5, (2013) 126-131.
- [113] M. Pesic, A. Podolski-Renic, S. Stojkovic, B. Matovic, D. Zmejkoski, V. Kojic, G. Bogdanovic, A. Pavicevic, M. Mojovic, A. Savic, I. Milenkovic, A. Kalauzi, K. Radotic, *Chem. Biol. Interact.*, 232, (2015) 85-93.
- [114] M.Y. Ge, H. Wang, E.Z. Liu, J.F. Liu, J.Z. Jiang, Y.K. Li, Z.A. Xu, H.Y. Li, *Appl. Phys. Lett.*, 93, (2008) 062505.
- [115] K.S. Ranjith, P. Saravanan, S.H. Chen, C.L. Dong, C.L. Chen, S.Y. Chen, K. Asokan, R. Thangavelu, R. Kumar, *J. Phys. Chem. C*, 118, (2014) 27039-27047.
- [116] M. Kumari, S.P. Singh, S. Chinde, M.F. Rahman, M. Mahboob, P. Grover, *International Journal of Toxicology*, (2014) 1091581814522305.
- [117] C.M. Bergamini, S. Gambetti, A. Dondi, C. Cervellati, *Curr Pharm Des.*, 10, (2004) 1611-26.

- [118] X.H. Fang, R. Yu, B.Q. Li, P. Somasundaran, K. Chandran, *J. Colloid Interface Sci.*, 348, (2010) 329–334.
- [119] A. Asati, S. Sentra, C. Kaittanis, J.M. PerezACS Nano, 4, (2010) 5321–5331.
- [120] S. Mittal, A.K. Pandey, *Biomed. Res. Int.*, 2014, (2014) 891934.
- [121] T. Jan, J. Iqbal, Q. Mansoor, M. Ismail, S.H. Naqvi, A. Gul, S.F.H. Naqvi, F. Abbas, *J. Phys. D: Appl. Phys.*, 47, (2014) 355301.
- [122] E. Malka, I. Perelshtein, A. Lipovsky, Y. Shalom, L. Naparstek, N. Perkas, T. Patick, R. Lubart, Y. Nitzan, E. Banin, A. Gedanken, *Small*, 23, (2013) 4069-76.
- [123] A. Nel, T. Xia, L. Madler, N. Li, *Science*, 311, (2006) 622-627.
- [124] C. Nutzenadel, A. Zuttell, D. Chartouni, G. Schmid, L. Schlapbach, *J. Eur. Phys. D*, 8, (2000) 245-250.
- [125] G.C. Bond, C. Louis, D.T. Thompson, *Catalysis by Gold*, Imperial College Press, London, 2006.
- [126] G. Gao, *Nanostructures and nanomaterials: Synthesis, properties and applications*, Imperial College Press, (2004).
- [127] Q. Wang, J.M. Perez, T.J. Webster, *International Journal of Nanomedicine*, 8, (2013) 3395-99.
- [128] F. Zhou, X. Ni, Y. Zhang, H. Zheng, *Journal of Colloid and Interface Science*, 307, (2007)135-138.
- [129] D. Zhang, X. Ni, H. Zheng, X. Zhang, J. Song, *Solid State Science*, 8, (2006) 1290-1293.
- [130] B. Xu, Q. Zhang, S. Yuan, M. Zhang, T. Ohno, *Chemical Engineering Journal*, 260, (2015) 126-132.
- [131] A.G. Khairnar, Y.S. Mhaisagar, A.M. Mahajan, *J. Nano- Electron. Phys.*, 5, (2013) 03002-5.

- [132] M. Farahmandjou, M. Zarinkamar, *Journal of Ultrafine Grained and Nanostructured Materials*, 48, (2015) 5-10.
- [133] E. Kumar , P. Selvarajan, D. Muthura, *Materials Research*, 16, (2013) 269-276
- [134] S. Phokha, S. Pinitsoontorn, P. Chirawatkul, Y. Pooarporn, S. Maensiri, *Nanoscale Res. Lett.*, 7, (2012) 425-37.
- [135] K.L. Chopra, S.R. Das, *Thin film solar cells*, Plenum press, N Y, (1983).
- [136] G.N. Eby, *Principles of Environmental Geochemistry*. Brooks/Cole-Thomson Learning, (2004) 212-214.
- [137] R.E. Ferrell, G.G. Paulson, *An Ortec Workshop, Energy Dispersive Analysis of X-ray Spectra Generated in the SEM*, Braniff Place, New Orleans, Louisiana,1973.
- [138] J.R. Ferraro, K. Nakamoto, C.W. Brown, *Book Introductory Raman Spectroscopy*, Amsterdam, The Netherland, 2003.
- [139] A. Bund A. Ispas, *Journal of Electroanalytical Chemistry*, 575, (2005) 221-228.
- [140] N.K. Park, J.D. Lee, T.J. Lee, S.O. Ryu, C.H. Chang, *Fuel*, 84, (2005) 2165-2171.
- [141] J. Kaspar, P. Fornasiero, M. Graziani, *Catal. Today*, 50, (1999) 285-298.
- [142] P. Jasinski, T. Suzuki, H.U. Anderson, *Sensors Actuat., B*, 95, (2003) 73-77.
- [143] S. Park, J.M. Vohs, R.J. Gorte, *Nature* 404, (2000) 265-267.
- [144] I. Porqueras, C. Person, C. Corbella, M. Vives, A. Pinyol, E. Bertan, *J. Solid State Ionics*, 165, (2003) 131-137.
- [145] V.D. Kosynkin, A.A. Arzgatkina, E.N. Ivanov, M.G. Chtoutsu, *J. Alloys Compd.*, 303, (2000) 421-425.
- [146] A. Bouaine, R.J. Green, S. Colis, P. Bazylewski, G.S. Chang, A. Moewes, E.Z. Kurmaev, A. Dinia, *J. Phys. Chem. C*, 115, (2011) 1556-1560.
- [147] A. Thurber, K.M. Reddy, V. Shutthanandan, M.H. Engelhard, C. Wang, J. Hays, A. Punnoose, *Phys. Rev. B*, 76, (2007) 165206-165211.

- [148] B. Ali, L.R. Shah, J.Q. Xiao, S.I. Shah, *J. Phys. Condens. Matter.*, 21, (2009) 456005-456011.
- [149] Q.Y. Wen, H.W. Zhang, Y.Q. Song, Q.H. Yang, H. Zhuand, J.Q. Xiao, *J. Phys. Condens. Matter.*, 19, (2007) 246205-246213.
- [150] Y. Liu, Z. Lockman, A. Aziz, J. MacManus-Driscoll, *J. Phys. Condens. Matter.*, 20, (2008) 165201-165205.
- [151] F. Vidal, Y. Zheng, J. Milano, D. Demaille, P. Schio, E. Fonda, B. Vodungbo, *Appl. Phys. Lett.*, 95, (2009) 152510-152516.
- [152] S. Colis, A. Bouaine, R. Moubah, G. Schmerber, C. Ulhaq-Bouillet, A. Dinia, L. Daheron, J. Petersen, C. Becker, *J. Appl. Phys.*, 108, (2010) 053910-053915.
- [153] V. Fernandes, J.J. Klein, N. Mattoso, D.H. Mosca, E. Silveira, E. Ribeiro, W.H. Schreiner, J. Varalda, A. de Oliveira, *Phys. Rev. B*, 75, (2007) 121304-121309.
- [154] Y.Q. Song, H.W. Zhang, Q.Y. Wen, L. Peng, J.Q. Xiao, *J. Phys. Condens. Matter.*, 20, (2008) 255210-255214.
- [155] Y.Q. Song, H.W. Zhang, Q.Y. Wen, H. Zhu, J.Q. Xiao, *J. Appl. Phys.*, 102, (2007) 043912-043915.
- [156] M. Kumari, S.I. Kumari, S.S.K. Kamal, P. Grovera, *Mutat. Res.*, 775, (2014) 7-19.
- [157] M.I.B. Bernardi, A. Mesquita, F. Beron, K.R. Pirota, A.O. de Zevallos, A.C. Doriguettod, H.B. de Carvalho, *Phys. Chem. Chem. Phys.*, 17, (2015) 3072-3080.
- [158] A.D. Liyanage, D.P. Sanjaya, K. Tan, Y. Chabal, J.B. Kenneth, *ACS Catal.*, 4, (2014) 577-584.
- [159] N.S. Arul, D. Mangalaraj, P.C. Chen, N. Ponpandian, P. Meena, Y. Masud, *J. Sol- Gel Sci. Technol.*, 64, (2012) 515-523.
- [160] L. Yan, X. Xing, R. Yu, L. Qiao, J. Chen, J. Deng, G. Liu, *Scr. Mater.*, 56, (2007) 301-304.

- [161] Y. Song, J. Wei, Y. Yang, Z. Yang, H. Yang, *J. Mater. Sci.*, 4, (2010) 4158-4162.
- [162] S.B. Khan, M. Faisal, M.M. Rahman, A. Jamal, *Sci. Total Environ.*, 409, (2011) 2987-2992.
- [163] E. Ziegler, A. Heinrich, H. Oppermann, G. Stover, *J. Phys. Status Solidi A*, 66, (1981) 635-648.
- [164] D. Barreca, G. Bruno, A. Gasparotto, M. Losurdo, E. Tondello, *J. Mater. Sci. Eng. C*, 23, (2003) 1013-1016.
- [165] J. Robertson, K. Xiong, S.J. Clark, *Thin Solid Films*, 496, (2006) 1-7.
- [166] K.W. Wagner, *Am. J. Phys.*, 40, (1973) 317-326.
- [167] J. Kuar, V. Gupta, R.K. Kotnala, K.C. Verma, *Indian J. Pure Appl. Phys.*, 50, (2012) 57-63.
- [168] C.G. Koops, *J. Phys. Rev.*, 83, (1951) 121-125.
- [169] J.M.D. Coey, A.P. Douvalis, C.B. Fitzgerald, M. Venkatesan, *Appl. Phys. Lett.*, 84, (2004) 1332-1334.
- [170] A. Sundaresan, R. Bhargavi, N. Rangarajan, U. Siddesh, C.N.R. Rao, *Phys. Rev. B*, 74, (2006) 161306-161311.
- [171] S. Atiq, S.A. Siddiqi, F. Abbas, M. Saleem, S.M. Ramay, *Chin. J. Chem. Phys.*, 26, (2013) 457-461.
- [172] S. Kumar, Y.J. Kim, B.H. Koo, H. Choi, C.G. Lee, *IEEE Transac. Magn.*, 45, (2009) 2439-2441.
- [173] J. Neamtu, M. Volmer, *J. Sci. World*, 2014, (2014) 7.
- [174] J. Yu, C. Yang, J. Li, Y. Ding, L. Zhang, M.Z. Yousaf, J. Lin, R. Pang, L. Wei, L. Xu, F. Sheng, C. Li, G. Li, L. Zhao, Y. Hou, *Adv. Mater.*, 26, (2014) 4114-4120.
- [175] W. Tang, Z. Zhen, C. Yang, L. Wang, T. Cowger, H. Chen, T. Todd, K. Hekmatyar, Q. Zhao, Y. Hou, J. Xie, *Small*, 10, (2014) 1245-1249.

- [176] R. Hergt, S. Dutz, R. Muller, M. Zeisberger, *Journal of Physics: Condensed Matter.*, 18, (2006) S2919.
- [177] Q.A. Pankhurst, J. Connolly, S.K Jones, J.J, Dobson, *Journal of physics D: Applied physics*, 36, (2003) R167.
- [178] E.J. Park, J. Choi, Y.K. Park, K. Park, *Toxicology*, 245, (2008) 90-100.
- [179] Y. Gao, K. Chen, J.L. Ma, F. Gao, *Onco Targets Ther.*, 7, (2014) 835-840.
- [180] D. Channei, B. Inceesungvorn, N. Wetchakun, S. Ukritnukun, A. Nattestad, J. Chen, S. Phanichphant, *Sci. Rep.*, 4, (2014) 5757-5763.
- [181] A. Tiwari, V.M. Bhosle, S. Ramachandran, N. Sudhakar, J. Narayan, S. Budak, A. Gupta, *Appl. Phys. Lett.*, 88, (2006) 142511-142513.
- [182] D. Channei, B. Inceesungvorn, N. Wetchakun, S. Ukritnukun, A. Nattestad, J.Chen, S. Phanichphant, *Ceram. Int.*, 39, (2013) 3129-3134.
- [183] H. An, J. Li, J. Zhou, K. Li, B. Zhu, W. Huang, *J. Mater. Chem.*, 20, (2010) 603-610.
- [184] R.D. Shannon, *Acta. Cryst. Sect. A*, 32, (1976) 7512767.
- [185] G.R. Li, D.L. Qu, L. Arurault, Y.X. Tong, *J. Phys. Chem. C*, 113, (2009) 1235-1241.
- [186] S. Tsunekawa, J.T. Wang, Y. Kawazoe, A. Kasuya, *J. Appl. Phys.*, 94, (2003) 5.
- [187] Y.S. Yu, G.Y. Kim, B.H. Min, S.C. Kim, *J. Eur. Ceram. Soc.*, 24, (2004) 1865-1868.
- [188] Q.Y. Wen, H.W. Zhang, Q.H. Yang, Y.Q. Song, J.Q. Xiao, *J. Appl. Phys.*, 107, (2010) 09C307.
- [189] W.C. Wang, S.Y. Chen, P.A. Glans, J. Guo, R.J. Chen, K.W. Fong, C.L. Chen, A. Gloter, C.L. Chang, T.S. Chan, J.M. Chen, J.F. Lee, C.L. Dong, *Phys. Chem. Chem. Phys.*, 15, (2013) 14701-14707.
- [190] I.S. Kim, M. Baek, S.J. Choi, *J. Nanosci. Nanotechnol.*, 10, (2010) 3453-3458.
- [191] Y.S. Kuang, X. He, Z.Y. Zhang, Y.Y. Li, H.F. Zhang, Y.H. Ma, Z.Q. Wu, Z.F. Chai, *J. Nanosci. Nanotechnol.*, 11, (2011) 4103-4108.

- [192] S.W. Bennett, A.A. Keller, *Appl. Catal. B*, 102, (2011) 600-607.
- [193] X. Cunni, W. Shaofei, S. Chunwen, L. Hong, C. Suiwai, C. Liquan, *Chin. J.Catal.*, 34, (2013) 305–312.
- [194] I.A. Rahman, P. Vejayakumaran, C.S. Sipaut, J. Ismail, C.K. Chee, *Materials Chemistry and Physics*, 114, (2009) 328-332.
- [195] J.C. Maxwell, *Electricity and Magnetism*, New York: Oxford university press, 2, (1973) 828.
- [196] C. Xia, C. Hu, P. Chen, B. Wan, X. He, Y. Tian, *Res. Bull.*, 45, (2010) 794-798.
- [197] S. Alarifi, D. Ali, S. Alkahtani, M.S. Alhader, *Biol. Trace Elem. Res.*, 159, (2014) 416-424.
- [198] S. Nie, Y. Xing, G.J. Kim, J.W. Simons, *Nanotechnology applications in cancer*, *Annu. Rev. Biomed. Eng.*, 9, (2007) 257-288.
- [199] S. Hellman, *Cancer Res.*, 40, (1980) 4335-4342.
- [200] T. Jan, J. Iqbal, M. Ismail, Q. Mansoor, A. Mahmood, A. Ahmad, *Appl. Surf. Sci.*, 308, (2014) 75-81.
- [201] S. Patil, S. Seal, Y. Guo, A. Schulte, J. Norwood, *Applied Physics Letters*, 88, (2006) 243110-243110.
- [202] X. Zhang, J. Wei, H. Yang, X. Liu, W. Liu, C. Zhang, Y. Yang, *Eur. J. Inorg. Chem.*, 25, (2013) 4443-4449.
- [203] F. Arena, G. Trunfio, J. Negro, B. Fazio, L. Spadaro, *Chemistry of materials*, 19, (2007) 2269-2276.
- [204] V. Shapovalov, H. Metiu, *Journal of Catalysis*, 245, (2007) 205-214.
- [205] L.W. Jia, M.Q. Shen, J.J. Hao, T. Rao, J. Wang, *Journal of Alloys and Compounds*, 454, (2008) 321-326.

- [206] S. Babu, R. Thanneeru, T. Inerbaev, R. Day, A.E. Masunov, A. Schulte, S. Seal, *Nanotechnology*, 20, (2009) 085713.
- [207] J. Tan, W. Zhang, Y.H. Lv, A.L. Xia, *Materials Research*, 16, (2013) 689-694.
- [208] K.S. rinivas, M. Vithal, B. Sreedhar, M.M. Raja, P.V. Reddy, *J. Phys. Chem. C*, 113, (2009) 3543–3552.